Roma Tre

CORSO DI DOTTORATO DI RICERCA IN

Scienze della materia e dei nanomateriali

XXXVIII ciclo

Gold nanorods: synthesis, characterization, functionalization with radiopharmaceutical and *in vitro* testing for application in nuclear medicine

---

Ludovica Binelli

_____

Iole Venditti

_____

Docente Guida/Tutor: Prof

Valentina Dini

_____

Docente Guida/Tutor: Prof

Marco Barbieri

_____

Coordinatore: Prof.

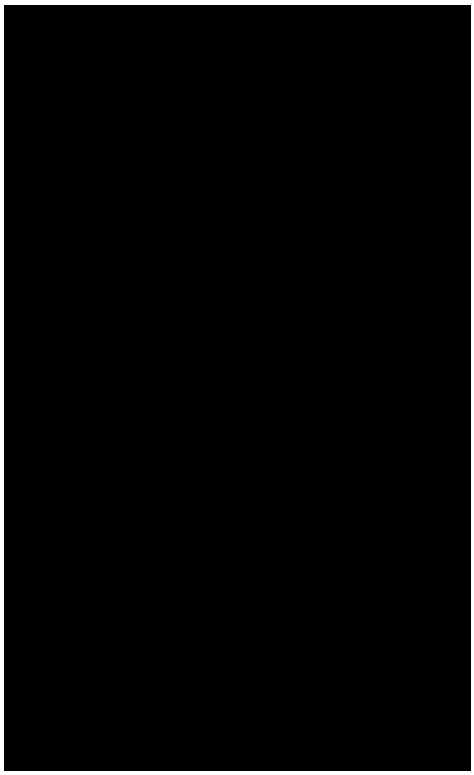

INDEX

ABSTRACT **4**

1. INTRODUCTION **5**

1.1. CHARACTERISTICS AND PROPERTIES OF NANOPARTICLES ***5***

1.1.1 FUNCTIONALIZATION OF GOLD NANOPARTICLES FOR CANCER THERAPY *11*

1.2. GOLD NANORODS (AUNRS) ***14***

1.3. FUNDAMENTALS OF IONIZING RADIATION ***17***

1.3.1 TYPES OF IONIZING RADIATION *18*

1.3.2 LINEAR ENERGY TRANSFER (LET) *22*

1.3.3 TRACK STRUCTURE *24*

1.3.4 INTERACTION BETWEEN GOLD AND RADIATION *25*

1.3.5 EFFECTS OF IONIZING RADIATION ON BIOLOGICAL SYSTEMS *26*

1.3.5.1. DNA DAMAGE 29

1.4. SYNCHROTRON CHARACTERIZATION ***32***

1.5. SEGNAR PROJECT ***33***

2. EXPERIMENTAL DESIGN AND SET UP **35**

2.1. MATERIAL AND METHODS ***35***

2.1.1. INSTRUMENTATION *35*

2.1.2. AUNRS SYNTHESIS AND PURIFICATION *38*

2.1.3. CONJUGATION WITH ^{99M}TC *39*

2.1.4. CONJUGATION WITH TAT PEPTIDE *40*

2.1.5. DLS MEASUREMENT *42*

2.1.6. STRUCTURAL CHARACTERIZATION *42*

2.1.6.1 SYNCHROTRON RADIATION INDUCED X-RAY PHOTOELECTRON SPECTROSCOPY (SR-XPS) 42

2.1.6.2 NEAR EDGE X-RAY ABSORPTION FINE STRUCTURE (NEXAFS) 43

2.1.6.3 REFLECTION-ABSORPTION INFRARED SPECTROSCOPY (RAIRS) 43

2.1.7. BIOLOGICAL CHARACTERIZATION *44*

2.1.7.1 COLONY-FORMING ASSAY 44

2.1.7.2 REALTIME-GLO ™ MT CELL VIABILITY ASSAY VALIDATION PROTOCOL 45

2.1.7.3 γ-H2AX ASSAY VALIDATION PROTOCOL 46

3. RESULTS AND DISCUSSION **47**

3.1. SYNTHESIS AND CONJUGATION OF AUNRS ***47***

3.1.1 DLS CHARACTERIZATION *50*

3.2. SYNCHROTRON RADIATION-INDUCED SPECTROSCOPIC ANALYSIS ***51***

3.2.1. SYNCHROTRON RADIATION INDUCED X-RAY PHOTOELECTRON SPECTROSCOPY (SR-XPS) *51*

3.2.1.1. ^{99}TC-SESTAMIBI AND AUNRS CONJUGATION 52

3.2.1.2. TAT PEPTIDE AND AUNRS CONJUGATION 53

3.2.2. NEAR EDGE X-RAY ABSORPTION FINE STRUCTURE (NEXAFS) *55*

3.2.2.1. TAT PEPTIDE AND AUNRS CONJUGATION 55

3.2.3. REFLECTION-ABSORPTION INFRARED SPECTROSCOPY (RAIRS) *57*

3.2.3.1. ^{99}TC-SESTAMIBI AND AUNRS CONJUGATION 57

3.2.3.2. TAT PEPTIDE AND AUNRS CONJUGATION 58

3.3. BIOLOGICAL RESULTS ***60***

3.3.1. COLONY-FORMING ASSAY *60*

3.2.1. RealTime-Glo ™ MT cell viability Assay validation protocol *62*
3.2.2. γ-H2AX assay validation protocol..... *64*
5. CONCLUSION..... **72**
6. APPENDIX A:..... **74**
7. BIBLIOGRAPHY..... **75**

ABSTRACT

This research focuses on the development and validation of a nano-radiosensitization strategy using gold nanorods functionalized with the TAT peptide (AuNR-TAT) to enhance the efficacy of radiotherapy. The core objective was to exploit the high atomic number of gold to increase radiation absorption and induce localized biological damage through the emission of Auger electrons.

The study successfully demonstrated that the AuNR-TAT system possesses high colloidal stability and low intrinsic toxicity, making it a safe candidate for clinical applications. A central part of the investigation involved the use of physical-chemical characterization to optimize the conjugated system and Transmission Electron Microscopy (TEM) to track the intracellular fate of the nanoconstructs. The analysis revealed that while the TAT peptide facilitates high cellular uptake, the nanorods are predominantly sequestered within endolysosomal vesicles in the perinuclear region rather than translocating into the nucleus. Radiobiological assays showed a significant increase in γ-H2AX foci following irradiation, indicating enhanced DNA damage. This finding suggests that the radiosensitization is mediated by an indirect mechanism: Auger electrons generated by irradiation of AuNRs in the cytoplasm produce reactive species that migrate into the nucleus to induce complex, clustered DNA breaks. In conclusion, this work indicates that nuclear proximity could be sufficient to promote radiobiological enhancement; however, these findings should be considered as preliminary and may represent a possible proof of concept for future targeted nano-radiotherapies.

1. INTRODUCTION

1.1. CHARACTERISTICS AND PROPERTIES OF NANOPARTICLES

The term "nanometre" was first used in 1914 by Richard Adolf Zsigmondy who was the first to measure particles with a dimension between 1 and 10^{-6} meters. With this measurement he developed a system of classification based on in particle size in the nanometre range. In 1959 the Nobel Prize Richard P. Feynman introduced the concept of nanotechnology during his seminary "There's plenty room at the bottom" at the American Physical Society's annual meeting. Dr. Feynman suggested that in the end it would be possible to manipulate the atoms and molecules to create nanoscale machines that will be able to create tinier "factories" with smaller and smaller dimensions, to the point where the gravity will be negligible and the Van Der Waals attraction and surface tension will become more significant [1, 2]. Starting from this concept studies with the main idea of developing systems in the nanoscale, 10^{-7}-10^{-9} m, began to take place (Fig. 1).

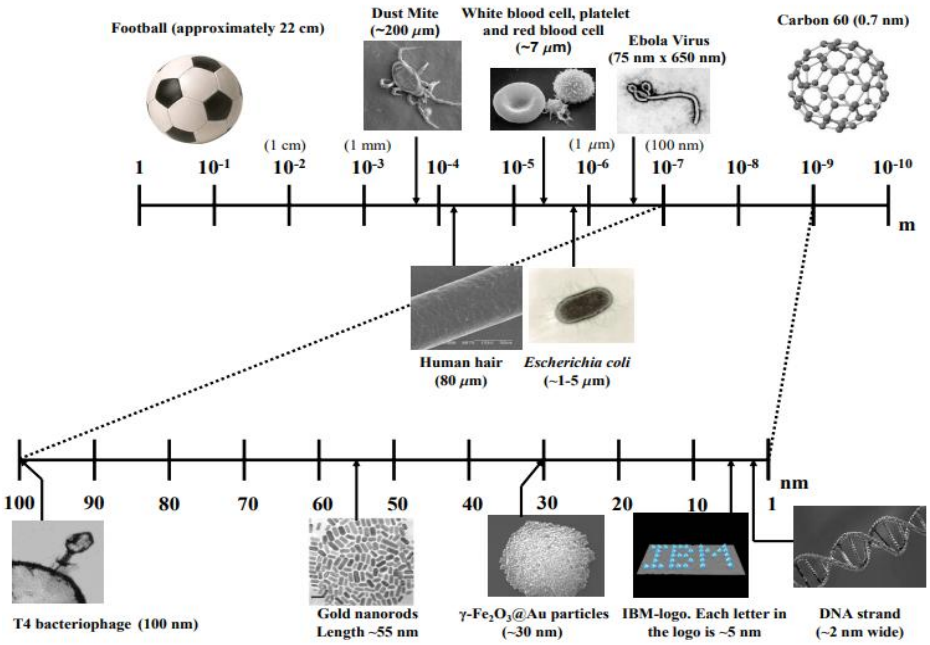

Figure 1. Picture showing the nanoscale in context. The length scale at the top ranges from 1 m to 10^{-10} m. The section from 10^{-7} m (100 nm) to 10^{-9} m (1 nm) is expanded on the length scale beneath. The typical length scale of interest for nanoscience is from 100 nm down to the atomic scale [3].

As for nanomaterial are understood those materials in which at least one dimension is less than 100 nm. This can be translated into a very small size (1-100 nm) in which the material acquires new physical, chemical, electrical and magnetic properties that differ from the bulk material [2]. Since the volume becomes smaller, the ratio between volume and surface increases and the percentage of atoms on the nanomaterial surface becomes more significant. This phenomenon is responsible for some physical and optical properties such as the Surface Plasmon Resonance (SPR). These materials have a wide range of possibilities for use as for example in drug delivery since they can be engineered with drugs, proteins, siRNA[1], enzymes and biomolecules [4].

Nanomaterials can be classified by both their shape and their dimensionality. While their shape defines their geometry such as spheres, stars, rods, cubes, or wires, their dimensionality is determined by the number of dimensions outside the nanoscale. Specifically, they are categorized as zero-dimensional (0D), one-dimensional (1D), two-dimensional (2D), or three-dimensional (3D).

The 0D materials are those in which all the three dimensions (x, y, z) fall within the nanometric scale. Spherical nanoparticles, nanocubes and some polygonal shapes are part of this group (Figure 2 a-c). The 1D (Figure 2 d-i) are represented by nanotubes, nanorods and nanowires. In this case two of the three dimensions are in the nanoscale and they present unique advantages due to their high aspect ratio (A.R.) combined with superior mechanical, electrical and optical properties. Regarding the 2D nanomaterials only the x dimension is in the nanoscale (Figure 2 j-l) and includes nanofilms and nanolayers. The 3D has no dimension in the nanoscale, but they have a nanocrystal structure or involve the presence of features at the nanoscale, for this reason they are still considered nanomaterials (Figure 2 m-o) [5].

[1] siRNA (small interfering RNA): Short double-stranded RNA molecules (approximately 20-25 nucleotides) that regulate gene expression through the RNA interference (RNAi) mechanism, inducing the degradation of specific complementary mRNA strands and thereby preventing the synthesis of the target protein.

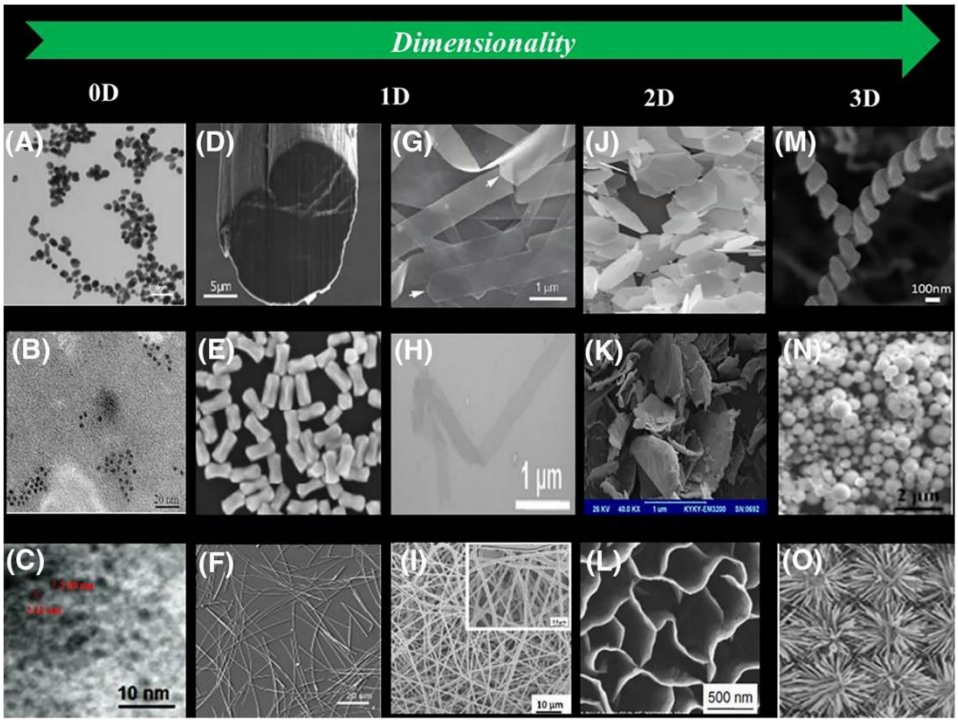

Figure 2. SEM and TEM images of different types of nanostructure: a) Au nanoparticles, b) CdTe quantum dots, c) Au nanocluster, d) carbon nanotubes, e) Au nanorods, f) Ag nanowires, g) MnO_2 nanoribbons, h) graphene oxide nanoribbons, i) boron nitride and gelatine nanofibers, j) Au nanodisks, k) graphene oxide nanolayers, l) carbon nanowall, m) carbon nanocoils, n) graphene nanospheres with copper cores, o) Pd nanoflowers [6].

Nanosphere are synthetized starting from polymeric materials, inorganic material or a combination of both. They are widely used for drug delivery due to their exceedingly small size they can release pharmaceutical (drugs) in the right spot. Nanostars, on the other hand, have sharp corners that allow an increase of the electromagnetic field around of the particles. The nanorods have a cylindrical shape with two sides of different dimension, both in nanometric scale, which have between them a length-to-thickness ratio (aspect ratio) in the range of 2 to 5. These types of particles are very useful for drug delivery because the possess two sides that can be functionalized with different macromolecule simultaneously and for the same reason their optical properties are very peculiar [6].

In general, metallic nanoparticles have received much popularity in the last years. This kind of material can be functionalized with a multitude of different biological molecules, but they can also be widely used in the catalysis, magnetic and mechanical fields. Their discover is to dates back in ancient times, back to the 4th century A.D. where ancient Romans would use colloidal

solution of gold as decoration like in the Lycurgus cup (Fig. 3) in which we can observe a reflected green colour that changes in red when the light is transmitted to the glass of the cup [7].

Figure 3. The Lycurgus Cup that contains gold nanoparticles that change colour depending on the light position [7].

Noble metal nanoparticles were widely used in the past for example in 1727 John Herman Schulze observed that silver salts turned black when exposed to light [8], 1890 Robert Koch discovered that $K[Au(CN)_2]$ potassium gold cyanide at low concentration has an antimicrobial activity against Tuberculosis bacillus [9]. Faraday conducted studies on the colouring effect of colloidal gold in solution and in glasses and was the first to suggest that the colour comes from extremely fine dispersed particles of gold [10, 11].

In the last years metal nanostructures have been the focus of different research fields, since they can be applied in different areas: surface plasmonic, surface-enhanced Raman scattering, chemical and biological sensing and photothermal therapy. Their properties depend on their size and shape [12]. For example, functionalized gold nanospheres can be used for drug delivery by loading L-Cysteine on their surface that allows the bond with the drug [13].

The principal characteristic of nanomaterials, specifically of noble metal nanomaterials, is an optical property called Localized Surfaced Plasmon Resonance (LSPR). This phenomenon

occurs when the nanomaterial interacts with an electromagnetic radiation with the appropriate wavelength causing a synchronised oscillation between radiation and the surface electrons. This generates a charge separation with free electron oscillation around positive holes. If the wavelength of the radiation matches the frequency of the electrons, in the conduction bands, then the oscillations become resonant, leading to a highly localized increase of the electromagnetic field in a confined area of several nanometres surrounding the particles. The LSPR possess a double origin: one is the absorption component, and the other is the scattering, but the absorption is dominant between the two. To analyse this phenomenon the UV-Visible or Infrared spectroscopy can be used because nanomaterials made of silver or gold produce the SPR in the near infrared or in the visible-ultraviolet range (Fig. 4) [14, 15, 16].

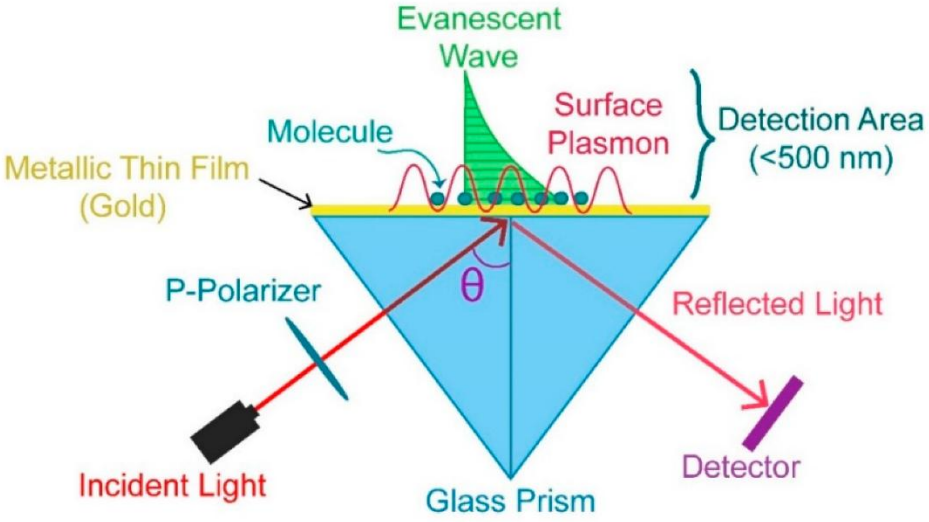

Figure 4. Schematic representation of the Surface Plasmon Resonance phenomenon [14].

Nanomaterials synthesis depends on the result that want to be obtained like dimension or shape but also on the biocompatibility that is required for that particular material. In general, there are two approaches: the top-down and the bottom-up (Fig. 5).

The top-down method employs physical principles to create nanostructures by breaking down bulk materials. The process begins with a large quantity of precursor—such as molten metal—which is then fragmented into nanoparticles using various techniques. Among these, laser ablation is one of the most prominent due to its high reproducibility and effectiveness in producing high-purity materials. In this process, a high-power laser beam is focused onto a solid target (the bulk material). The intense energy of the laser pulses causes the rapid evaporation and ionization of the target surface, creating a plasma plume. When this occurs in

a liquid medium, the plasma is quickly quenched, leading to the nucleation and growth of nanoparticles. A significant advantage of this technique is that it allows for the synthesis of ligand-free nanoparticles, which are inherently biocompatible and possess "clean" surfaces, ideal for subsequent functionalization without the interference of residual chemical precursors [17].

Conversely, the bottom-up approach starts from atomic, ionic, or molecular units that are assembled into nanometric structures through processes like chemical reduction or biosynthesis. This is the standard route for producing noble metal nanomaterials. In a typical chemical reduction, a metal precursor (generally in the form of a salt) is reduced by specific agents, such as sodium borohydride or ascorbic acid, and subsequently stabilized by capping agents to prevent aggregation [18, 19].

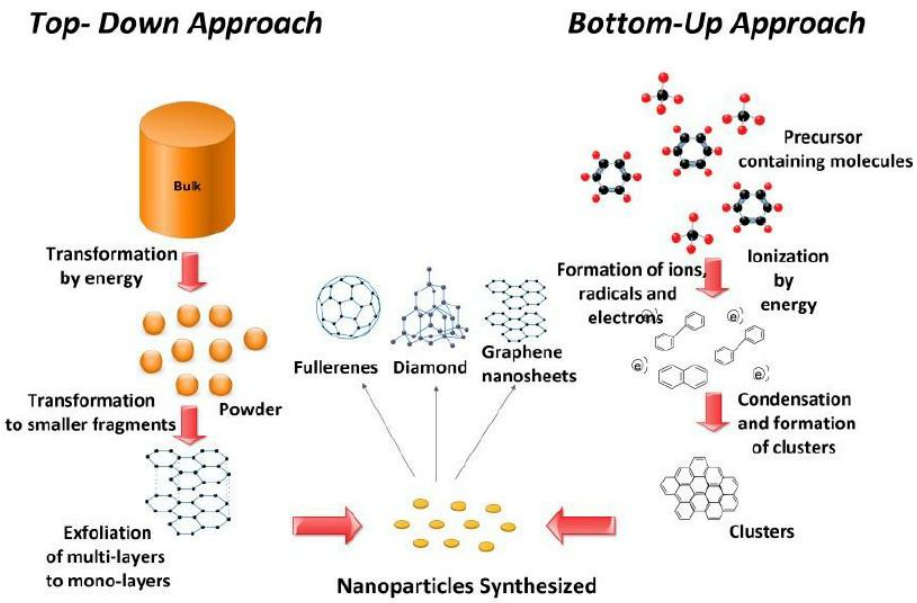

Figure 5. Representation of the two synthesis approaches to produce nanoparticles [20].

1.1.1 *FUNCTIONALIZATION OF GOLD NANOPARTICLES FOR CANCER THERAPY*

Nanotechnology is an interdisciplinary research field involving disciplines like chemistry, engineering, biology and medicine. This close collaboration between fields creates a great potential for early detection, accurate diagnosis and personalized treatment of cancer. The cancer treatment could be revolutionized due to the fact that the smaller size (nanometric scale) of the particles, that result one hundred times smaller than human cells, could permit the interaction with the cellular membrane or, in the best case, the particles can enter in the cells and interact with the various cytoplasmic organelles [21, 22]. Inside the broad world of nanoparticles, the gold nanoparticles (AuNPs) have received major attention due to their well-established biocompatibility, simple method of synthesis, and stability. Gold, as a material, possesses a high electron content and a low chemical reactivity and these properties make AuNPs suitable as imaging agents. Also, the optical properties that they present, such as strong scattering and absorbance in the visible-near-infrared (Vis-NIR) region can be used for cancer therapy [23, 24, 25]. The rod-shaped AuNRs present a typical cylindrical shape that allows a large attachment of material and confers plasmonic properties to the nanomaterial [26].

One of the most studied of AuNPs applications in cancer therapy is the photothermal therapy (PTT) that combines high biological selectivity with minimal surgical invasion. While traditional PTT relies primarily on organic photosensitizers activated by specific light wavelengths—often facing limitations in selectivity and stability—the integration of AuNPs optimizes the use of laser radiation by acting as extremely efficient and versatile photothermal agents. The AuNPs present a high superficial plasmonic resonance that consent the absorption of radiation in the near infrared (NIR) with the consequence of a high efficiency photothermal conversion. This characteristic leads to the possibility to modulate the optical response through the control of shape, dimension and superficial functionalization, allowing a localized enhancement of surface temperature that induces cell death in tumoral tissues [27,28]. Von Maltzan and colleagues [29] synthetized nanocarriers based on Pluronic F68 modified with chitosan in which AuNRs were loaded, with a NIR peak at 808 nm. The system was further functionalized with polyethylene glycol (PEG) to increase the circulation time. They demonstrate, *in vitro*, that after irradiation with a NIR laser the temperature reached around

50°C and the cell death was about 90% due to necrosis from protein denaturation and, *in vivo*, almost complete regression of the tumour was achieved in 5-7 days.

Gold nanoparticles can be largely functionalized: it means that on their surface can be attached molecules, like peptide or pharmaceuticals, making them useful for biomedical applications such as imaging, diagnostics, or drug delivery to perform therapy. Nanoparticles made of gold can be functionalized by different techniques: (I) the ligand exchange method; (II) the introduction of bifunctional thiols; (III) the use of many different capping agents throughout the synthesis mixture; (IV) post-synthesis reactions. Ligand exchange is an easy and inexpensive way to functionalize the gold surface, but it often leads to partial coverage that is short-lived (Fig. 6). The use of bifunctional thiols (HS--X), which have a free terminal group X, such as thiol, acid, or amine, allows the particles to interact with the external environment and perform post-synthesis modifications. It is also possible to introduce different capping agents simultaneously, in order to introduce different specific functions but with strict control of the synthetic parameters (pH, concentration, reducing agent, temperature) to ensure success. Post-synthesis functionalization allows modifications of the surface to introduce new characteristics, molecules or drugs. The modifications can be achieved through four main approaches: (I) covalent bonding; (II) electrostatic interaction; (III) direct reaction to thiol; and (IV) secondary interactions [13].

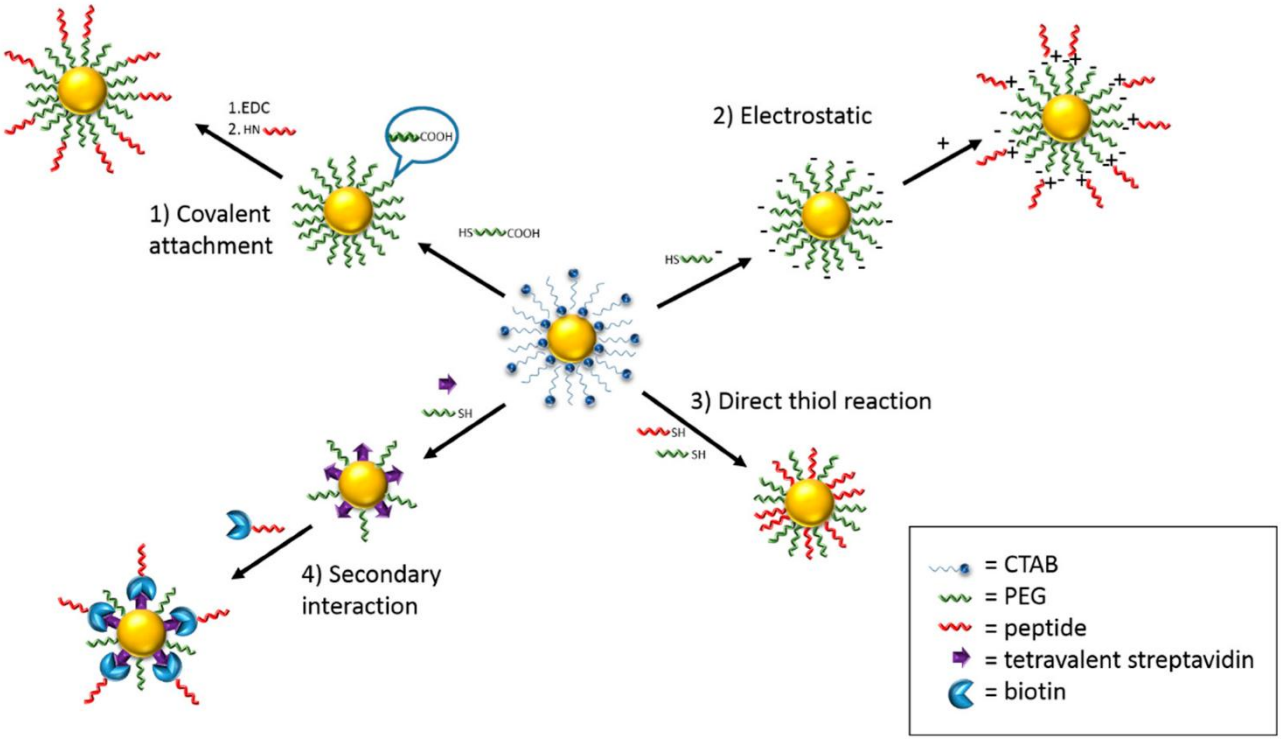

Figure 6. Four principal modification approaches for nanomaterial's surface functionalization using PEG and a peptide as examples of biomolecules [30].

Xie et al. [31], used AuNRs functionalized with PEG and a stable fluorescent molecule (NPAPF) to obtain a theranostic system named NPAPF-AuNRs@PEG. All the components have a specific role in the cancer treatment: AuNRs are needed for the PTT because they can increase the cell damage due to the radiotherapy in the radioresistant tumours; PEG increases the biocompatibility of AuNRs limiting their toxicity and increasing the circulation time and the fluorophore is useful to localize with precision the tumour and at the same time to monitoring in real time the response to the treatment. What they observed *in vitro* was that in cell lines like HeLa and SiHa the AuNPs system + radiation therapy had greater efficiency in increasing Reactive Oxygen Species (ROS), DNA damage and reducing cell migration. At the same time, *in vivo,* the system combined with NIR laser and radiotherapy resulted in an almost total elimination of tumour.

1.2. GOLD NANORODS (AUNRS)

AuNRs are classified as 1D materials, with a peculiar cylindrical shape that permit to increase the surface/volume ratio and the aspect ratio (Fig. 7), namely the ratio between the transverse side and the longitudinal side [32,33].

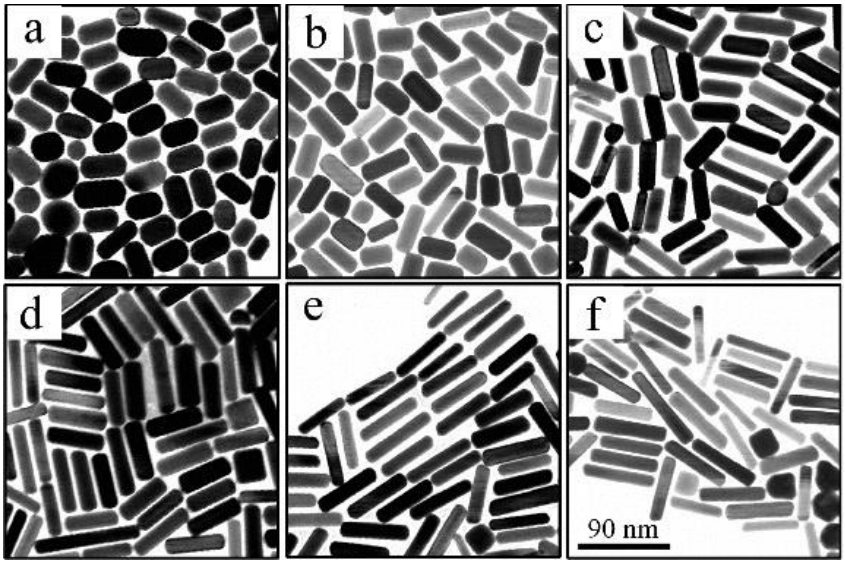

Figure 7. AuNRs with different aspect ratio due to the different concentration of silver nitrate ($AgNO_3$) [34].

The cylindrical shape of the AuNRs gives them a specific visualization of the LSPR's effect (Fig. 8). Due to the different dimensions of the two sides the UV-Vis-NIR spectra result in two plasmonic peak associated with the different oscillations that the electrons have in the transversal and longitudinal sides. The presence of these two peaks can be very useful for investigating the AuNRs surrounding and more specifically to understand if a ligand is present or not. It has in fact been discovered that the longitudinal plasmon is very sensitive to the surrounding environment. Pellas et al. studied how a silica coating, if it's too thick, interferes with the LSPR, whose sensitivity decreases in relation to the fact that the oscillations field are shielded by the layer [33, 35].

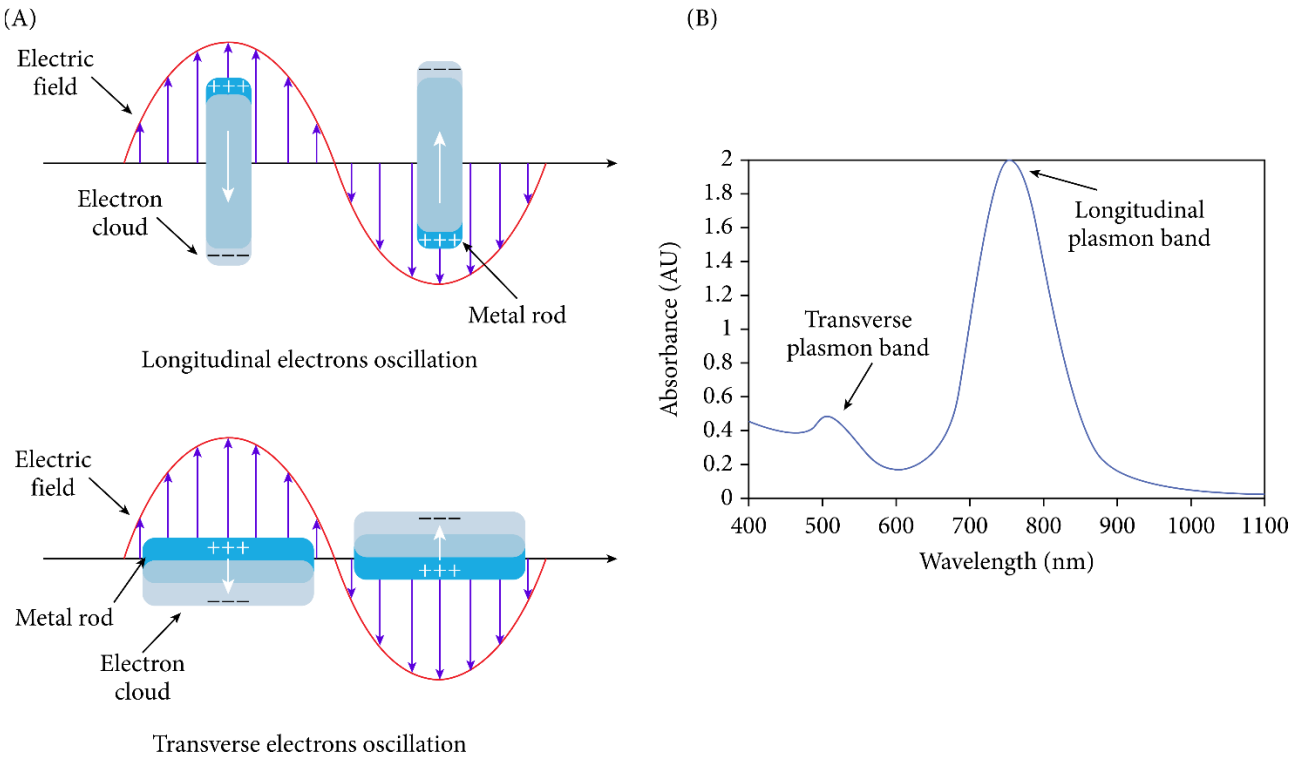

Figure 8. LSPR of AuNRs in which it is highlighting the presence of the two plasmon: the first one (transversal) it's around 500 nm, the second appears around 700 nm. Modified from Meng et al. [36].

The AuNRs can be prepared with a wide range of different techniques, but the most used is the wet method initially proposed by Murphy in 2001 [37] and revived and upgraded by Nikoobakht and El-Sayed in 2003 [38]. The seed mediated synthesis of AuNRs consist of two steps (Fig. 9). During the first, the so-called "seeds" are produced, which are very small nanoparticles, measuring between 2 and 4 nm, that serve as nucleation centres for the AuNRs growth. The seeds are made with tetra-chloroauric (III) acid ($HAuCl_4$), cetyltrimethylammonium bromide (CTAB, a surfactant agent) and a reducing agent that is sodium borohydride ($NaBH_4$). For the growth solution of AuNRs, the gold and surfactant remain the same, but the ascorbic acid (AA) is used as reducing agent to convert Au^{3+} to Au^{+1}. In addition, silver nitrate ($AgNO_3$) is introduced, as it promotes the anisotropic growth of AuNRs by selectively binding to specific gold facets inhibiting the growth along those directions [39, 40].

The CTAB, needed for the stabilization, forms a peculiar structure around gold ions, in both seed and growth solution, turning the solution form the light yellow of gold to a more dark-yellow/orange colour when the surfactant is added. The modulation of the experimental

parameters, like reagent concentration, pH and temperature, allows the control of dimensions and polydispersity of the solution [38].

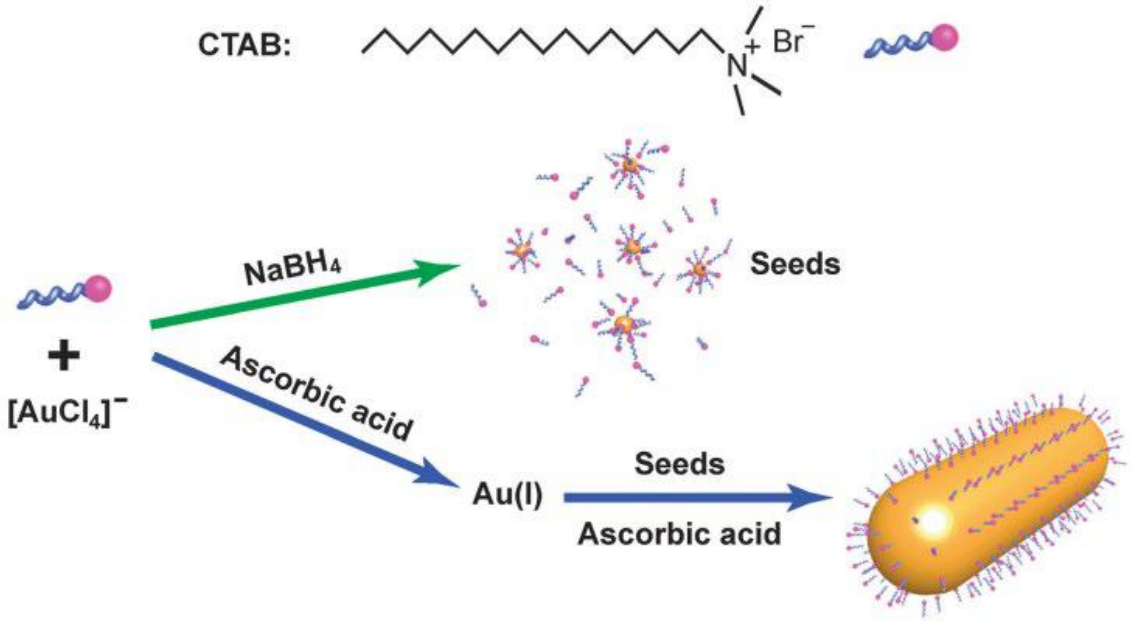

Figure 9. Schematic representation of seed-mediated synthesis of AuNRs [33].

1.3. *FUNDAMENTALS OF IONIZING RADIATION*

Radiation is a physical phenomenon involving the emission and propagation of energy through space, which can occur in the form of electromagnetic waves (photons) or particles (corpuscular). This energy propagates in a straight line and can transfer part of its energy to the matter with which it interacts (Fig. 10). Radiation can be mainly divided into two categories:

- Electromagnetic radiation: wave-like radiation that propagates through space at the speed of light. A unit of electromagnetic radiation (photon) is characterised by a magnetic field and an electric field whose vectors are perpendicular to each other and to the direction of wave propagation.
- Corpuscular radiation: radiation consisting of atomic or subatomic particles such as electrons, protons, neutrons, etc.

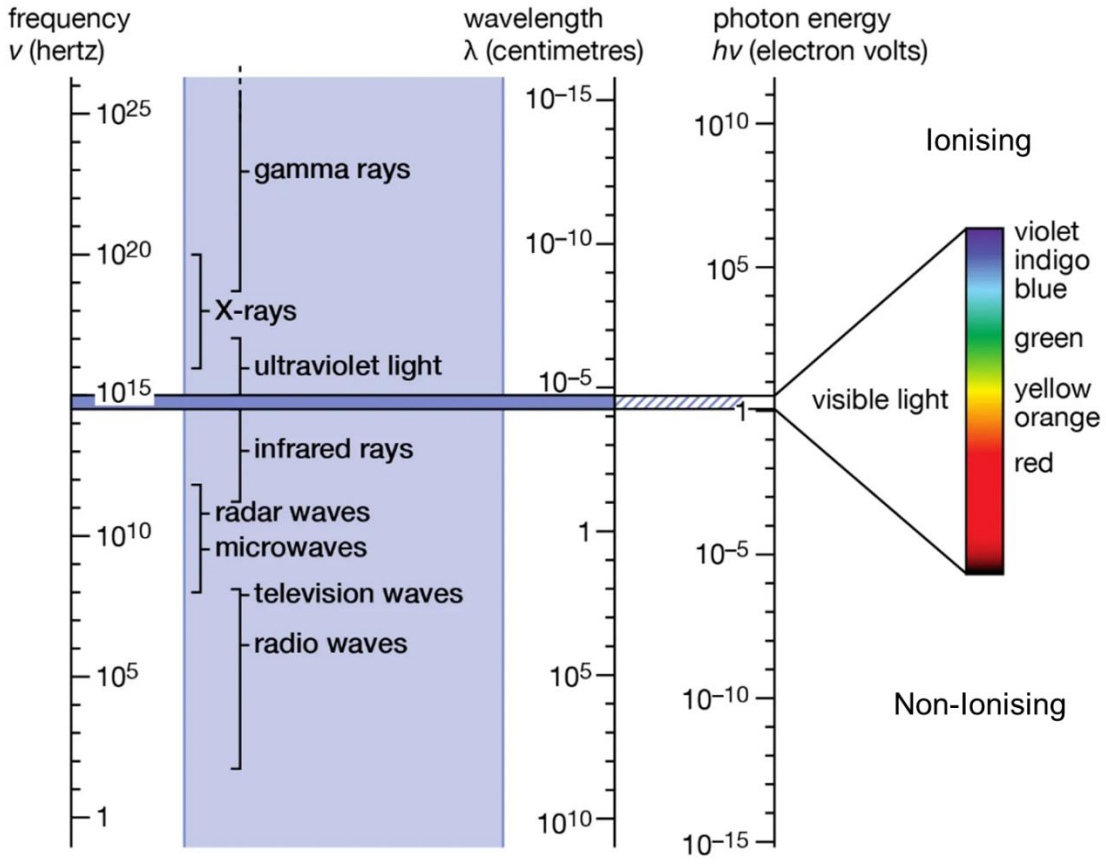

Figure 10. Electromagnetic spectrum. Modified from Shahi et al. [41].

1.3.1 TYPES OF IONIZING RADIATION

Ionizing radiation is defined as radiation possessing sufficient energy to produce both excitations and ionizations in the matter it traverses, through processes of energy deposition at the atomic and molecular levels [42, 43]. In the case of excitation, an electron within an atom or molecule absorbs part of the energy carried by the incident particle and is promoted from its ground state to a higher energy level. In this process, the energy transferred in a single interaction remains below the electron's binding energy and is therefore insufficient to detach the electron from the atom or molecule [44]. Ionization, on the other hand, occurs when the energy lost by the incident particle exceeds the electron's binding energy. The electron is consequently ejected from the atom or molecule, resulting in the formation of an ion pair-comprising a positively charged residual atom or molecule and a free, negatively charged electron. The surplus energy, corresponding to the difference between the transferred energy and the electron's binding energy, corresponds to the kinetic energy of the emitted electron [45]. In certain cases, the kinetic energy of this primary electron is sufficiently high to induce additional ionizations along its path, producing further electrons known as secondary electrons. These secondary processes play a crucial role in determining the spatial distribution of energy deposition, which underpins the physical, chemical, and ultimately biological effects of ionizing radiation [44, 46].

Ionizing radiation can be divided into charged and neutral [47, 48]. The charged radiation consists of subatomic particles, with positive or negative charge, that directly interact with the electrons of the atoms of matter they travers (direct ionization). Interactions can be Coulombic or strong interactions with nuclei of the atoms. Neutral radiation, instead, does not directly interact with the atoms of the matter trough which it passes. It transfers all or part of its energy to these atoms, generating secondary charged particles such as rebound protons or secondary electrons. The latter dissipate the energy acquired in the matter, generating ionisations and excitations (indirect ionization) [47, 48].

When photons interact with matter, three primary processes dominate depending on the photon energy and the atomic number (Z) of the material: pair production, Compton scattering and the photoelectric effect (Fig. 11).

Pair production (Fig. 11A) occurs when a high-energy photon (≥ 1.022 MeV) passes through the intense electromagnetic field of an atomic nucleus. The photon, under the influence of the nuclear Coulomb field, is annihilated, and its energy is converted into an electron (e^-) and a positron (e^+) pair. The presence of the nucleus is essential to conserve momentum. [47, 48].

At intermediate photon energy (100 keV-10 MeV), the Compton effect (Fig. 11B) becomes dominant. In this case, the photon transfers only part of its energy to an electron in one of the valence orbitals, which have very low binding energy, resulting in the expulsion of the electron. The probability of this effect is independent of the atomic number of the material. The photon, still possessing energy, continues its path, but in a different direction from that of incidence, and may still interact with other atoms in the material [47, 48].

At low photon energy (< 0.5 MeV), the photoelectric effect (Fig. 11C) prevails. The photon is completely absorbed by an atom transferring its energy to an inner-shell electron, which is ejected with a kinetic energy equal to the photon energy minus the electron's binding energy. The probability of this effect occurring is higher the greater the atomic number (Z^4-Z^5) of the medium through which it passes and the more closely the electron is bound to the atom. The atoms that undergo this process often result in the emission of X-ray or Auger electrons [47, 48].

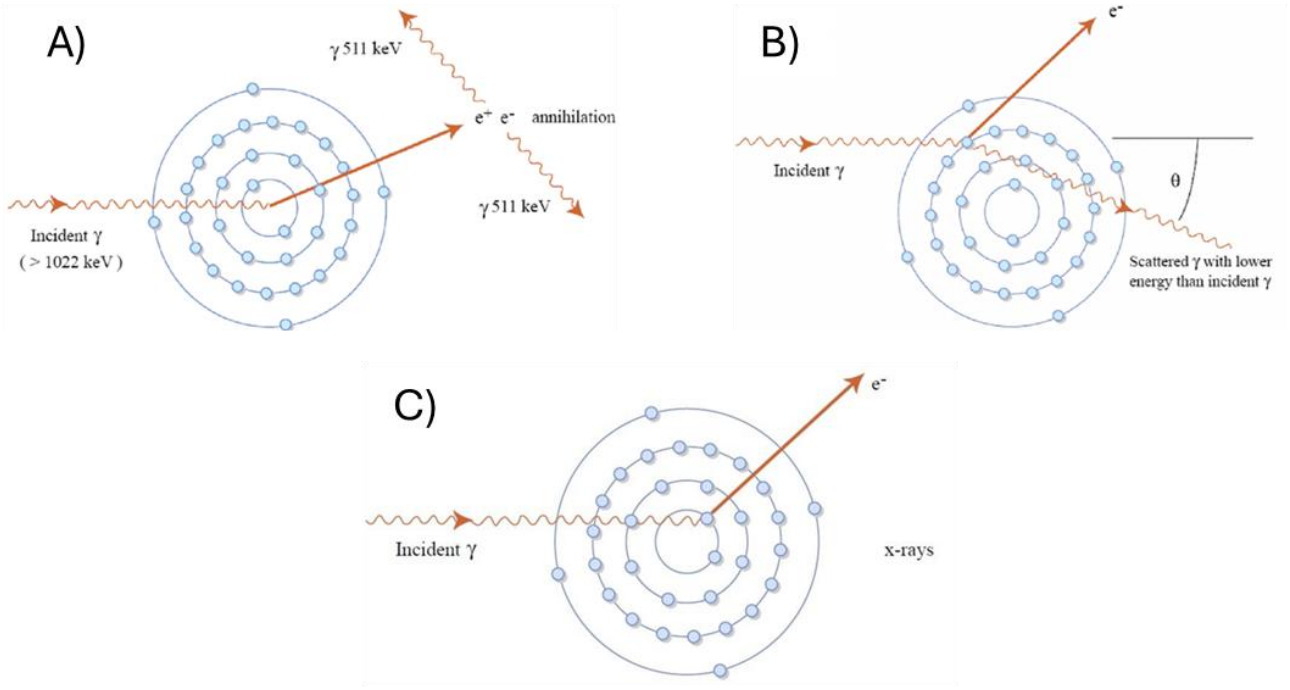

Figure 11. Representation of the three effects. A) pair production; B) Compton scattering; C) photoelectric effect [49].

The Auger electrons are low energy electrons, having kinetic energy typically in the range from 100 to 1000 eV, depending on the atomic number of the element and on the electronic shell involved in the transition. In addition, they can cover very short distance (i.e. short range from 10 to 100 nm) in which the energy deposition is very local, leading to highly localized ionization and potential biological damage at the cellular and subcellular level. In biological systems this means that an Auger cascade can deposit all its energy within a few nanometres, compared to the diameter of DNA (≈ 2 nm). As a result, Auger emitting radionuclides, such iodine-125 or indium-111, can produce highly localized ionizations and clustered DNA damage (Fig. 12), often lethal to cells when decay occurs near the nucleus [50]. For this reason, their use can be effective in the treatment of radioresistant tumours, such as glioblastoma multiform.
The Auger electron emission and its potential as therapeutic agent is a fundamental part of this thesis work.

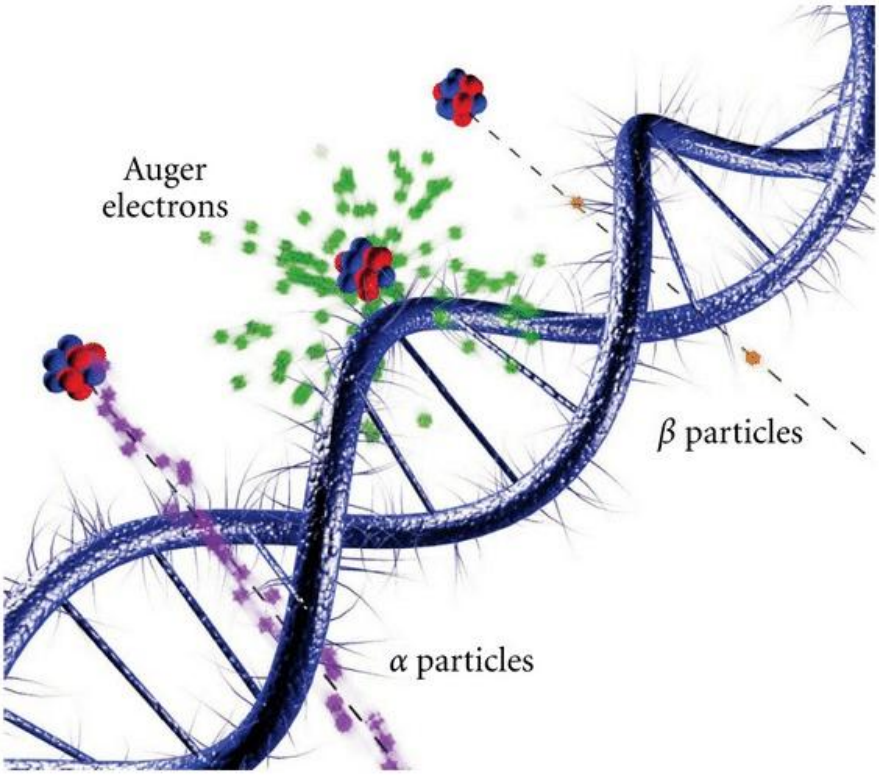

Figure 12. Interaction of ionizing radiation on the scale of DNA [51].

1.3.2 LINEAR ENERGY TRANSFER (LET)

Linear Energy Transfer (LET) is a fundamental parameter in radiobiology that quantifies the energy deposited per unit path length by an ionizing particle as it travels through matter. It's typically expressed in keV/μm or MeV cm^2/g and represents how densely ionization events occur along the particle's track [52]. LET can be defined as:

$$LET = \frac{dE_L}{dx}$$

Where:

dE_L= energy locally deposited in the medium by the particle

dx= differential path length travelled by the particle

Although LET is defined for charged particles, it can also be used for neutrons and photons (X-rays and γ rays), attributing the concept of LET to the secondary charged particles emitted by them. In general, particles such as neutrons and protons are considered high LET radiation, while X-rays, γ rays and fast electrons are considered low LET radiation. However, this definition is not absolute, as LET depends on the energy of the particle, is inversely proportional to it, and its value is not constant over time but varies along the path of the particle (Tab. 1) [53].

Initial energy	LET
Electron	
0.01 eV	2.30 keV/μm
0.1 eV	0.42 keV/μm
1 eV	0.25 keV/μm
Proton	
2 eV	16 keV/μm
5 eV	8 keV/μm
10 eV	4 keV/μm
Neutron	
14 eV	3-30 keV/μm
Carbon Ions	
10/250 MeV	170/15 keV/μm

Table 1. Examples of particles with different initial energies and their respective LET. Modified from Guerrini et al. [54].

Low-LET radiations, such as X-rays, γ rays and high-energy β^- particles, deposit energy sparsely along their path leading to isolated ionization events; in fact, they are also defined to as sparsely ionizing. High-LET radiations (heavy ions and low energy Auger electrons) produce densely ionizing tracks, generating clusters of ionizations and complex DNA damage [55].

The Linear Energy Transfer (LET) is a key factor in determining the Relative Biological Effectiveness (RBE). The RBE is defined as the ratio of a reference radiation dose to the dose of a test radiation required to produce the same biological effect. Essentially, it quantifies the increased biological damage caused by high-LET particles compared to low-LET radiation for the same absorbed dose.

$$RBE = \frac{D_R}{D_X}$$

D_R= reference dose

D_X= studied dose

High-LET radiations possess a greater RBE due to the dense ionization patterns, which increase the possibilities of irreparable double-strand breaks in DNA [56]. In the case of Auger electron cascades, although their total energy is low, their extremely short range (1–100 nm) leads to very highly localised and densely space energy deposition events, often exceeding 1000 keV/μm. This results in an exceptionally dense energy deposition pattern, capable of inducing lethal DNA damage when decay occurs near or inside the cell nucleus. Consequently, Auger emitting radionuclides illustrate how the spatial distribution of microscopic energy deposition rather than total dose alone, determines radiobiological outcomes, effectively bridging the radiation physics and molecular radiobiology [50, 57].

1.3.3 TRACK STRUCTURE

Track structure represents the non-homogeneous, stochastic, and 3D spatial pattern of energy deposition produced by ionizing radiation and its secondary particles (electrons) within matter. Therefore, it is the key aspect conferring ionizing radiation its peculiar ability in causing a wide variety of biological effects by determining the precise localization of interactions at sub-nanometre scale, crucial for understanding the relative effectiveness of different types of radiation, including DNA damage complexity (Fig. 13) [58]. The track structure depends on the type and the energy of the radiation: low-LET radiation creates sparse and isolated tracks, while high-LET radiation produces dense and highly localized tracks, formed of overlapping cluster of ionization and secondary electrons.

At macroscopic level, a charged particle track consists of dense a core typically extending over few nanometres, surrounded by a penumbra that may reach distances form 100 nm up to several micrometres depending on particles energy and LET. The core corresponds to the primary trajectory of the track where the ionization density is highest for the frequent inelastic collision. The penumbra is formed by δ-rays (secondary electrons) emitted from the core, which extend the energy deposition radially and create a gradient in ionization density [59]. From a radiobiological point of view, the analysis of the track structure connects the gap between the physical description of radiation interactions and their biological consequences. High-density tracks are associated with clustered DNA damage and complex lesions that are difficult to repair, leading to higher RBE [60]. Monte Carlo track-structure simulations, such as those developed by Nikjoo and collaborators, have been instrumental in quantifying these patterns at

nanometric resolution, enabling direct links between microscopic energy deposition and macroscopic biological endpoints.

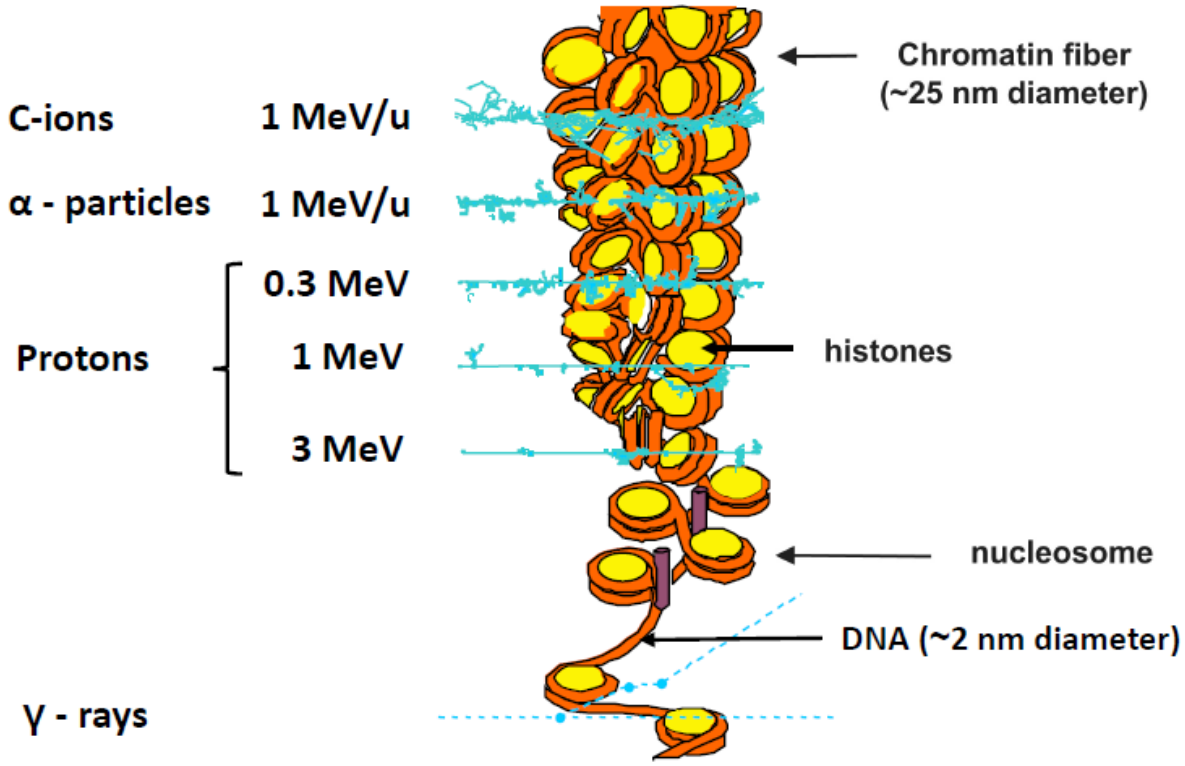

Figure 13. Schematic representation of track of sparsely and densely ionizing radiation compared with some relevant biological targets [61].

1.3.4 INTERACTION BETWEEN GOLD AND RADIATION

Gold (Au) atoms possess a high atomic number (Z=79) that increases the probability of interaction with ionizing radiation through photoelectric absorption and inner-shell ionization. When the inner-shell vacancy (K, L or M shell) is created, by radiation like X-rays, γ-rays or charged particles, gold can undergo radiative relaxation, with the emission of X-rays or a non-radiative relaxation *via* the emission of Auger electrons. In Au, the Auger electrons usually possess an energy from 50 eV to 2 keV depending on the transition that occur [62]. Recent articles of Monte Carlo track-structure simulation have demonstrated that photoionization of gold nanoparticles (AuNPs) by keV or MeV photons can produce cascades of ten to hundreds of Auger and secondary electrons [63, 64]. These electrons produce dense nanometric tracks around each AuNPs simplifying the local dose in a phenomenon known as nanoscale dose

enhancement. This mechanism underpins the radiosensitizing properties of gold nanoparticles, particularly when they are internalized near DNA or other critical targets [65]. Auger emission from Au is quantum-shell specific, and its spectral features have been experimentally characterized via X-ray photoelectrons spectroscopy (XPS) and Auger electron spectroscopy (AES), revealing multiple emission packs corresponding to MNN and LMM transitions[2] [66].

1.3.5 EFFECTS OF IONIZING RADIATION ON BIOLOGICAL SYSTEMS

When radiation interacts with a biological target, it undergoes a series of processes typically divided into three phases, distinguishable in terms of time and the characteristics of the phenomena involved. These phases are:

1. Physical phase: characterized by interaction process of radiation with matter (10^{-18}-10^{-12} seconds from the moment of interaction);
2. Chemical phase: in which ionisations and excited states are produced in the chemical structure of molecules present in the biological system (10^{-12}-1 seconds from the moment of interaction)
3. Biological phase: which includes all phenomena affecting cells as a consequence of molecular alterations induced by radiation absorption, such as cell inactivation or the induction of mutations (hours, days, months and years)

The biological phase is the particularly important because it can involve a single cell or the entire organism, triggering a series of biological modification [53].

When ionizing radiation goes throw a biological material, it could interact with biomolecules, such as nucleic acid, causing excitations and ionizations and thereby modifying the chemical structure of the molecules or atoms with which it interacts. A biomolecule can be damaged directly and/or indirectly by radiation (Fig. 14). Water is considered a biologically relevant molecule due to its abundance within cells (70-80% of a biological system) and its major role as an intermediate in the radiation-induced damage of other biomolecules

[2] "MNN" and "LMM" denote the electronic levels involved in the Auger emission process: the first letter indicates the shell where the initial vacancy is located, the second identifies the shell of the electron that fills that vacancy, and the third specifies the shell from which the Auger electron is emitted.

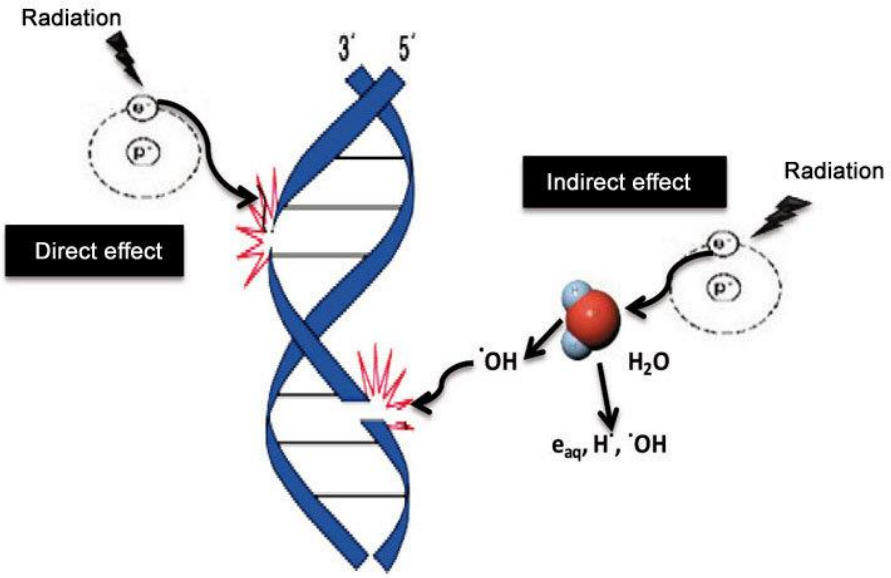

Figure 14. Direct and indirect actions of radiation. [67].

In the case of direct action, the atoms or molecules of the target are excited or ionized directly and create a pathway of events. Direct action is of greater importance with densely ionizing radiation because, due to its track, there is a higher probability that an ionizing event will occur directly in a biologically important target molecule. The probability of such events occurring depends on the concentration of the target and its volume, in relation to the volume in which it occurs [68].

Indirect action prevalently occurs when radiation, such as γ rays or X-rays, ionizes and excites molecules, which produce reactive species that in turn cause damage to macromolecules.

When discussing radiation-induced damage, the process of radiolysis of water, must also be considered, because it leads to the formation of free radicals.

The free electron, having a negative charge, can hydrate, which increases its circulation time and also increases the risk that it may cause damage to biological molecules. At the same time, e^- can encounter a water molecule, creating a negative ion H_2O^-. Both ions that are created are unstable and dissociate as follows:

$$H_2O^+ \rightarrow H^+ + {}^{\cdot}OH$$

$$H_2O^- \rightarrow H^{\cdot} + OH^-$$

The radical products form the dissociation can interact among themselves originating the following species:

$$H^{\cdot} + H^{\cdot} \rightarrow H_2$$

$${}^{\cdot}OH + {}^{\cdot}OH \rightarrow H_2O_2$$

$$H^{\cdot} + {}^{\cdot}OH \rightarrow H_2O$$

Radicals, such as $H^{\cdot}$ and ${}^{\cdot}OH$, can interact with biological compounds as enzymes, proteins and DNA, leading to the formation of radical biomolecules [53, 69]. The organic radicals can react between each other generating a cascade of reactions till producing stable modify chemical species. In particular if in the surrounding is present molecular oxygen (O_2), the radical $H^{\cdot}$ reacts and produce hydroperoxide radicals:

$$H^{\cdot} + O_2 \rightarrow HO^{\cdot}{}_2$$

These, in turn, can interact with each other, producing hydrogen peroxide.

The extent and type of biological damage depends on the specific molecules concerned and by the number of copies in which it is present. In this way damage at enzyme or proteins presents in a high level or play a minor role, can be negligible. On the other hand, molecules that play a highly significant role or are present at low levels can cause damage to cells if they are damaged.

Radiation can cause damage in the cytoplasm at the level of the various organelles present there. The endoplasmic reticulum (ER) is essential for cell life as it regulates Ca^{2+} storage, the synthesis of proteins, glycosylation and the protein transport to the membrane or secretory pathways. Disruption of these processes by radiation can lead to ER stress, which, if prolonged, leads to the activations of specific pathways that are grouped under the name of unfolded protein response (UPR). Sustained UPR activation often leads to cell death by apoptosis or autophagy [70].

In mitochondria, the radiation can directly promote the release of cytochrome C (Cyt-c) through the release of ROS or through the activation of Cyt-c-induced apoptosis, causing altered permeability both *in vivo* and *in vitro*. Once released into the cytoplasm, Cyt-c forms a complex

with the apoptotic factor Apaf-1, which recruits caspase-9, which activates downstream apoptotic pathways mediated by caspase-3 and caspase-7 [71].

Lysosomes are important cellular organelles that are responsible for digesting various macromolecules and, for this purpose, have a lumen rich in hydrolases. If the lysosome membranes are damaged by radiation, the hydrolases are released into the cytoplasm, causing the digestion of all macromolecules.

Finally, the cytoplasmic membrane can be damaged either directly or indirectly. In the first case, physical damage involves the macromolecules, i.e. the structure of the membrane is damaged, and permeability, integrity and mobility are altered. In the second case, the damage occurs through the action of ROS and RNS (Reactive Nitrogen Species), which disrupt cellular signalling pathways. In addition, radiation can directly activate sphingomyelinases, which destroys the polar components of the membrane [72].

1.3.5.1. DNA DAMAGE

Radiation-induced damage to DNA is very dangerous because DNA is present in a single copy and contain all the genetic information necessary for the correct functioning of cells. DNA damage may be caused by the direct deposition of energy in the molecule, in general due to highly ionizing radiation (heavy ions or Auger electrons), or by interactions with radicals produced by radiolysis of water following exposure to sparsely ionizing radiation (X-rays and γ rays) [73].

The energy deposition causes damage to all three components of nucleotide (base, deoxyribose sugar and filaments). The breaking of filaments results in single-strand breaks (SSBs), when only one the filament is affected, or double-stand breaks (DSBs), when both filaments are interested (Fig. 15). DSBs represent lesions responsible for chromosomal aberrations and cell death. Cell lethality seems to be related to the failure of the repair systems given that the breaks are present in both the DNA's filaments [74].

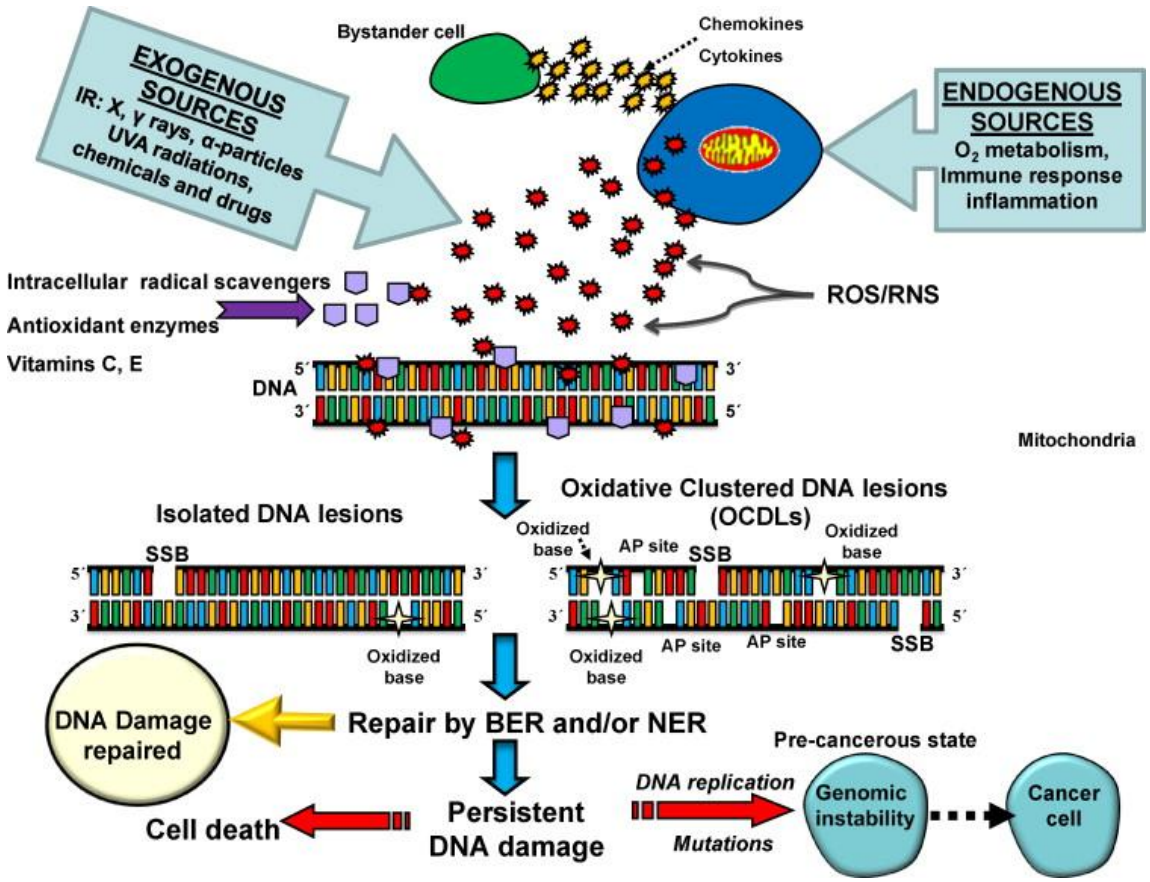

Figure 15. Schematic representation of DNA damage by ionizing radiation and the repairing systems [75].

As is well known, DNA is in a hydrated state and is therefore surrounded by water molecules. When these molecules are hit by radiation, they can lead to the formation of the above-mentioned radical species, which may cause DNA damage to various degrees, up to the extent that the cell becomes non-viable. One of the most frequent non-lethal mutations occurs at the level of the nitrogenous bases. In fact, both thymine and guanine are targets of the ·OH radical. In the specific case of guanine, 8-oxo-7,8-dihydroguanine is produced by the addition of the hydroxyl radical at C8 position of the purine ring, whereas for thymine, interaction with the ·OH radical at position 5 or 6 of the ring produce thymine glycol. The two main repair systems (Fig. 15) for this type of damage are base excision repair (BER) and, to a lesser extent, nucleotide excision repair (NER) [75].

Regarding single-strand breaks (SSBs), it has been observed that a large number (that is 1000) of SSBs can be generated even at relatively small doses (~1 Gy) in a dose dependent manner. However, this type of damage is efficiently repaired: the initial condition is restored in about

15 minutes using the intact strand as a template to synthesize the strand that has been damaged. For this reason, this type of damage does not cause cell death [76].

Double-strand breaks (DSBs) can be produced either by a single ionization event affecting both strands, or by two independent ionization events that produce closely spaced SSBs on the complementary strand. Again, a relationship between DSBs and dose has been demonstrated, but only at low doses. There are two mechanisms capable of repairing DSBs: non-homologous end joining (NHEJ) and homologous recombination (HR) (Fig. 16). The first repair system is prone to error because there is no strand that can be used as a template, so the broken part is simply removed, and the two DNA ends are joined together by DNA ligase. The second system of repair is more accurate and can be carried out during the cell replication process, in which two copies of the genome are present. If radiation induces a DSBs, after DNA replication, the copy of DNA that has not been affected by the lesion can be used as a template to synthesize the missing part on the strand where the DSB occurred [77, 78, 79].

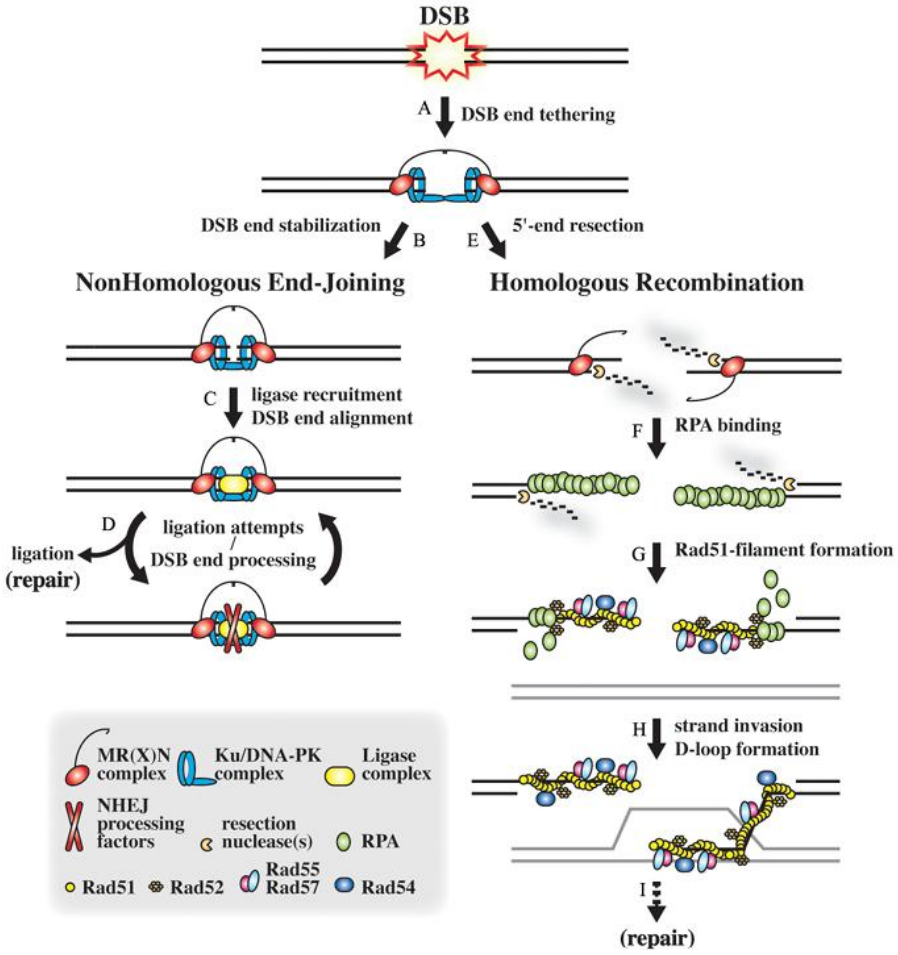

Figure 16. Model of DSB repair by NHEJ and HR pathways [79].

1.4. SYNCHROTRON CHARACTERIZATION

Synchrotron Radiation (SR) is a highly specialized electromagnetic emission generated when relativistic charged particles (electrons or positrons), confined within an ultra-high vacuum environment like a storage ring, are accelerated along curved trajectories by external magnetic fields. This process endows SR with several exceptional properties, including high brilliance (photons per second per unit source size, divergence, and bandwidth), narrow angular collimation, broad spectral range spanning from infrared to hard X-rays, a pulsed time structure, and a high degree of polarization. These unique characteristics have established SR facilities, such as Elettra Sincrotrone Trieste, as versatile platforms essential for advanced research across diverse domains including materials science, molecular physics, and nanotechnology, where the radiation is harnessed for techniques like XAS, XRD, and specifically, X-ray Photoelectron Spectroscopy (SR-XPS). The adoption of SR in XPS confers substantial advantages over conventional laboratory sources, leading to a marked improvement in spectral quality, enhanced surface sensitivity, and significantly faster data acquisition due to the higher photon flux. Crucially, the tunability of the photon energy ($h\upsilon$) in SR-XPS allows for two powerful capabilities: first, maximizing the photoemission cross-section for core-levels of interest (e.g., S 2p in diluted species) to obtain high-resolution spectra from complex, low-concentration materials; and second, performing depth profiling. By varying $h\upsilon$, the kinetic energy of the photoelectrons is changed, thereby modulating the information depth (governed by the inelastic mean free path), which enables the selective investigation of distinct layers, such as the stabilizing molecule/nanoparticle interface versus external physiosorbed layers, a capability paramount for the structural and electronic characterization of the chemically stabilized noble metal nanoparticles investigated in this PhD thesis [80, 81].

1.5. SEGNAR PROJECT

The project Synergistic Effect of Gold Nanorods And Radiopharmaceutical (SEGNAR) is a 3-year project founded by Istituto Nazionale di Fisica Nucleare (INFN) and it started in January 2023. The basic idea is the realization of a conjugated AuNR-radiopharmaceutical system for diagnosis and therapy. The functionalization of AuNRs for targeting the nucleus of tumour cells, the radiopharmaceutical loading of the functionalized AuNRs and the study of Auger electrons emission from AuNRs subjected to gamma irradiation are some of the first challenges that the project has to solve to achieve this proof of concept. Another main goal of the project is the modelling of the AuNRs system in the cell environment in order to predict the potential radiobiological enhancement of radiation-induced biological effects trying to elucidate the possible mechanism and to identify possible synergistic effects between Au form AuNRs and ^{99m}Tc-sestaMIBI radiopharmaceutical. To achieve these objectives several experiments are performed to study the effects of the AuNRs in different configurations and concentrations when irradiated with gamma rays. Structural and physical characterization of AuNRs together *in vitro* biological studies on T98G cells with the use of several assays (e.g. Magnetic Resonance Spectroscopy - MRS) allows us to assess the AuNRs cytotoxicity and the metabolic alterations in tumour cells allowing to exploit the synergic effect of the AuNR-TAT-^{99m}Tc-sestaMIBI. More detailed regard the TAT and the radiopharmaceutical will be provided in the Materials and Methods section.

The project is structured into five work packages (WPs), which have the following objectives:

1. WP1 Modelling: Theoretical and modelling studies to highlight possible synergic effects of modified AuNR-TAT and radiopharmaceutical based on ^{99m}Tc-sestaMIBI;

2. WP2 Synthesis, functionalization and conjugation: Preparation and preliminary structural characterization of modified AuNRs-TAT and AuNRs-^{99}Tc-sestaMIBI and AuNRs-TAT-^{99}Tc-sestaMIBI and stability studies;

3. WP3 Characterization and Auger emission studies: Structural and diagnostic characterization of AuNRs and AuNRs-TAT modified systems and their conjugates with ^{99}Tc-sestaMIBI and AuNRs-TAT-^{99}Tc-sestaMIBI;

4. WP4 *In vitro* biological studies. *In vitro* evaluation of cytotoxicity and AuNRs stability, with and without irradiation, across the three configurations (AuNRs, AuNR-TAT, and AuNR-TAT-^{99}Tc-sestaMIBI). Magnetic resonance spectroscopy (NMR) will be used to assess metabolic changes following AuNR incorporation and irradiation. Additionally, ultrastructural studies will determine the intracellular distribution and morphological changes induced by the three configurations.

5. WP5 Studies with radiopharmaceutical: Preliminary evaluation with test *in vitro* using AuNRs-TAT-^{99m}Tc-sestaMIBI;

This PhD research was integrated into WP2 and WP4. Specifically, I was responsible for the full development of WP2. Regarding WP4, my core contribution involved assessing toxicity and DNA damage, whereas stability assessments and ultrastructural studies were performed through active collaboration with project partners

2. EXPERIMENTAL DESIGN AND SET UP

2.1. MATERIAL AND METHODS

2.1.1. INSTRUMENTATION

Centrifuge

Nanorods were purified using an Eppendorf Mini Spin centrifuge with 12-position rotor for 1.5 mL microcentrifuge tubes.

UV-Visible Spectroscopy (Uv-Vis)

Uv-Visible spectra were recorded with a Shimadzu 2401 PC spectrophotometer, operating in double beam configuration, where one ray was exposed to a referent solution (containing only the solvent solution of bidistillate water) while the other probed the solution of study. Spectra were acquired in the 200-800 nm range with a spectral resolution of 1nm. Quartz cuvettes (4 mL volume, 1 cm optical path length) were used for all measurements.

Fourier Transform Infrared Spectroscopy (FT-IR)

FT-IR measurements were performed using a Bruker Vector 22 spectrophotometer. A detailed description of the experimental setup is provided in Section 2.1.6 (Structural Characterization).

Synchrotron Radiation-induced X-ray Photoelectron Spectroscopy (SR-XPS)

SR-XPS measurements were carried out at different Synchrotron Radiation facilities and beamlines. Beamlines characteristics will be described in detail for sample and experiment in the section 2.1.6 Structural characterization.

Near Edge X-ray Absorption Fine Structure (NEXAFS)

NEXAFS experiments were carried out at Elettra Synchrotron Radiation implant in Italy (Basovizza - TS) at the BEAR beamline. The beamline description will be reported in detail in the section 2.1.6 Structural characterization.

High-resolution transmission electron microscopy (HR-TEM)

Morphological characterization of the materials was achieved with High-Resolution Transmission Electron Microscopy in collaboration with the NIMP (Nation Institute of Material Physics) research center in Magurele, Bucharest, Romania operated at 200 kV. The JEOL JEM ARM 200F microscope is suitable for morphological characterization of nanostructured materials with a focus on structural characterizations down to atomic resolution of extended defects in crystalline materials and strain fields associated with extended defects and interfaces. The instrument is equipped for Energy-Dispersive X-ray Spectroscopy (EDS) and Electron Energy Loss Spectroscopy (EELS) measurements, allowing the determination of a material's elemental composition. Accelerating voltages: 120, 200 kV, TEM magnification: 50 – 2 000 000 ×, TEM resolution: 0.19 nm, EDS energy resolution: 131,4 eV (Mn-Ka). Samples were deposited via drop-casting on a copper, gold or nickel coated silicon oxide mesh.

Gamma Ray

Irradiation was performed using a Gammacell 40 Exactor equipped with a Caesium-137 (^{137}Cs) source. The dose rate was 0.653 Gy/min. Cells were irradiated in culture flasks or 96-well plates. No more than two samples were irradiated simultaneously, and all samples were positioned centrally within the chamber to ensure uniform dose distribution.

Cell counter

Cell counts were performed using a Beckman Coulter Z2 particle counter, with size thresholds set between 9 µm and 27 µm. A total of 0.5 mL of stained cell suspension was diluted in 9.5 mL of isotonic solution. Two 0.5 mL aliquots were measured, and the counts were averaged and multiplied by the dilution factor (20) to determine the final cell concentration.

Optical microscope

Cell morphology and culture conditions were monitored using a Leica DMIL optical microscopy.

LUMIstar Omega

Cell viability measurements were performed using a LUMIstar Omega microplate reader (single luminescence channel). Data acquisition was controlled using Omega Reader Control Software, allowing adjustment of plate type, gain, and emission settings. Data were initially processed using MARS Data Analysis Software.

Dynamic Light Scattering (DLS)

Particle size distribution and ζ-potential measurements were performed using a Zetasizer Ultra RED. All measurements were carried out in bidistilled water.

Confocal microscopy

Observations were made using a Zeiss LSM 980 confocal laser scanning microscope with Airyscan2. 40x and 63x oil immersion objectives were used to obtain high-resolution images. The spectral excitation laser lines used included 405, 488, 546, 594, and 633 nm, corresponding to the excitation wavelengths of the fluorochromes used. The images were acquired in z-stack mode to obtain optical sections along the z-axis of the sample, allowing three-dimensional analysis of the observed structures. The analyses were performed using ZEN 3.3 software.

TEM microscopy for cells

T98G cells were seeded in 12-well plates and, once 80% confluence was reached, were treated with AuNR-TAT at a concentration of 50 μg/mL for 1, 6 and 24 hours. After fixation in 2.5% glutaraldehyde in 0.1M cacodylate buffer for 1 hour, the cells were washed with cacodylate buffer three times and post-fixed in 1% osmium tetroxide for 1 hour. They were then dehydrated using a series of increasing concentrations of ethyl alcohol and embedded in epoxy resin. After polymerisation at 60 °C for 48 h, the samples were sectioned with an ultramicrotome and sections of approximately 70 nm were stained with alternative Uranyl acetate and lead citrate dyes. Observation was performed using a FEI 208S transmission electron microscope (FEI Company, Hillsboro, OR, USA) and images were acquired using the Mega-view II SIS acquisition system (Olympus, Hamburg, Germany).

Chemical for AuNRs synthesis

The following reagents were used as received:
Tetrachoroauric (III) acid trihydrate ($HAuCl_4 \cdot 3H_2O$, ≥99.9% Sigma-Aldrich, St. Louis, MO, USA), Cetyltrimethylammonium bromide (CTAB) ($C_{19}H_{42}BrN$, ≥97% Merck, Rahway, NJ, USA), Sodium borohydrate ($NaBH_4$, 99.99% Aldrich, St. Louis, MO, USA), L-ascorbic acid ($C_6H_8O_6$, AA, 99% Sigma, St. Louis, MO, USA), Silver nitrate ($AgNO_3$ 99.9%, Aldrich), and MilliQ H_2O were used as received.

Cell culture

Human glioblastoma multiform cells (T98G cells) were purchased from the European Collection of Authenticated Cell Cultures (ECACC, UK Health Security Agency). Dulbecco's MEM Nutrient Mix F12 medium (DMEM-F12; Euroclone S.p.A., Pero, Italy), fetal bovine serum (FBS; GIBCO®, Life Technologies, Waltham, MA, USA), glutamine (Euroclone S.p.A., Italy), penicillin and streptomycin (Euroclone S.p.A., Italy).

2.1.2. AuNRs SYNTHESIS AND PURIFICATION

Gold nanorods (AuNRs) were synthesized using a seed-mediated growth method adapted from the literature (Fig. 17) [38]. The seed solution was prepared by mixing 5 mL of 0.2 M CTAB and 5 mL of 0.5 mM $HAuCl_4$ in a round-bottom flask under magnetic stirring (700 rpm). The solution was degassed with argon for 3 minutes. Subsequently, 600 μL of freshly prepared $NaBH_4$ solution were rapidly injected under vigorous stirring initiating the reduction of Au^{3+} ions. The solution colour change form intense yellow to a brownish-yellow indicating nanoparticles seed formation. Stirring was continued for 5 minutes.
The growth solution was prepared by mixing 5 mL of 0.2 M CTAB and 5 mL of 0.05 mM $HAuCl_4$. Then 200 μL of 4 mM $AgNO_3$ were added. The mixture was stirred and degassed with argon form 3 minutes. After degassing 70 μL of 0.078 M ascorbic acid were added, resulting in complete discoloration of solution due to the reductio of Au^{3+} to Au^{1+}. Finally, 24 μL of the previously prepared seed solution was introduced under gentle stirring. The reaction was left under. A gradual colour change from transparent to pale pink was observed after approximately 15 minutes, indicating nanorod growth. The suspension was then left undisturbed at room temperature for 24 hours to complete the growth process.

AuNRs were purified by two centrifugation cycles at 13,000 rpm for 15 minutes. The supernatant was discarded after each cycle, and the pellet was resuspended in bidistilled water.

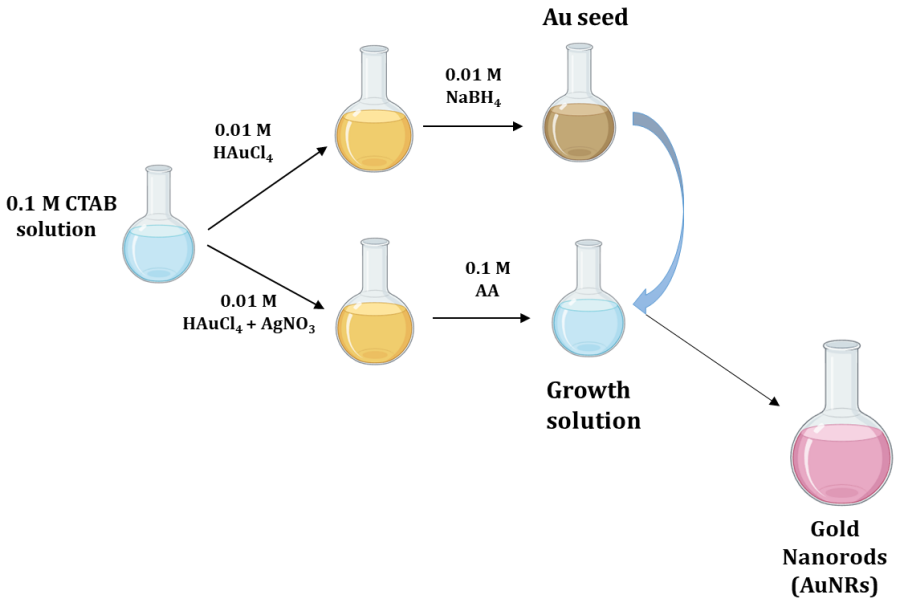

Figure 17. Two step synthesis scheme [82].

2.1.3. CONJUGATION WITH ^{99M}TC

Preparation of ^{99m}Tc

^{99m}Tc-sestaMIBI (Fig. 18) 99mTc-sestaMIBI (methoxyisobutylisonitrile) was selected as the radiopharmaceutical. Radiolabelling was performed according to the manufacturer's instructions (STAMICIS®, Curium Pharma, UK). The lyophilized kit was reconstituted with 3 mL (11.1 GBq) of freshly eluted 99mTcO$_4^-$ obtained from a ^{99}Mo/^{99m}Tc generator (Ultratechnekow FW, Curium Pharma). The vial was heated at 100 °C and subsequently incubated at room temperature for 15 minutes. Radiochemical purity (%RP) was evaluated using aluminium oxide chromatography strips with ethanol as the mobile phase. Radiochromatographic analysis was performed using a Cyclone Plus® system (PerkinElmer), and %RP was quantified with OptiQuant® software. After quality control, the product was stored at 4 °C until complete radioactive decay. The resulting long-lived ^{99}Tc-sestaMIBI was then used for loading onto AuNRs. [83].

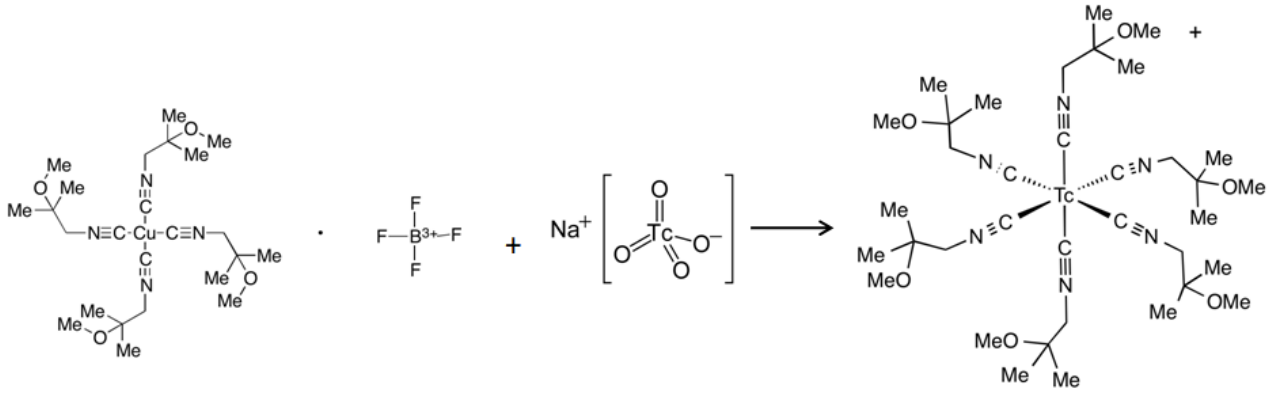

Figure 18. ^{99m}Tc-sestaMIBI preparation.

Loading onto AuNRs

To evaluate the loading efficiency, two independent experiments were performed, each in technical triplicate. A solution containing 4 mL of 0.0165 mg/mL 99Tc-sestaMIBI was mixed with 1 mL of AuNR suspension (1 mg/mL) under magnetic stirring for 30 minutes. The mixture was centrifuged at 13,000 rpm for 20 minutes. The pellet was stored at −20 °C, while the supernatant was analysed by UV–Vis spectroscopy to estimate loading efficiency.

2.1.4. CONJUGATION WITH TAT PEPTIDE

Synthesis of TAT (made by university of Parma.)

The TAT peptide was modified starting from cell-penetrating peptides (CCPs) present in the human immunodeficiency virus type 1 (HIV-1). Frankel and colleagues [84] discovered that the TAT peptide can enter in cell and translocate into the nucleus. CPPs present a breakthrough as delivery systems for macromolecules. CPPs are capable of entering the body in a non-invasive manner, do not destroy the integrity of cellular membranes, and are considered highly efficient and safe. Thus far, CPPs have been used to safely deliver peptides, proteins and nucleic acids that are generally difficult to deliver due to some of their inherent properties. The CPPs has been used with a wide variety of cell types and in combination with different cargos. However, the exact mechanism CPPs use to cross cell membranes is still an unsolved issue. It is well known that CPPs use different mechanisms to enter into cells. In general, the mechanisms can be associated to two broad groups: endocytosis and direct penetration. In the literature, it is described that many CPPs use different uptake pathways depending on their

structure, net charge, concentration, type of cargo, cell lines used, temperature at which uptake studies were conducted and incubation times. Basically, the TAT's domain encompassing amino acids 38–58 (the basic region of TAT) maintaining the property of transduction enabling both its nuclear and cytoplasmic accumulation [85]. The basic region of TAT as that of the HIV-1 original protein didn't have groups that can permit the loading on a gold surface. As well-known there are many ways to functionalize the AuNRs surface. One of the most fruitful functionalization methods is definitely the direct thiol reaction, which allows stable binding between the molecule and the nanorods. Santos-Cuevas et al. have provided the solution of how to label the TAT on the surface by modifying the carboxyl terminal adding a free cysteine. In this case is the thiol group that permit the loading [86, 87].

This work optimizes the synthesis of gold nanorods and their functionalization with a suitably modified TAT peptide to allow for cell nucleus growth. Various chemical and physical characterizations were performed to verify and optimize the system, such as DLS and Z-potential measurements, and UV-vis and FT-IR spectroscopies. Furthermore, the structural characterizations conducted using synchrotron radiation were crucial and confirmed the amazing perspective of this system in nanomedicine.

A TAT peptide solution (8×10^{-3} M, 5 mL) was prepared.

Two milliliters of this solution were mixed with 1 mg of AuNRs (2 mL of 0.5 mg/mL suspension) under magnetic stirring. The reaction mixture was incubated for 2 hours at room temperature. Following incubation, the suspension was centrifuged at 13,000 rpm for 15 minutes to remove unbound peptide. The supernatant was discarded, and the pellet was collected. The functionalized AuNR-TAT nanoconstructs were stored at room temperature in the absence of excess solvent.

(Fig. 19).

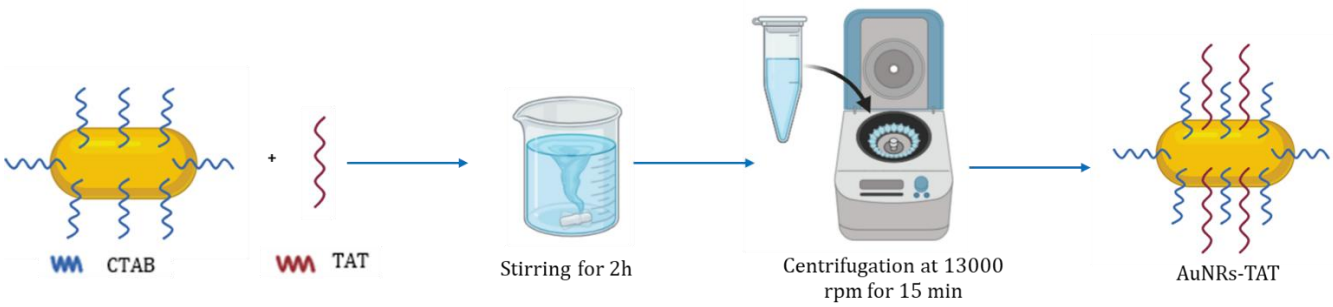

Figure 19. Schematic representation of modified TAT peptide [82].

2.1.5. DLS MEASUREMENT

After the purification the AuNRs were resuspended in bidistilled water to obtain a solution with a concentration of 0.5 mg/mL. The suspension was put in a special zeta potential cell equipped with electrodes, through which an electric field is applied, and in this way the particles are charged. The charged particles migrate toward the opposite charged electrode. The AuNRs are illuminated with a laser and the light and the scattered light from the AuNRs experiences a frequency shift. The instrument detects this frequency shift and calculates the electrophoretic mobility (μ_e) of the particles. The software converts the μ_e in zeta potential (ζ) using the following equation:

$$\zeta = \frac{\eta \mu_e}{\varepsilon}$$

Where:

η= viscosity of the medium

μ_e= electrophoretic mobility

ε= dielectric constant of the medium

2.1.6. STRUCTURAL CHARACTERIZATION

2.1.6.1 SYNCHROTRON RADIATION INDUCED X-RAY PHOTOELECTRON SPECTROSCOPY (SR-XPS)

The characterizations were carried out at the SuperESCA beamline at the ELETTRA synchrotron facility in Triste (Italy). Different experiments were carried out but in general for C1s, N1s, O1s and Ag3d regions a photon energy (PE) of 600 eV was used, instead Au4f, Tc3d, S2p and Br3d core levels were measured with PE=260 eV, as to maximize signals intensity and to optimize the resolution. The energy resolution was between 100 and 250 meV depending on the experiment carried out. All samples were measured in solid state on thick films prepared by drop-casting a drop of aqueous solution on TiO_2/Si(111) wafers surfaces.

2.1.6.2 Near Edge X-ray Absorption Fine Structure (NEXAFS)

Spectra were performed at the BEAR beamline at the ELETTRA synchrotron. All experiments were performed on thick films of samples prepared from aqueous solution by drop-casting on Au/Si(111) wafers surfaces. C K-edge, N K-edge, and O K-edge spectra were acquired with the incident X-ray beam striking the sample surface at a grazing angle of 20°, optimizing the signal intensity. To ensure accurate energy calibration, the carbon K-edge spectra were aligned using the C=O 1s→π* resonance at 288.70 eV, while the nitrogen K-edge spectra were referenced to the peptide bond 1s→π* transition at 402.00 eV.

2.1.6.3 Reflection-Absorption Infrared Spectroscopy (RAIRS)

The analyses were conducted on thin films of cys-TAT and Au-NRs-cys-TAT, prepared by casting aqueous solutions onto Au-coated Si(111) substrates. Infrared spectra were acquired in the 400–4000 cm^{-1} range with a spectral resolution of 1 cm^{-1}, using a VECTOR 22 FT-IR spectrometer (Bruker). The instrument consists of a source Michelson interferometer, a sample housing compartment and a DTGS detector operating in the range wavenumber 400-4000 cm^{-1}, at a resolution of 1 cm^{-1}. The spectrophotometer uses a Glocar source, consisting of a silicon carbide (SiC) rod that is heated by the Joule effect through a resistor to a temperature, approximately T = 1500 °C. FT-IR spectra were recorded in reflectance mode by means of a Specac P/N 19650 series monolayer/grazing angle accessory; the infrared beam was directed onto the sample surface at a grazing incidence angle of 20° to enhance surface sensitivity.

2.1.7. BIOLOGICAL CHARACTERIZATION

The T98G cells were grown in a monolayer at 37 °C in a humidified atmosphere of 95% air and 5% CO_2, in DMEM-F12 medium supplemented with 10% fetal bovine serum, 1 mM glutamine, and 50 U/dm^3 penicillin and streptomycin, with a doubling time of 27 h. To ensure the success of the experiments, the cells were thawed at least one week before and the first passage was always carried out in T75 flask with freshly prepared medium.

2.1.7.1 COLONY-FORMING ASSAY

To investigate the effect of a combination between the AuNRs toxicity and the radiation-induced damage, a colony-forming assay was performed, based on classical clonogenic survival [88, 89].

To better investigate the effects of the AuNRs on T98G cells, first survival experiments were carried out with different concentrations of AuNRs. After the validation of the right concentration of AuNRs, a complete experiment involving two treatments was conducted. To carried out the experiment, 48h before the irradiation, the cells were seeded at a density of 8x10^3 cells/cm^2 in T25 flasks. At 24h before irradiation, the cell culture medium was removed from each flask and replaced with 10 mL of fresh medium or medium enriched with AuNRs in two different concentration (0.1 and 0.5 μg/ml). On the irradiation's day, all medium was removed, and fresh medium was added to the flask 1h before irradiation. The cells were irradiated with two different radiation doses (i.e. 1 and 4 Gy). After irradiation, cells were detached from the flask by using trypsin, counted, and reseeded at the appropriate density. For each sample, 6 cm Petri dishes were prepared four with a final volume of 5 ml. The number of cells seeded per dish depends on the treatment and it was calculated to obtain a final range of 300-600 colony for each sample. The samples were leave in incubation for 12 days and then they were stained with crystal violet. At this point, only the colonies containing at least 50 cells were manually scored and considered as surviving cells. The average colony count from the four Petri dishes was used to calculate the plating efficiency (PE) that is defined as number of colonies counted divided by the number of cells plated. For each experiment, cell-surviving fractions (SF) were calculated as the ratio between the PE measured in the investigated sample and the PE of the corresponding control (Fig. 20).

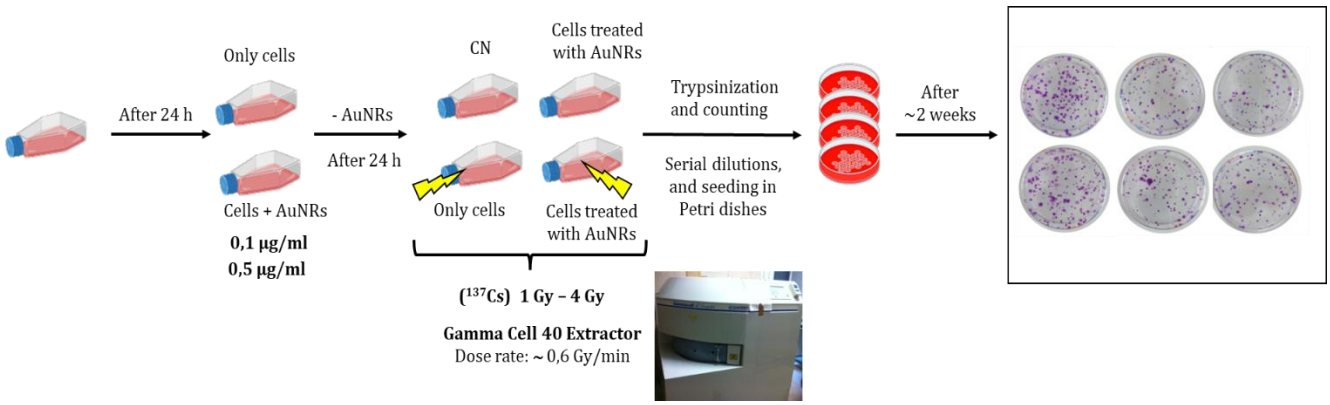

Figure 20. Colony forming assay scheme.

2.1.7.2 REALTIME-GLO ™ MT CELL VIABILITY ASSAY VALIDATION PROTOCOL

The RealTime-Glo™ MT cell viability assay is a nonlytic method to measure in an indirect way, by the measuring the reducing potential of cells and thus metabolism, the viability of cells. The assay consists of two components: the luciferase enzyme (NanoLuc® Enzyme) and a prosubstrate (MT Cell Viability Substrate) that are added to the cell in a concentration 1X at 37°C. The prosubstrate is internalized by the cell, meanwhile the enzyme remains in the media. Inside the cells the prosubstrate is reduced inside and tourn into the active luciferase substrate. At this point the active substrate exits from the cells and is rapidly used by the enzyme, preventing accumulation in the medium. When the cells are dead, they do not produce the active substrate, because their metabolism is not active, and any luminescence is observed [90, 91].

One day before the AuNR treatment, the cells were seeded at $2x10^3$ cells/well in 100 µL in a 96 well plate. White plates with transparent bottoms were used to isolate the luminescence of individual samples. After 24h, all the medium was removed and different concentrations of AuNRs, with and without TAT, were added to the wells; the control (Ctrl) received fresh medium. The day after, in all the sample, the medium was removed again and replaced with fresh medium. 48h later, medium was removed and the medium containing the prosubstrate and the enzyme was added. After 10 minutes, luminescence was measured using LumiStar reader (Fig. 21).

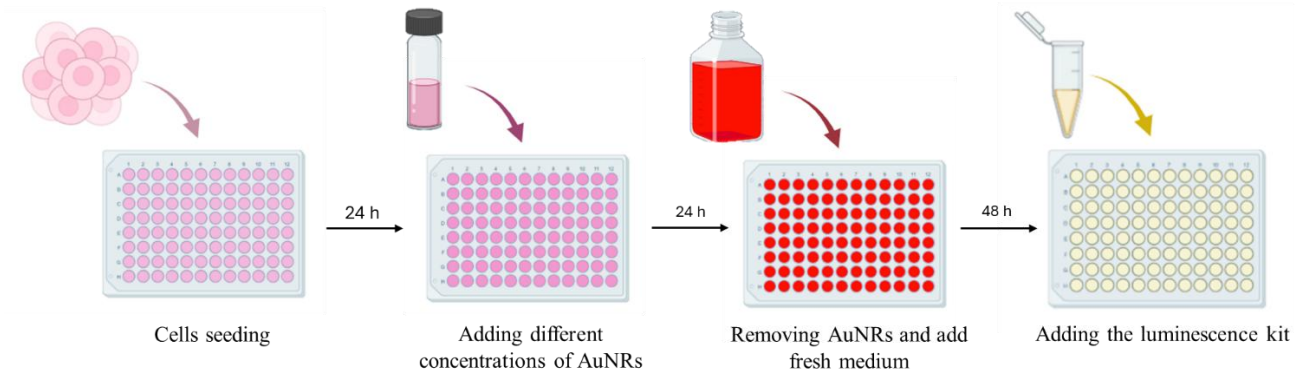

Figure 21. Schematic representation of RealTime-Glo™ MT cell viability assay [82].

2.1.7.3 γ-H2AX ASSAY VALIDATION PROTOCOL

Five days prior to irradiation, $5x10^5$ cells were seeded in T25 flasks with 10 mL of culture medium to reach 90–100% confluence, thereby inducing cell cycle arrest in the G0 phase via contact inhibition. Two days before irradiation, at 10 AM, 50 µg/mL of AuNR-TAT were added to the designated flasks. The following day (18h before irradiation), to ensure that the majority of the cell population remained in the G0 phase at the time of exposure, the AuNRs were removed, and the cells were re-seeded in slide flasks at a density of $5x10^5$ in 3 mL of medium. On the irradiation day 1 or 2 slide flasks for each dose were irradiated, this was done to ensure a backup sample. The cells were incubated at 37 °C for different time point (30 min, 1h, and 2h) and then fixed. For the fixation, all medium was removed, and cells were washed twice with PBS, followed by 2 mL of 2% PFA for 10 minutes in ice. At the end of the time, 3 washes with PBS, of 5 minutes each, were performed, and then 2 mL of PBS with 0.5% of TritonX was added for 5 minutes at room temperature (RT). The blocking was performed with 2 mL of 2% BSA for 30 minutes at RT. When time runs out, BSA was removed, and the slide flasks were opened. 60 µl of the primary antibody were put on the slide, covered with parafilm, and incubated in humid chamber for 2h at 37°C, at the end, 3 PBS washes were done. Then, 60 µl of the secondary antibody were added and the slide covered with parafilm, left at the dark at RT for 1 h 4 PBS washes were performed and finally the slides were mounted with the Vectashield and cover slips.

3. RESULTS AND DISCUSSION

3.1. SYNTHESIS AND CONJUGATION OF AUNRS

AuNRs exhibit characteristic localized surface plasmon resonance (LSPR) properties, which allow rapid preliminary characterization by UV–Visible spectroscopy. Specifically, AuNRs display two distinct plasmon bands corresponding to transverse and longitudinal oscillation modes. Several synthesis batches were performed to achieve reproducible and standardized morphological features. The optimized synthesis yielded AuNRs with average dimensions of 39 ± 5 nm in length and 11 ± 2 nm in width, corresponding to an aspect ratio (AR) of approximately 3.5. The UV–Vis spectrum of the AuNRs dispersed in water showed a transverse plasmon band centered at 500–515 nm and a longitudinal plasmon band in the 720–800 nm range (Fig. 22a). These values are consistent with nanorods possessing an aspect ratio of ~3.5. Transmission Electron Microscopy (TEM) analysis confirmed the nanoscale dimensions and low polydispersity of the synthesized nanorods. The measured average length was 39 ± 5 nm and the average width was 11 ± 2 nm, in agreement with spectroscopic data. The calculated aspect ratio was 3.5 (Fig. 22b).

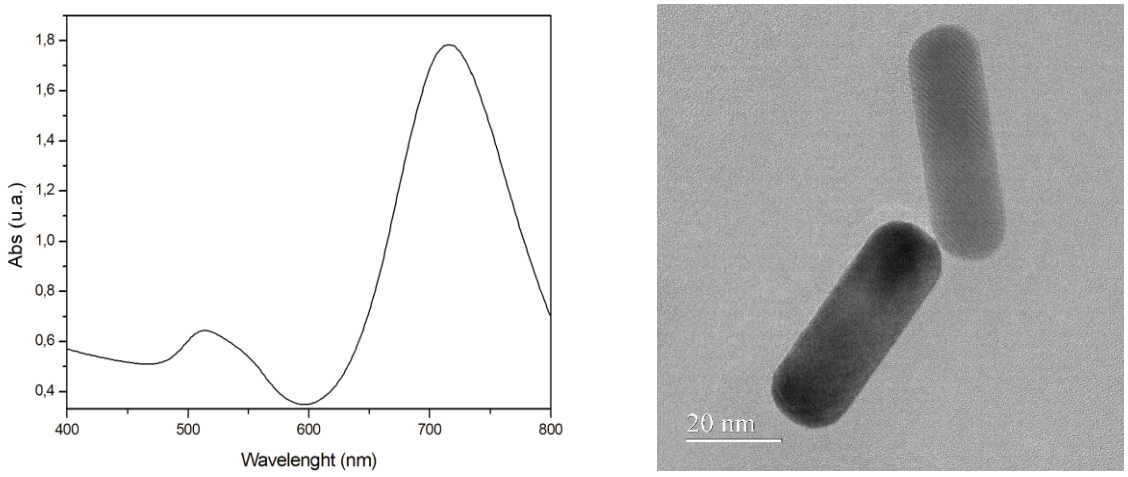

Figure 22. (a) UV–Vis spectrum of AuNRs showing transverse and longitudinal plasmon bands (514–720 nm); (b) TEM image of the corresponding AuNR sample.

To quantify the loading efficiency of 99Tc-sestaMIBI onto AuNRs, a calibration curve was constructed using known concentrations of the drug ($y = 55.409x$; $R^2 = 0.999$) [92]. The loading efficiency (η%) was calculated according to the following equation [93]:

$$\eta(\%) = (m_{\text{loaded drug}}/m_{\text{drug}})\ 100$$

The loading efficiency was determined to be 5 ± 2%, corresponding to 0.0033 mg of drug per 1 mg of AuNRs..

AuNRs were subsequently functionalized with TAT peptide to promote potential nuclear targeting. After 2 hours of incubation between AuNRs and the peptide solution, the conjugates were purified by centrifugation and characterized. UV–Vis spectroscopy was used to verify peptide attachment. The spectrum of bare AuNRs (Fig. 23, green line) and free Cys-TAT peptide (Fig. 23, black line) were first recorded. The spectrum of AuNR–Cys-TAT conjugates (Fig. 23, red line) showed the characteristic absorption feature of TAT (highlighted by the pink bar), confirming successful peptide immobilization on the AuNR surface.

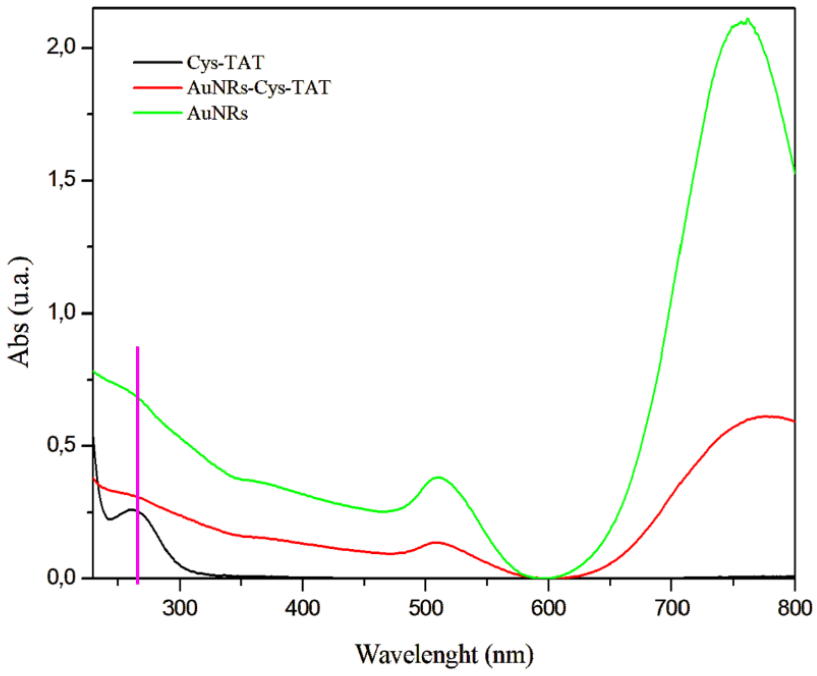

Figure 23. Comparison between Cys-TAT (black), AuNRs (green), and AuNR–Cys-TAT conjugates (red). The highlighted region (pink bar) indicates the characteristic TAT absorption band confirming surface functionalization.

TEM analysis was performed to evaluate morphological changes after peptide conjugation (Fig. 24).

AuNR–Cys-TAT samples exhibited a higher degree of aggregation, likely due to thiol-mediated interparticle interactions and possible disulfide bond formation between peptides. In contrast, AuNR–Acm-TAT samples showed reduced aggregation, attributed to the presence of the Acm protecting group on cysteine, which prevents disulfide bond formation and limits interparticle crosslinking

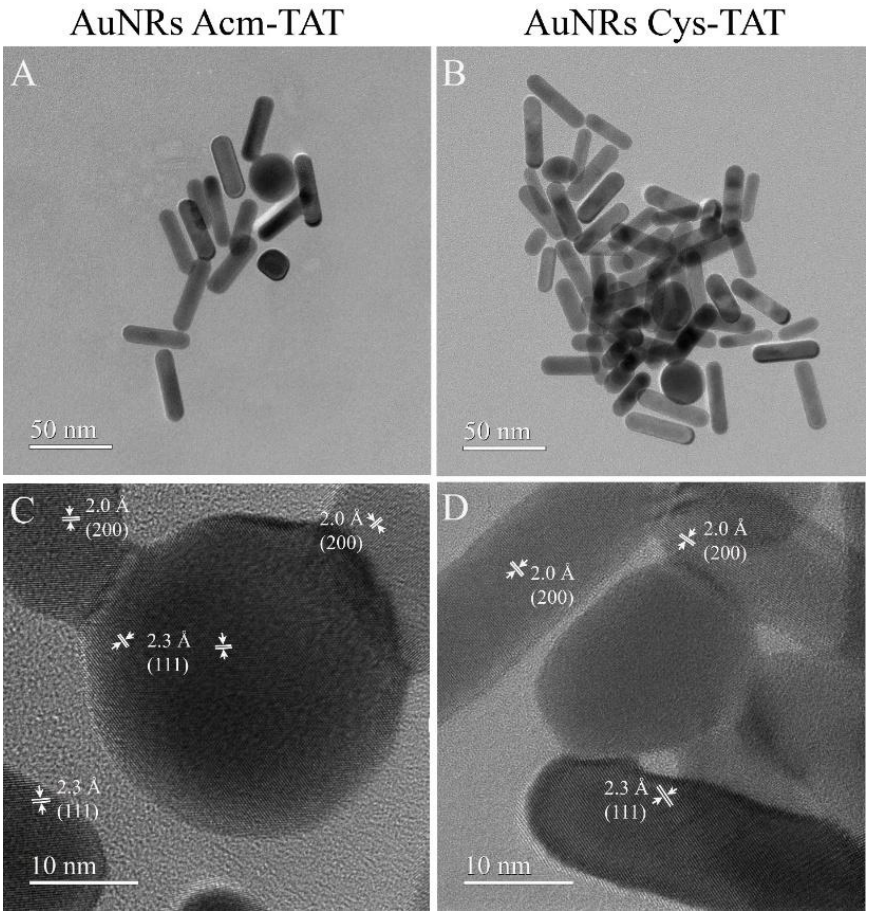

Figure 24. CTEM (A, B) and HRTEM (C, D) images of AuNRs functionalized with Acm-TAT and Cys-TAT.

Conventional TEM (CTEM) images (Fig. 24A, B) revealed nanorods together with a minor fraction of spherical nanoparticles. For both samples, nanorods exhibited lengths ranging from 18 to 52 nm and widths between 9 and 12 nm. Spherical nanoparticles showed diameters ranging from 9 to 28 nm. High-resolution TEM (HRTEM) images (Fig. 24C, D) confirmed the crystalline structure of the nanomaterials. Lattice fringes with interplanar spacings of 2.3 Å and

2.0 Å were observed, corresponding to the (111) and (200) crystallographic planes of face-centered cubic (fcc) gold, respectively.

3.1.1 DLS CHARACTERIZATION

DLS measurements performed on AuNRs in Milli-Q water showed a hydrodynamic diameter of 8.43 nm ± 0.1 nm and a polydispersity index (PDI) of 0.647. The difference between DLS and FESEM data on AuNRs size and the high value of PDI are due to the different physical property measured by these techniques (hydrodynamic diameter versus projected diameter) and to the morphology of the AuNRs, far from the spherical shape on which DLS is based to determine these characteristics. Electron microscopy allows to determine the primary size of particles whereas DLS measures the time-dependent fluctuations in scattering intensity due to constructive and destructive interference resulting from the relative Brownian movements of the AuNRs. Through the autocorrelation function and subsequent calculation of the exponential decay it determines the hydrodynamic diameter that represents the diameter of an equivalent rigid sphere that diffuses at the same rate as the analyte [94]. The time-dependent position or velocity of the suspended particles affects frequency shifts resulting from light scattered by the suspended particles, leading to misleading results for hydrodynamic diameter polydispersity and aggregation state for non-spherical NPs. AuNRs show positive surface charge and high stability over one month for AuNRs in Milli-Q water as indicated by the values of Zeta potential greater than 30 mV (Fig. 25).

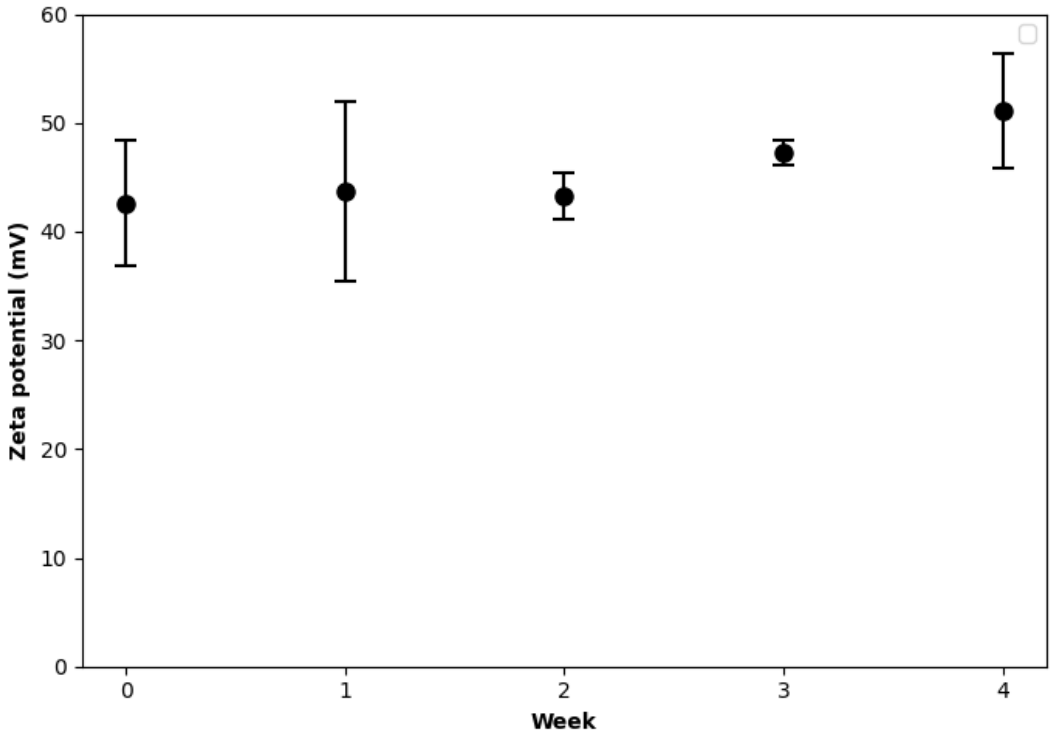

Figure 25. Time trend of AuNRs Zeta potential. Data points represent the mean of at least three independent measurements. The error bars represent the standard deviation (SD). All measurements were performed in a Milli-Q aqueous solution at 25°C and neutral pH.

3.2. SYNCHROTRON RADIATION-INDUCED SPECTROSCOPIC ANALYSIS

3.2.1. SYNCHROTRON RADIATION INDUCED X-RAY PHOTOELECTRON SPECTROSCOPY (SR-XPS)

The surface chemical composition of the pristine gold nanorods (AuNRs) has already been investigated by X-ray Photoelectron Spectroscopy (XPS) in a work from our research group [95]. That study provides a detailed analysis of the Au4f, Br3d, and Ag3d core level regions, confirming the successful synthesis of CTAB-stabilized AuNRs and the presence of residual silver and bromide ions associated with the growth and stabilization process. Therefore, in the present work, only XPS data relevant to the additional peptide or radiopharmaceutical functionalization are discussed, while reference is made to the aforementioned publication for the complete XPS characterization of the unmodified nanorods.

3.2.1.1. ^{99}Tc-sestaMIBI and AuNRs conjugation

In order to verify the successful conjugation of the radiopharmaceutical to gold nanorods (AuNRs) and to assess any potential alteration of the molecular structure of technetium-99 (^{99}Tc) following functionalization, synchrotron radiation X-ray photoelectron spectroscopy (SR-XPS) measurements were performed on the AuNR-^{99}Tc sample. For comparison purposes, SR-XPS analyses were also carried out on the pristine ^{99}Tc sample. The SR-XPS investigations focused on the C1s, N1s, and Tc3d core levels. For the ^{99}Tc-sestaMIBI-AuNRs sample, the Au4f core level was also examined. Complete results from the SR-XPS data analysis—including binding energy (BE), full width at half maximum (FWHM), atomic percentages, and proposed assignments for each spectral component. All spectral signals exhibited composite features. Through an appropriate peak-fitting procedure, several components were identified and assigned based on comparison with literature data [96].

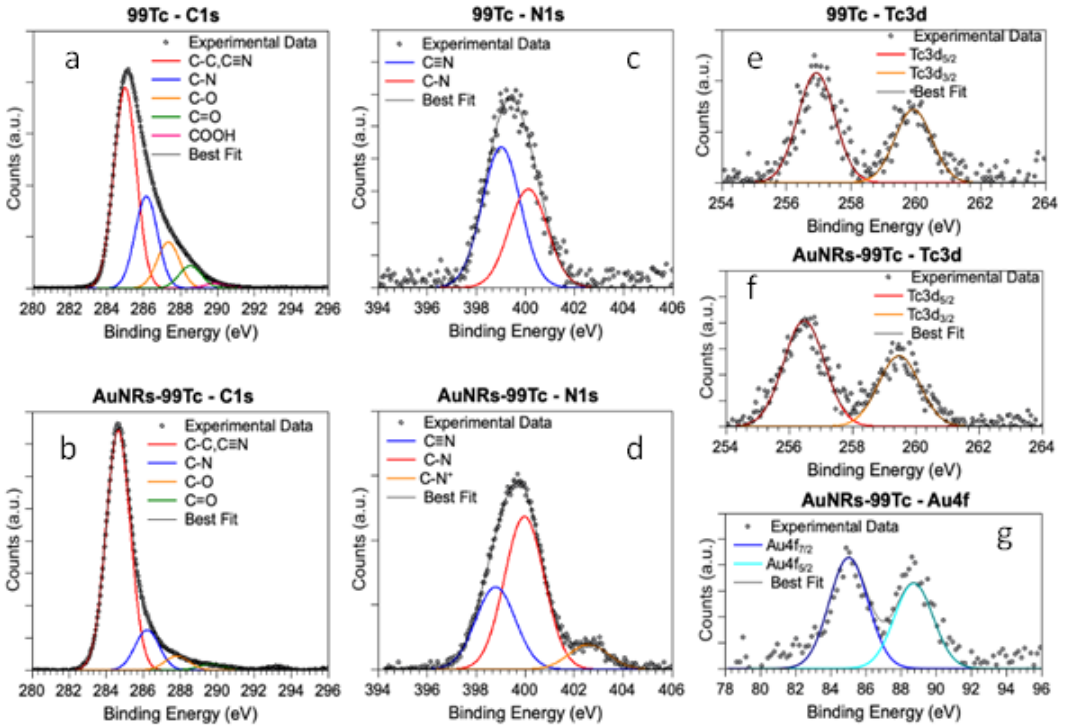

Figure 26. SR-XPS spectra. C1s (a,b), N1s (c,d), Tc3d (e,f) of the decayed and non-radioactive radiophar-maceutical ^{99}Tc and its conjugate on the gold rods AuNR-99Tc. SR-XPS Au4f spectrum of the AuNR-^{99}Tc (g) [83].

As shown in Figure 26, the C1s and N1s core level spectra confirm the preservation of the ^{99}Tc molecular structure after conjugation with AuNRs. Furthermore, for the AuNR-^{99}Tc system, the presence of CTAB is clearly detected, consistent with the expected chemical composition of the nanorods. In particular, the increased intensity of the C1s component at 285.0 eV (assigned to C–C bonds) in the AuNR-^{99}Tc sample, compared to pristine ^{99}Tc, is attributed to the aliphatic chain of CTAB (Fig. 26 a,b). A similar trend is observed in the N1s region, where the signal associated with amine-like nitrogen becomes more intense relative to the component assigned to C≡N groups (Fig. 26 c,d). Conversely, the intensity of the C1s peak at 287.3 eV, attributed to C–O groups of the –OMe moieties present in ^{99}Tc, decreases in the AuNR-^{99}Tc sample, as expected. The higher-BE C1s peaks assigned to C=O (~288 eV) and –COOH (~290 eV) groups suggest the presence of impurities, which are commonly observed in samples prepared in air and deposited from aqueous solution. To further confirm the effectiveness of ^{99m}Tc-sestaMIBI conjugation to the AuNRs surface, the Au4f and Tc3d signals were analysed. In the Au4f spectrum (Fig. 26 g), a single spin-orbit doublet is observed, with the main Au4f$_{7/2}$ component centered at 85.04 eV, consistent with gold atoms at the AuNRs surface interacting with ligands [97]. Finally, the high reproducibility of the Tc3d spectral position and shape [98, 99] further supports the successful and stable loading of the radiopharmaceutical onto the nanorods (Fig. 26 e,f).

3.2.1.2. TAT PEPTIDE AND AUNRS CONJUGATION

XPS data analysis was carried out on solid-state samples of both pristine cys-TAT and the AuNR-Cys-TAT conjugate, prepared as thin films via deposition from aqueous solutions onto TiO_2/Si(111) substrates. These analyses enabled the confirmation of successful peptide anchoring to the AuNRs surface in both cases, as well as the preservation of the peptide's molecular structure following interaction with the nanoparticles. All acquired spectra and the spectral components identified through peak-fitting procedures are shown in Figure 27 and are discussed in detail below. The C1s spectra collected for both cys-TAT and AuNR-cys-TAT (Figure 1a,d) exhibit the same major components: C–C and C–S bonds at 285.00 eV BE, C–N at 286.3 eV, C–O at approximately 287 eV, amide-like NH–CO groups near 288 eV, and COOH functionalities in the 289–290 eV range. Notably, the atomic percentage of the C–C component is higher in the functionalized nanorods, consistent with the presence of CTAB. The N1s spectra (Fig. 27 b,e) display two main components for the pristine peptide: one at 398.5 eV

corresponding to amide nitrogen, and another at 400.2 eV associated with amine-like nitrogen. Additionally, a minor feature at 402 eV is observed, attributed to positively charged amine groups—commonly detected in amino acids. In the AuNR-cys-TAT conjugate, the peak fitting reveals broader features due to increased surface roughness, resulting in overlapping signals that appear as a single component centered at approximately 398.7 eV BE. A pronounced peak at ~400 eV BE is also present, indicative of the NR_4^+ tertiary amines of CTAB [95]. The S2p spectra (Fig. 27 c,i) are highly comparable between the pristine cys-TAT and the AuNR- cys-TAT conjugate, supporting the excellent chemical stability of the peptide upon conjugation with the AuNRs. Detailed analysis of the S2p components provides insights into the chemical interactions between the peptide and the AuNRs. A spin-orbit doublet at low BE values is associated with thiol sulphur atoms covalently bonded to metal surfaces. In the case of pristine cys-TAT, this component is low in intensity (~8% atomic percentage) and is attributed to interactions between the peptide and the TiO_2 substrate ($S2p_{3/2}$ BE = 161.8 eV). In contrast, for the AuNR- cys-TAT sample, this component shifts to a lower BE (161.2 eV) and displays a significantly higher intensity (~24.5% atomic percentage when measured at 260 eV photon energy), as expected for thiol groups covalently bound to the gold surface [100]. Notably, at a photon energy of 600 eV—corresponding to a greater probing depth—the RS–Au signal increases further, reaching ~32% atomic percentage, providing additional evidence for covalent bond formation at the AuNRs/peptide interface. At higher binding energies, both cys-TAT and AuNR-cys-TAT exhibit a main component at ~163.5 eV BE, attributable to unreacted thiol groups and/or disulfides (RSH, RS–SR), which are common due to the high reactivity of thiols. Furthermore, oxidized sulphur species are observed in both samples, consistent with air and water exposure during deposition and conjugation procedures. This component appears at BE $S2p_{3/2}$ = 168.3 eV, with atomic percentages of 33% for pristine cys-TAT and 23% for the AuNR-conjugated sample. The Au4f, Br3d, and Ag3d core-level spectra for the AuNR- cys-TAT sample (Fig. 27 g,h,f) display all expected features for AuNRs stabilized with CTAB and additional surfactants, in agreement with previously published data [101]. In conclusion, SR-XPS analysis demonstrated that the cys-TAT peptide retains its molecular integrity upon binding to the AuNRs, and it clearly supports the formation of covalent bonds between the thiol functionalities of the peptide and gold atoms on the AuNRs surface. At the same time, the structural integrity of the AuNRs themselves is confirmed by the high reproducibility of the Au4f, Br3d, and Ag3d spectra, in line with reference data collected from CTAB-stabilized nanorods.

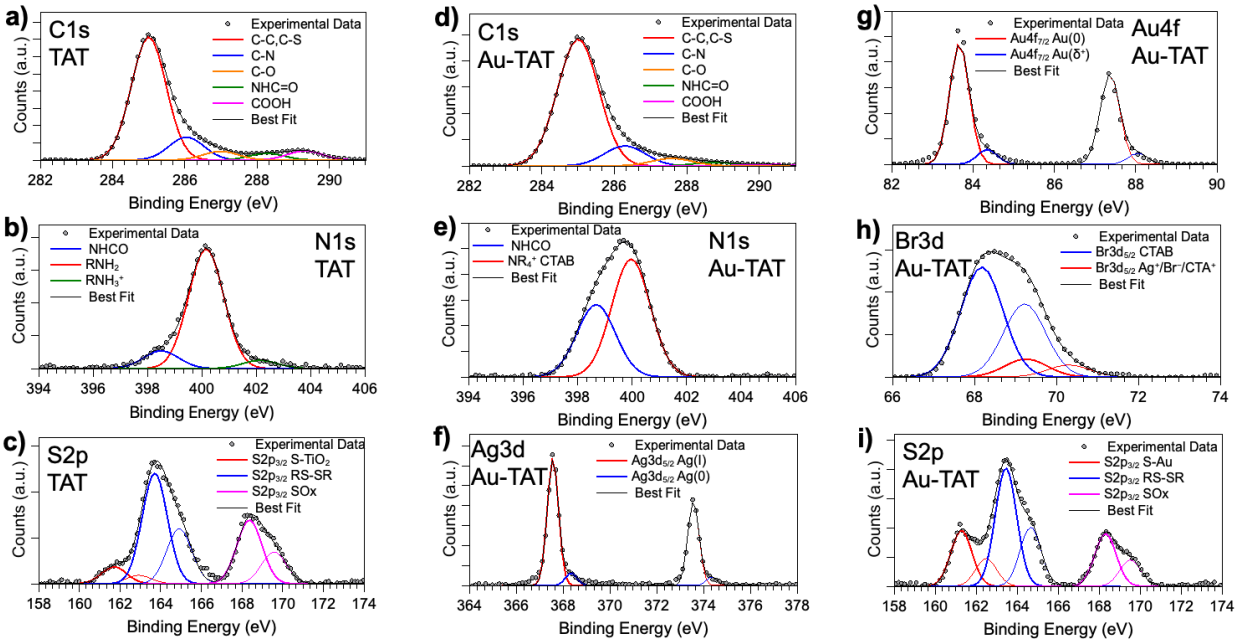

Figure 27. SR-XPS spectra collected on sample cys-TAT at a) C1s, b) N1s, c)) S2p core levels, and on sample AuNR-cys-TAT (namely Au-TAT in figure) at d) C1s, e) N1s, f) Ag3d, g) Au4f, h) Br3d and i) S2p core levels.

3.2.2. NEAR EDGE X-RAY ABSORPTION FINE STRUCTURE (NEXAFS)

3.2.2.1. TAT PEPTIDE AND AUNRS CONJUGATION

Near-edge X-ray absorption fine structure (NEXAFS) spectra recorded at the C K, N K, and O K edges for both the pristine cys-TAT peptide and the functionalized AuNR-cys-TAT nanorods are shown in Figure 28. In the C K-edge spectrum of the cys-TAT peptide (Fig. 28 a, black line), two C 1s → π* resonances are observed below the absorption edge, located at 285.4 eV and 288.7 eV, respectively.

The π* resonance at 288.7 eV is characteristic of C=O bonds and is typically associated with the amide functionalities of the peptide backbone, consistent with previous studies on similar peptide systems [102, 103]. The resonance at 285.4 eV is attributed to transitions into antibonding C=C orbitals. At photon energies above the absorption edge, broad σ* resonances are detected, arising from C–C and C=O molecular orbitals.

The N K-edge spectrum of cys-TAT (Fig. 28 b, black line) also reveals two prominent N 1s → π* resonances. The first, located at 402 eV, is attributed to transitions associated with peptide

bonds. The second resonance, at 399.5 eV, originates from transitions involving the C=N bonds of the guanidinium group, which is a distinctive feature of the arginine residues that constitute the primary sequence of the cys-TAT peptide [104]. In the post-edge region, two broader N 1s → σ* resonances are observed, corresponding to excitations involving N–H and C–N bonds.

The O K-edge spectrum of cys-TAT (Fig. 28 c, black line) displays a single sharp O 1s → π* resonance, again associated with the C=O bonds of the peptide backbone. A broad O 1s → σ* resonance appears at higher photon energies, corresponding to transitions into molecular orbitals involving oxygen atoms.

The NEXAFS spectra acquired at the C, N, and O K edges for the AuNR-cys-TAT conjugate (Fig. 28 a–c, red lines) show peak features that are fully consistent with those of the pristine peptide. All π* resonances occur at the same energies as those observed for the unbound cys-TAT, indicating that the electronic structure of the peptide remains unaltered following chemisorption onto the gold nanorod surface. Although the overall signal intensity is reduced—due to the low amount of peptide material present as a chemisorbed overlayer—the characteristic π* resonances remain clearly discernible. The reduced signal-to-noise ratio, particularly evident in the N K-edge spectrum, results in noisier data, yet the spectral features remain intact. These findings strongly support the conclusion that the molecular structure of the cys-TAT peptide is preserved upon immobilization onto AuNRs.

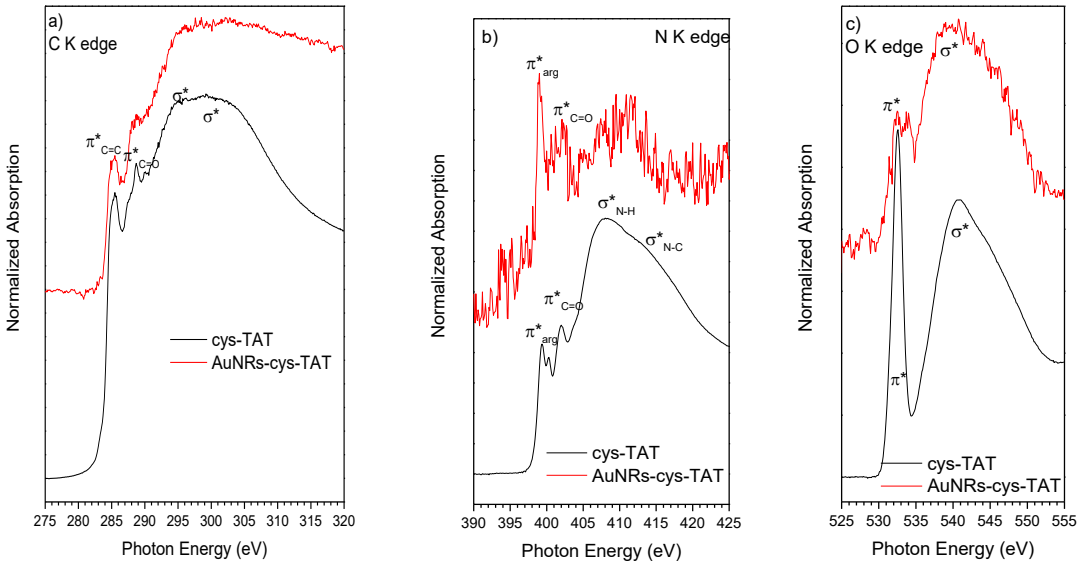

Figure 28. C K edge (a), N K edge (b) and O K edge (c) NEXAFS spectra of pristine cys-TAT (black line) and AuNR-cys-TAT (red line).

3.2.3. REFLECTION-ABSORPTION INFRARED SPECTROSCOPY (RAIRS)

3.2.3.1. ^{99}TC-SESTAMIBI AND AUNRS CONJUGATION

Figure 29 is displays the FTIR spectra for the pristine ^{99}Tc-sestaMIBI drug and for the AuNR-^{99}Tc nanoconjugate in the 2000-800 cm^{-1} region where the diagnostic peaks are located.

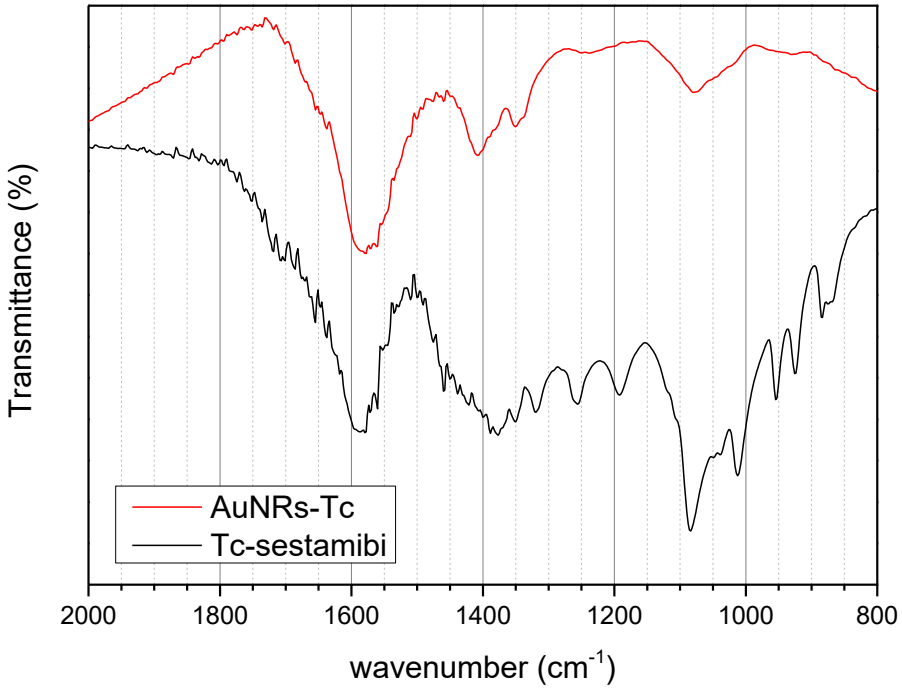

Figure 29. FTIR spectra of ^{99}Tc-sestaMIBI (black line) and AuNR-^{99}Tc (red line) in the 2000-800 cm^{-1} region.

The most intense peak in the spectrum of ^{99}Tc-sestaMIBI is the stretching of the C-O bond related to the methoxy groups located at 1080 cm^{-1}; this peak is also present in the spectrum of AuNR-^{99}Tc confirming the successful immobilization of the drug on the AuNRs surface.

The peak at 1586 cm^{-1} observed in the spectra of both ^{99}Tc-sestaMIBI and AuNRs–^{99}Tc is attributed to the asymmetric stretching of the carboxylate group of the citrate anion. The broad peak around 1390 cm^{-1} corresponds to the symmetric stretching of the same functional group [105].

3.2.3.2. TAT PEPTIDE AND AUNRS CONJUGATION

Figure 30 displays the most informative regions of the FTIR spectra for the pristine cys-TAT peptide and the AuNR-cys-TAT nanoconjugate, specifically the 4000–2400 cm^{-1} and 1900–1000 cm^{-1} regions.

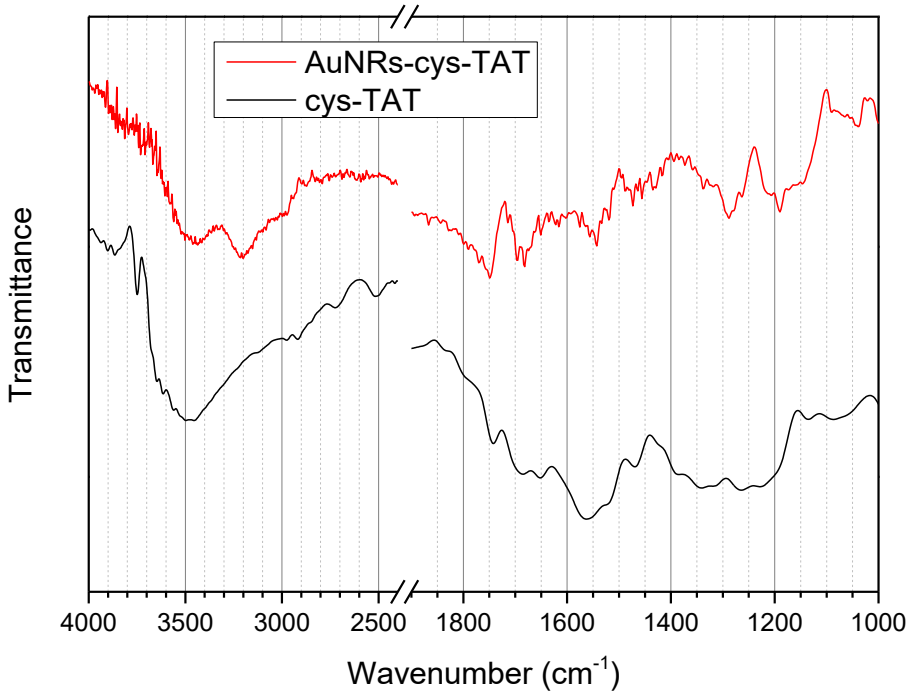

Figure 30. FTIR spectra of cys-TAT (black line) and AuNR-cys-TAT (red line) in the 4000-2400 and 1900-1000 cm^{-1} regions.

In the 4000–2400 cm^{-1} region of the spectrum, the cys-TAT peptide exhibits a broad and intense band centred at approximately 3500 cm^{-1}, resulting from the superposition of O–H and N–H stretching vibrations. Additionally, low-intensity bands in the 2980–2910 cm^{-1} range are attributable to aliphatic C–H stretching modes. A distinct absorption band at 2515 cm^{-1} is ascribed to the S–H stretching vibration of the cysteine thiol group.

The 1700–1400 cm^{-1} region reveals a complex profile arising from the overlap of several vibrational modes. As commonly observed in peptide IR spectra, three characteristic amide bands are present: the amide I band (predominantly C=O stretching) typically appears between 1700 and 1600 cm^{-1}; the amide II band (N–H bending) between 1600 and 1500 cm^{-1}; and the amide III band (a combination of C–N stretching and N–H deformation) between 1350 and

1250 cm^{-1}. The precise shape and position of the amide I band are often indicative of the peptide's secondary structure [106]. Furthermore, the abundance of arginine residues in the cys-TAT sequence leads to a strong C=N stretching vibration from the guanidinium group around 1666–1662 cm^{-1}, and a prominent N–H bending mode in the 1554–1537 cm^{-1} region. Notably, this latter signal can be influenced by the protonation state of nitrogen atoms and the involvement in hydrogen bonding interactions [107, 108].

In the FTIR spectrum of the AuNR-cys-TAT conjugate (red line), the disappearance of the 2515 cm^{-1} band confirms the involvement of the thiol group in covalent binding to the gold nanorods, consistent with a Au–S interaction. The amide I, II, and III bands remain clearly visible, centred around 1670, 1540, and 1280 cm^{-1}, respectively, confirming that the peptide backbone retains its integrity and that successful functionalization of the nanorods has occurred.

Additionally, in the high-frequency region, a new feature emerges around 3200 cm^{-1}, and the weak band near 1750 cm^{-1} observed in the spectrum of cys-TAT becomes more pronounced in the AuNR-cys-TAT spectrum. These two spectral changes can plausibly be attributed to residual ascorbic acid (AA) adsorbed on the nanorod surface, as previously reported [106].

3.3. BIOLOGICAL RESULTS

3.3.1. COLONY-FORMING ASSAY

For the study of the AuNRs, different concentrations between 0.025 µg/mL and 1 µg/mL (Fig. 31) were tested in T98G cells and compared to the control (no treated cells).

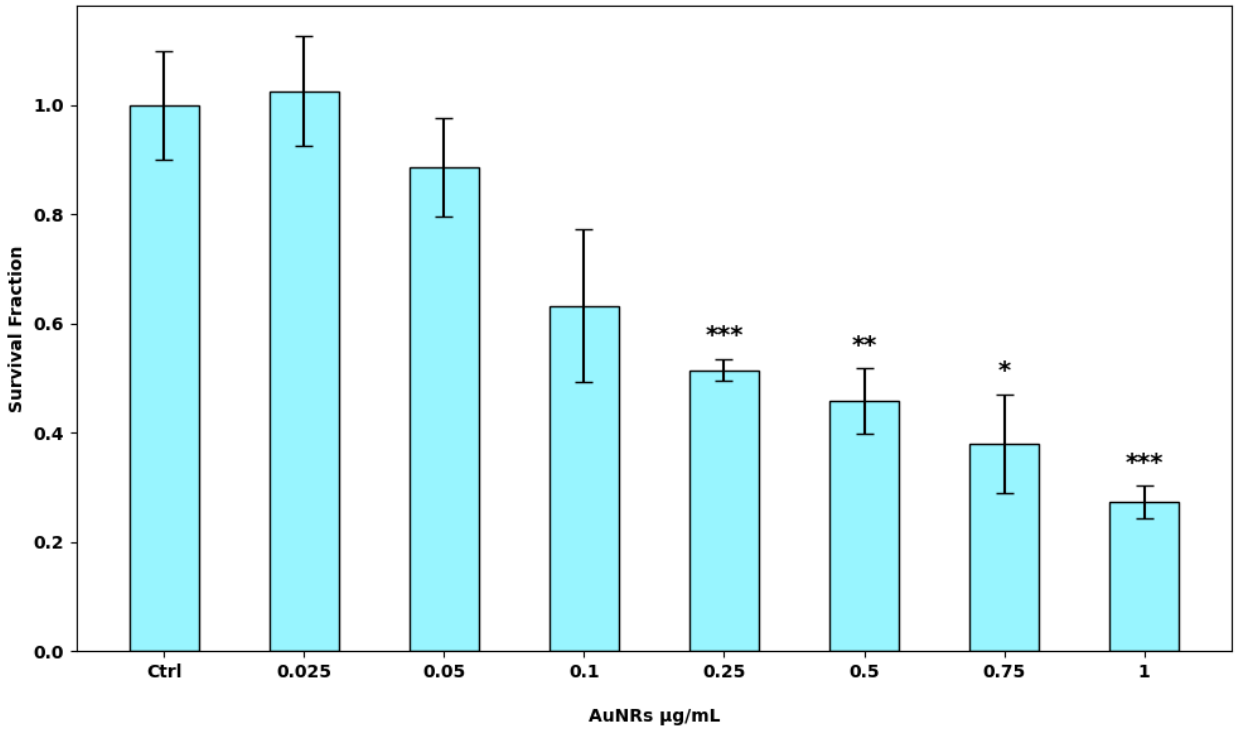

Figure 31. Bar plot showing the survival fraction (SF) obtained from colony-forming assay. All samples are normalized to the control (Ctrl). P value *= $p<0.05$, ** = $p<0.01$, *** = $p<0.001$. Significance was calculated related to Ctrl using two-tailed Student's t-test. Error bars represent the standard error of the mean (SEM) obtained from at least 3 independent experiments.

The lower concentrations (0.025 and 0.05 µg/ml) did not show a significant difference compared to the control, but from 0.25 µg/ml, it can be observed a significant reduction in survival, with a dose-dependent effect. For the following experiment, the concentrations of 0.1 and 0.5 µg/mL were chosen because an effect was observed but it was not so relevant.

For evaluating the toxicity of AuNRs, alone and in combination with gamma rays (γ-rays) irradiation, the colony-forming assay was performed with T98G cells. The samples analysed were:

Only cells (Ctrl);

- Irradiated cells with 2 different γ-rays doses (1 Gy and 4 Gy);
- Cells treated with 2 different concentrations of AuNRs (0.1 µg/mL and 0.5 µg/ml);
- Cells receiving the combined treatment (1 Gy + 0.1 µg/mL; 1 Gy + 0.5 µg/mL; 4 Gy + 0.1 µg/mL and 4 Gy + 0.5 µg/mL).

The concentrations of AuNRs were chosen based on the previous experiment (Fig. 31), while the radiation doses were chosen according to of literature [109]. To analyse the data, the mean of the PE of each sample was normalized to the control (*i.e.* untreated cell - Ctrl). The results, shown in Figure 32, demonstrate that the survival fraction (SF) decreases as the radiation dose and AuNRs concentration increase. The data for the AuNR-only samples are consistent with previous observations, and also the radiation-results agree with the literature [110, 111, 112, 113].

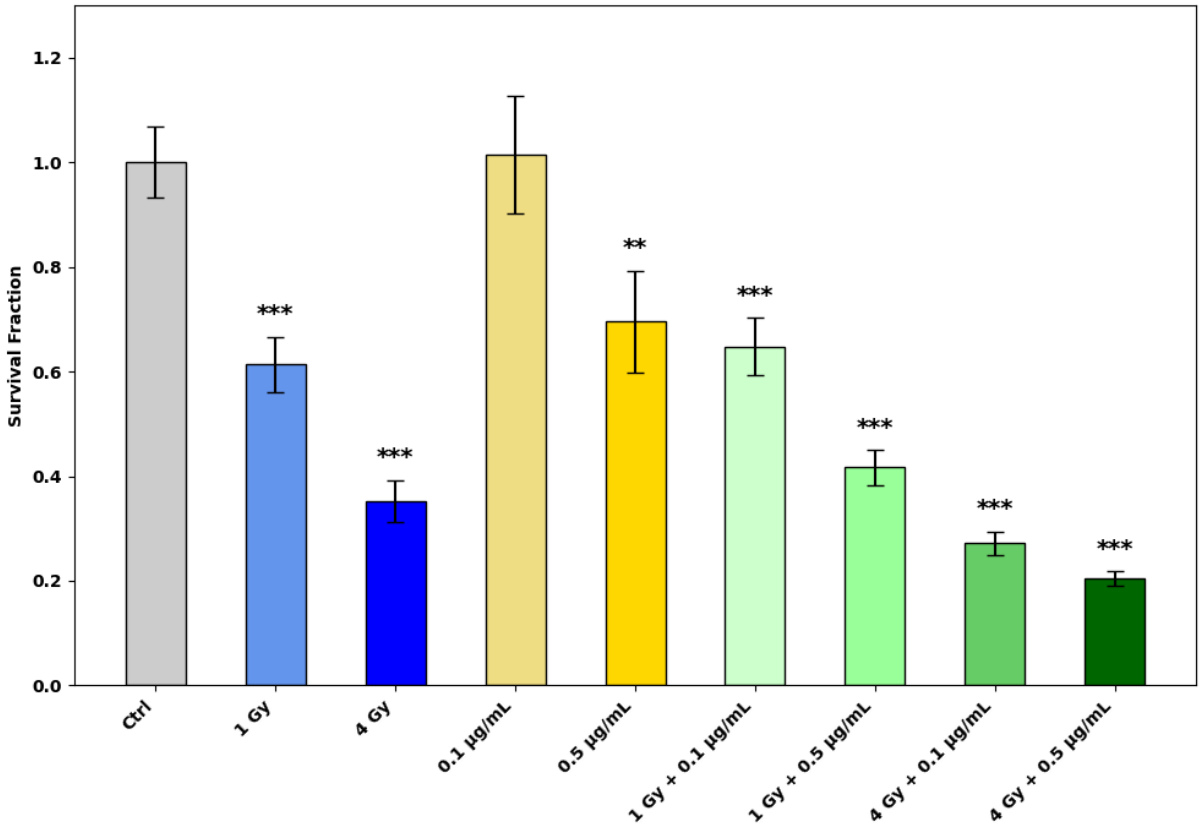

Figure 32. Bar plot showing SF obtained from colony-forming assay. All data, except for 0.1 µg/mL, are significantly different to the control (Ctrl). P value *= $p<0.05$, ** = $p<0.01$, *** = $p<0.001$.

Significance was calculated related to Ctrl using the two-way ANOVA test. Error bars represent the SEM obtained from at least 3 independent experiments.

In samples with combined treatment (i.e. AuNRs + γ-rays irradiation), the SF decreases at the as the concentration of AuNRs increases, with an overall trend that would appear to be linear. To investigate the effect of the AuNRs loaded with the ^{99}Tc-sestaMIBI, a single experiment was performed (Fig. 33). The data were normalized to the control, as in the previous experiment. The results confirm the effect of the AuNRs persists in the presence of the ^{99}Tc-sestaMIBI.

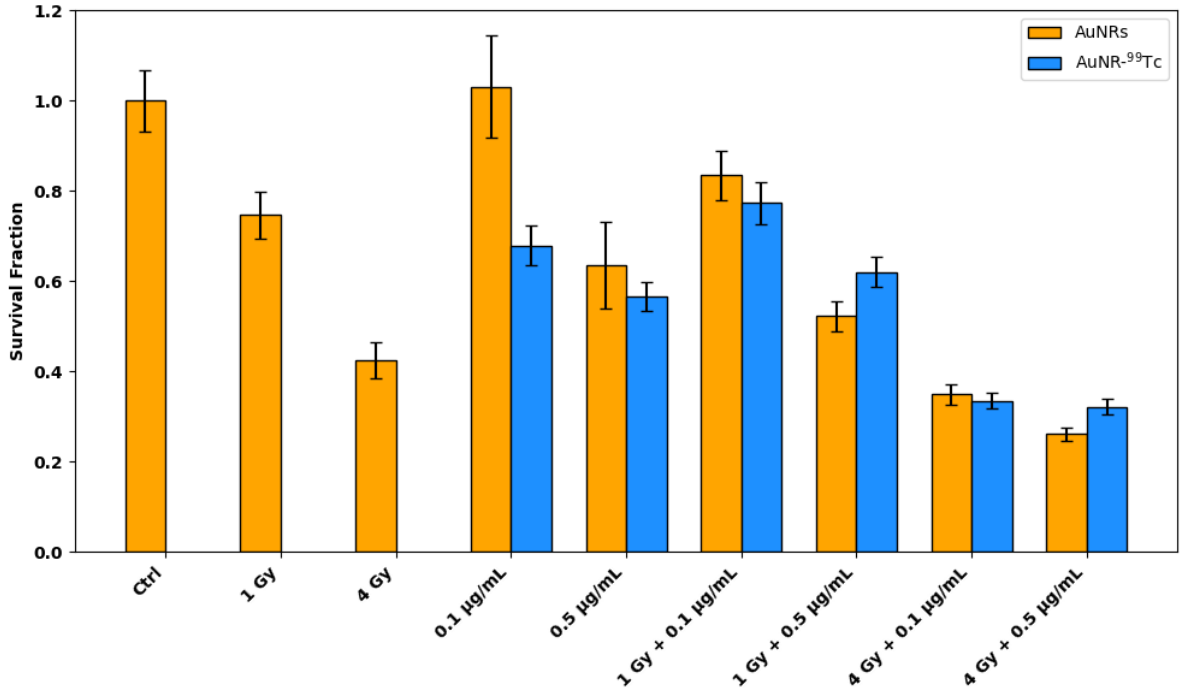

Figure 33. Bar plot for the results of the SF obtained from colony-forming assay performed with AuNRs only (orange bars) and AuNR-^{99}Tc (blue bars). The error bars represent the SEM.

3.2.1. REALTIME-GLO ™ MT CELL VIABILITY ASSAY VALIDATION PROTOCOL

The first experiment was conducted with "naked" AuNRs, without any functionalization, to test their effect on cells. The concentrations tested were different from the previous studies because, in this case, cell death was evaluated in a shorter time, so potentially more toxic concentrations were required. The concentration of 50 µg/mL show a 100% of death (Fig. 34), meanwhile the concentrations of 5 and 10 µg/mL cause a significant reduction in cell

viability, but not as pronounced. For 0.1 and 0.5 µg/mL, the results were comparable to those obtained in the survival fraction assay (see Figure 32)

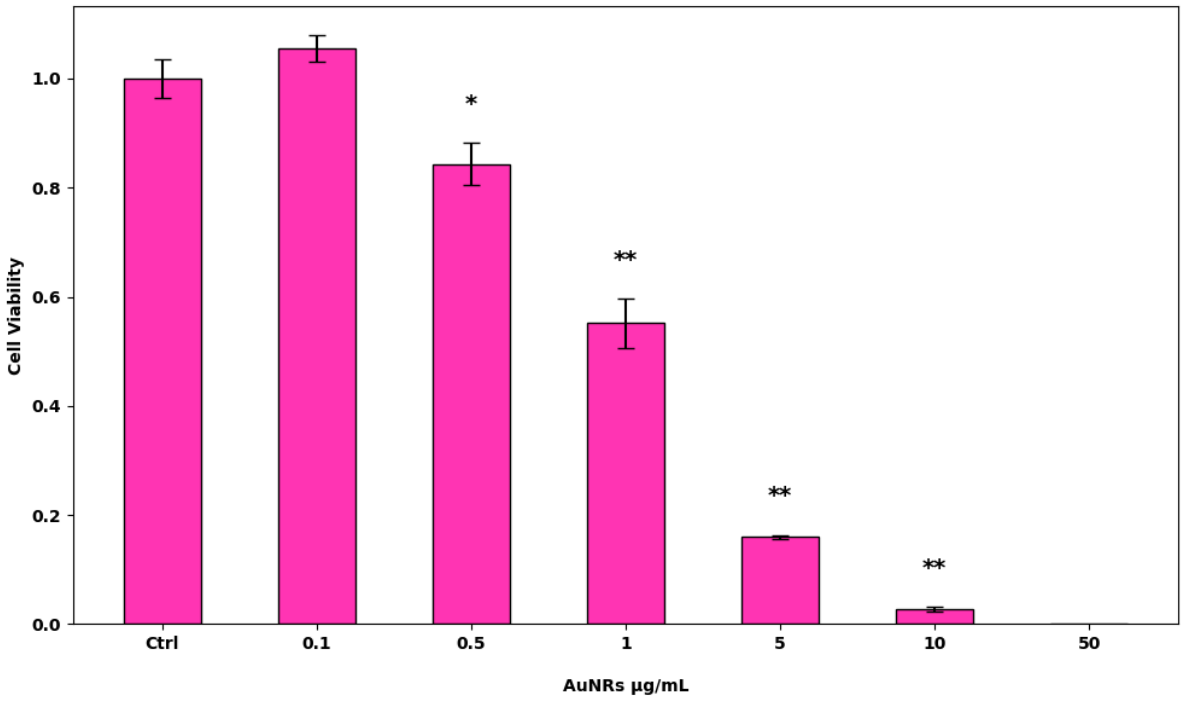

Figure 34. Bar plot of cell viability tasted by RealTime Glo MT assay. All data, except for 0.1 µg/mL, are significantly different from the control (Ctrl). P value *= $p<0.05$, ** = $p<0.01$, *** = $p<0.001$. Significance was calculated related to Ctrl two-tailed unpaired Student's t-test for unequal variances was performed. The error bars represent the propagation of the error.

A second experiment was conducted with the AuNRs functionalized with TAT (Fig. 35). The concentrations and the protocol were the same as the previous experiment. The results obtained showed a different toxicity profile for AuNR-TAT. The hypothesis is that TAT replace the CTAB present on the AuNR's surface rendering the system less toxic.

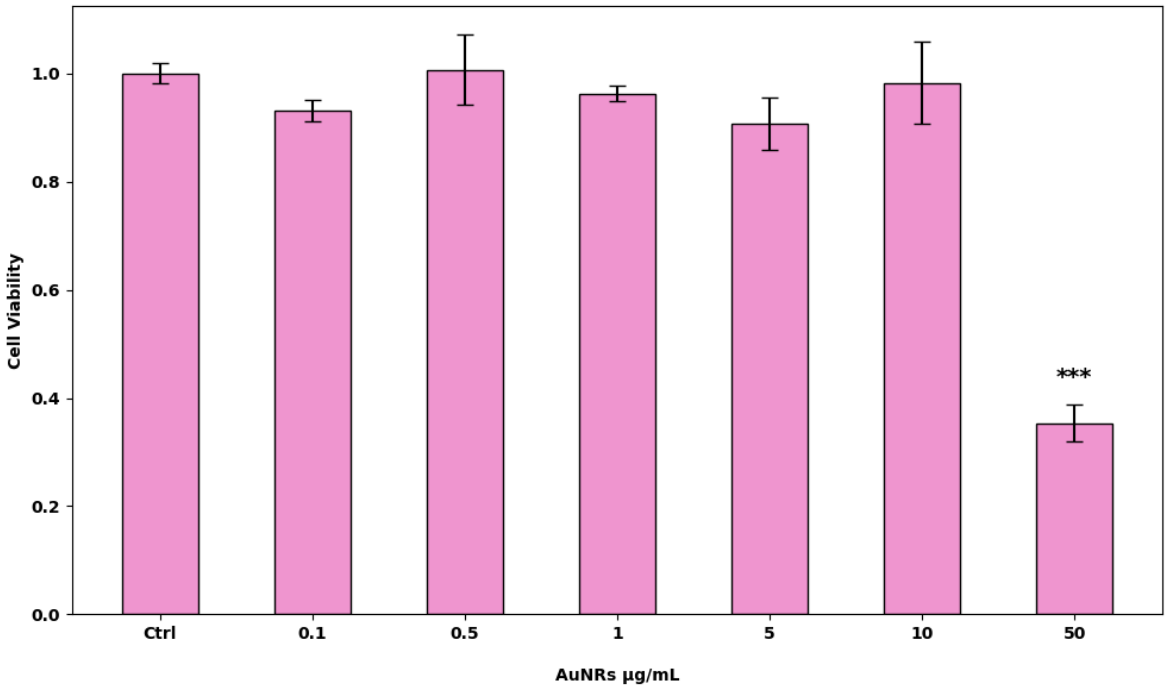

Figure 35. Bar plot of cell viability tasted by RealTime Glo MT assay with AuNR-TAT. Only the concentration 50 µg/mL is significantly different form the Ctrl. P value *= $p<0.05$, ** = $p<0.01$, *** = $p<0.001$. Significance was calculated related to Ctrl two-tailed unpaired Student's t-test was performed. The error bars represent the propagation of the error.

Future experiments are needed to understand the mechanism and to investigate the concentrations between 10 and 50 µg/mL to determine why functionalized AuNRs start to become a much more toxic.

3.2.2. γ-H2AX ASSAY VALIDATION PROTOCOL

The radio-sensitizing efficacy of the AuNR-TAT was assessed by quantifying the induction and repair of DNA double-strand breaks (DSBs), the most critical damage induced by ionizing radiation. We utilized the analysis of the phosphorylated histone H2AX (γ-H2AX), which rapidly accumulates at DSB sites, forming distinct structures known as foci. Each γ-H2AX focus corresponds to one or more unrepaired DSBs; therefore, its quantification at specific time points provides a direct measure of the extent of residual damage and the temporal evolution of repair kinetics. The analysis was performed using confocal microscopy on fixed samples. The visualization of these fluorescent foci within the nucleus is illustrated, as shown in Figure 36. This quantitative and kinetic approach allowed us to determine whether the

presence of the AuNR-TAT significantly altered the initial amount of induced damage and/or the efficiency with which that damage is resolved.

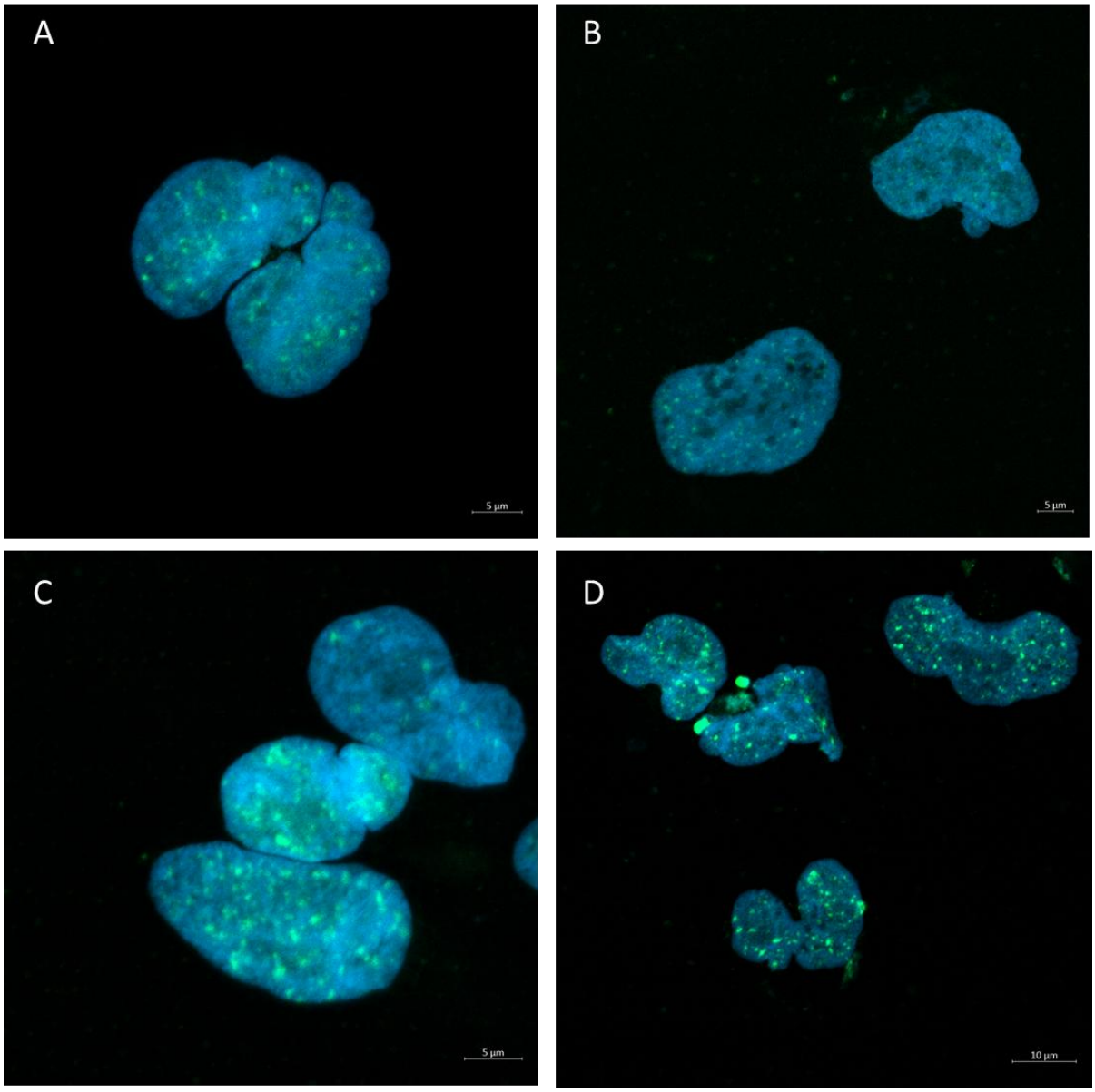

Figure 35. Immunofluorescent visualization of γ-H2AX foci (green) in cell nuclei (stained blue with DAPI). Samples were fixed at 1 hour after treatment. (A) Untreated Control (Ctrl) cells showing low, basal levels of γ-H2AX foci. (B) Cells treated with AuNR-TAT only (50 µg/mL) exhibiting foci levels comparable to the control, confirming low inherent genotoxicity. (C) Cells exposed to Radiation Only (0.5 Gy), showing a clear increase in γ-H2AX foci following DSB induction. (D) Cells from the Combined Treatment (0.5 Gy + AuNR-TAT) group, displaying a markedly higher and denser population of γ-H2AX foci compared to all other conditions, providing visual evidence of the strong radio-sensitizing effect of the AuNR-TAT. Scale bars are indicated in the bottom right of each panel.

The induction and repair of DNA DSBs were evaluated using immunocytochemical analysis of γ-H2AX foci, quantified at different time points (30 min, 1 h, 2 h) following irradiation. In accordance with the established methodology, the number of γ-H2AX foci, present inside the nucleus, was counted, analysing 100 nuclei per sample. To isolate the specific signal induced by the treatment and remove the physiological or background staining, the mean number of foci quantified in the untreated controls (cells only, fixed at the same time point) was subtracted from the mean of the treated samples. The final results, show in Figure 37, are expressed as the mean number of γ-H2AX foci per nucleus (± standard deviation).

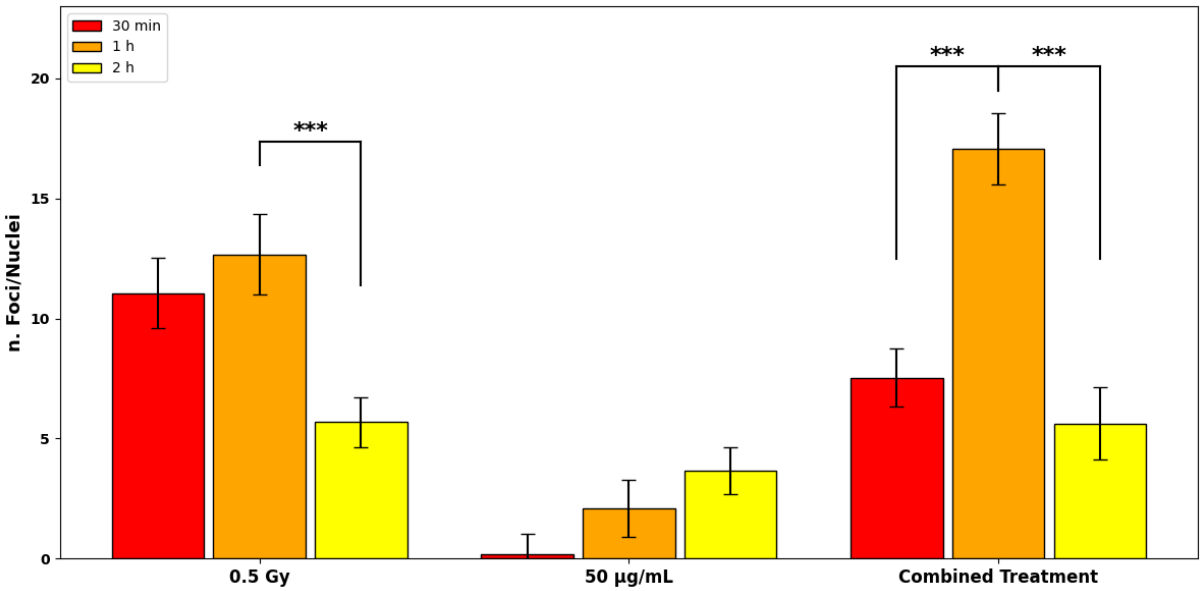

Figure 37. Bar plot showing the kinetics of DNA double-strand break (DSB) induction and repair measured through the quantification of γ-H2AX foci per nucleus (Foci/Nuclei). Cells were exposed to γ-rays irradiation (0.5 Gy), AuNR-TAT (50 µg/mL) or the Combined Treatment, and analysed at 30 minutes, 1 hour (h), and 2 hours. Foci counting was performed on 100 nuclei per sample, and the background (mean of the untreated control) was subtracted. Error bars represent the Standard Error of the Mean (SEM). Statistically significant differences were determined by one-way Anova by comparing the treated conditions, as indicated by the lines above the bars. ***= $p < 0.001$.

The radiation-only treatment (0.5 Gy) exhibited a rapid induction of DSBs. The maximum level of induced damage was recorded at 1 hour (12.5 ± 1.8 Foci/Nuclei), with high values already present at 30 minutes (11.0 ± 1.5 Foci/Nuclei). This is consistent with the known kinetics for

radiation-induced damage onset. Within 2 hours, a statistically significant reduction in foci was observed, indicating the activation of DNA repair mechanisms.

The AuNR-TAT only treatment (50 µg/mL), in the absence of irradiation, induced an extremely low number of γ-H2AX foci, which did not differ significantly from the background-corrected control. This result confirms the low inherent cytotoxicity or genotoxicity of the gold nanoparticles at the concentration used.

The combined treatment (0.5 Gy + 50 µg/mL of AuNR-TAT) resulted in a markedly altered and enhanced damage kinetic. The number of foci at 1 hour reached a value of 17.0 ± 1.3 Foci/Nuclei. This value is statistically much higher compared to the value observed with γ-rays alone. This increase suggests a radio-sensitizing effect induced by the functionalized AuNRs. Despite the amplified initial damage burden, the cell demonstrated their capacity to repair the induced damage. Between 1 hour and 2 hours, the number of foci significantly decreased to 5.5 ± 1.4 Foci/Nuclei.

An additional qualitative analysis was performed using confocal microscopy on DAPI-stained nuclei. This investigation revealed a key finding: cells treated with the AuNR-TAT, both irradiated and non-irradiated, exhibited distinct dark, rounded structures in the central sections of the nuclei as seen in Figure 38. These structures were entirely absent in nuclei of the control cells and in only irradiate once.

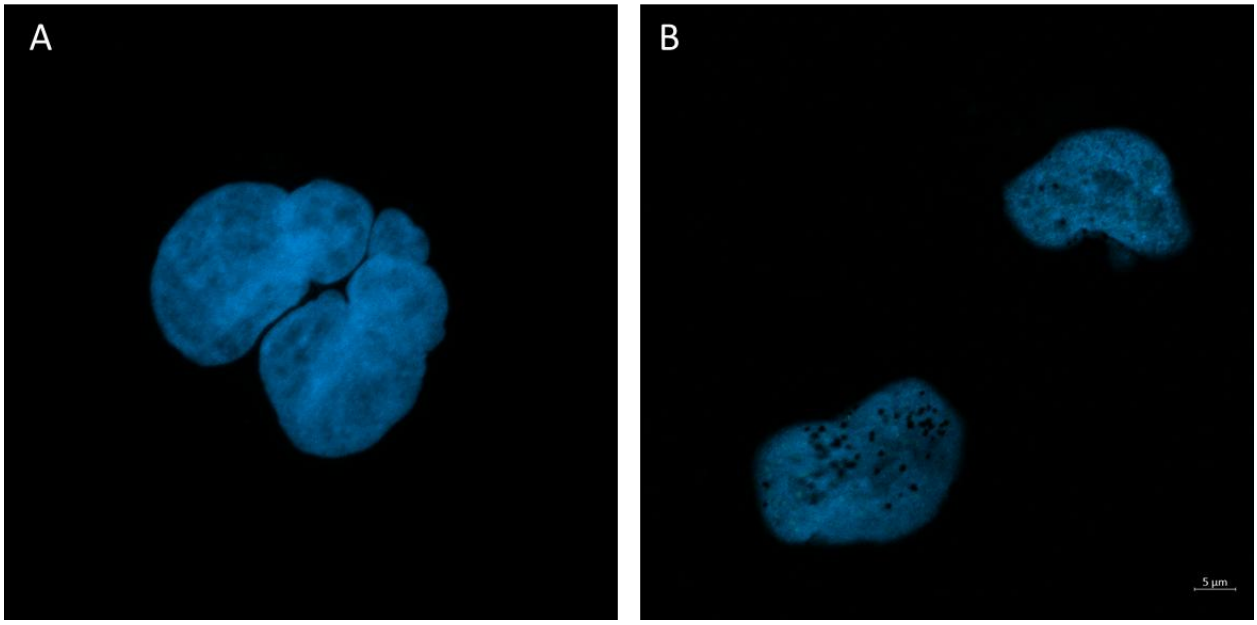

Figure 38. Immunofluorescent visualization of cell nuclei (stained with DAPI). Samples were fixed at 1 hour after treatment and the image is one section of nuclei. (A) Untreated Control (Ctrl) cells showing homogeneous blue colour of nuclei; (B) Cell treated with AuNR-TAT showing dark spots inside the DAPI coloration of nuclei.

These black spots in the nuclei of the cells analysed at first glance were obviously interpreted as clusters of AuNR-TAT in the nucleus.

To confirm this hypothesis, Transmission Electron Microscopy (TEM) was performed. Two types of experiments were conducted: in the first case (Fig. 39), the experimental conditions were identical to those of the γ-H2AX experiment in which cell cycle was blocked in G0; the second case (Fig. 40) the experimental condition used provide for cells with an active cell cycle to understand better if the uptake of AuNR-TAT is influenced by the cell cycle.

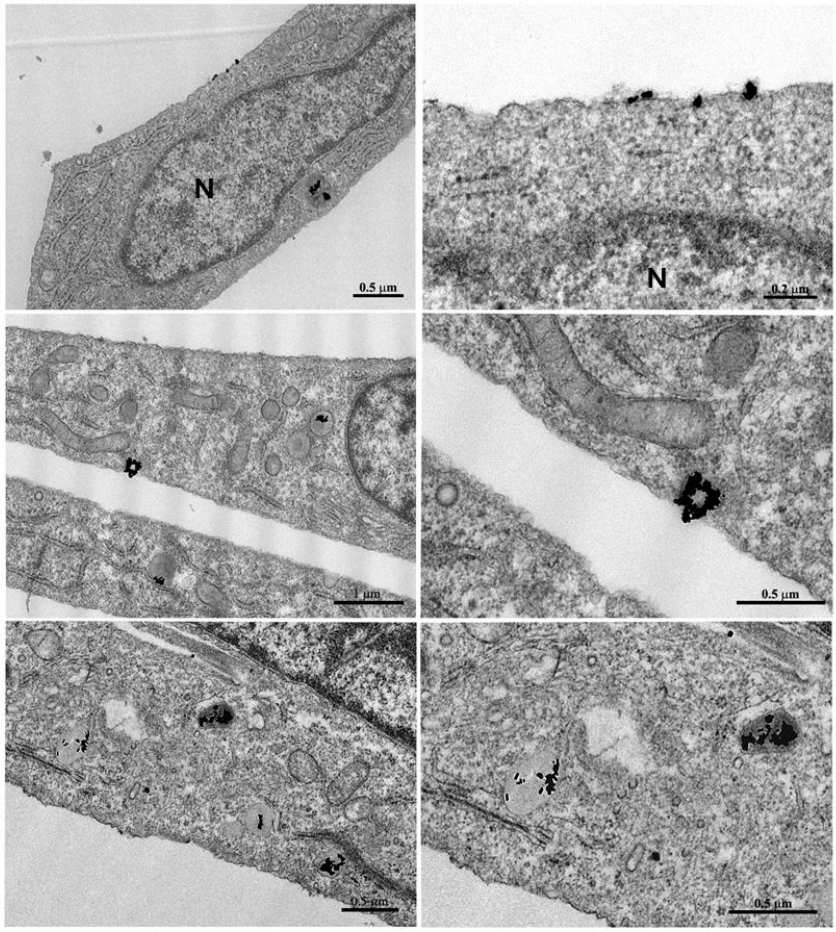

Figure 39. TEM micrographs of T98G cells treated with AuNR-TAT at various magnifications. AuNR-TAT clusters were consistently observed within intracellular vesicles and, in some cases, in close proximity to the nucleus (N). Scale bars are indicated for each magnification.

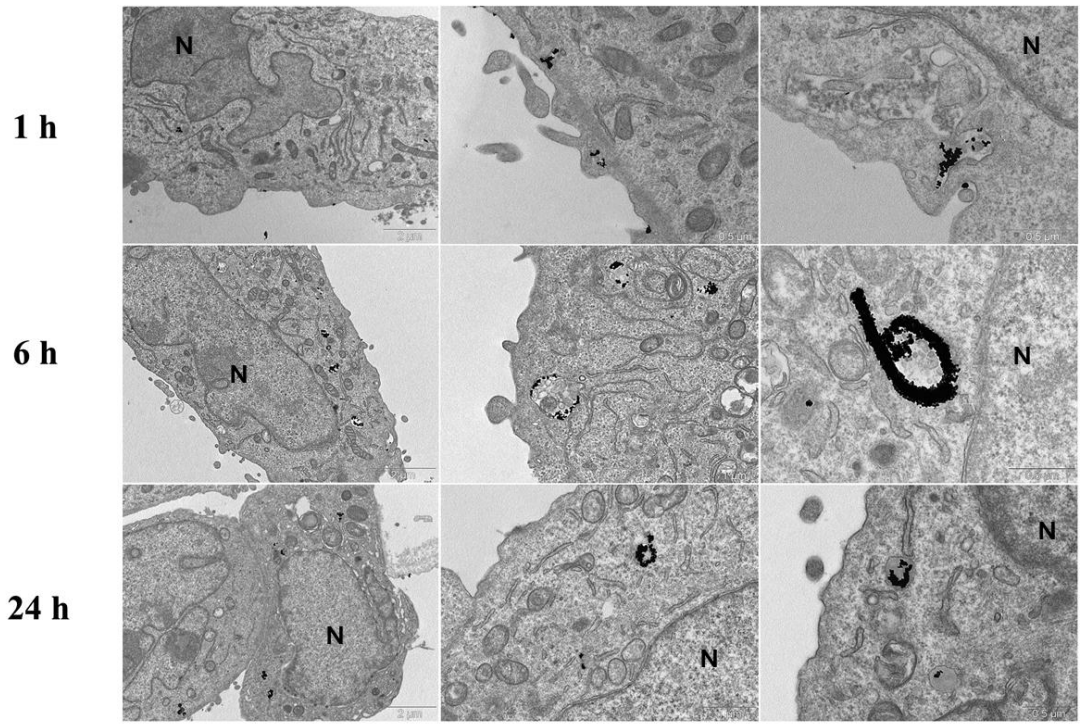

Figure 40. Time-course TEM analysis of AuNR-TAT uptake in T98G cells. Micrographs were captured at 1 h, 6 h, and 24 h post-incubation. The images show a progressive accumulation of gold nanorods within the cytoplasm, predominantly sequestered in vesicular structures. Even at 24 h, the AuNR-TAT clusters remain localized in the perinuclear region without evidence of translocation into the nucleoplasm (N). Scale bars are indicated for each magnification.

Regardless of the experimental conditions used and despite the presence of the TAT peptide—a known nuclear localization signal— no significant differences were observed. Indeed, in both the experimental conditions, the AuNR-TAT remain strictly confined within endo-lysosomal compartments with no evidence of nuclear entry and the number of AuNR-TAT undergoing uptake did not change. Additionally, in the cycling cells, was also studied the time-course of the uptake (i.e. 1, 6, 24h) and, as show in Figure 40, no differences in number of AuNR-TAT's clusters inside cells was observed.

These findings lead to a crucial reinterpretation of the previously observed increase in γ-H2AX foci. Since the TEM analysis confirms that AuNR-TAT do not translocate into the nucleus, the

recorded DNA damage cannot be attributed to the direct action of Auger electrons emitted within the nucleus. The hypothesis is that an indirect mechanism drives the increase in γ-H2AX foci observed (Fig. 37). Since AuNR-TAT have been shown to remain localized within the cytoplasm and considering the extremely short range of Auger electrons, the primary target of irradiation is expected to be the cytoplasm and its organelles. Indeed, numerous studies [114, 115, 116, 117] have demonstrated that selective cytoplasmic irradiation can induce the generation of reactive species, such as ROS and RNS, as well as damage to cytoplasmic organelles. These events can trigger a cascade of secondary cellular responses capable of propagating damage beyond the cytoplasmic compartment and involving the nucleus. In this context, cytoplasmically generated reactive species may diffuse toward the nucleus, promoting a state of oxidative stress and inducing DNA lesions, including DSBs. Therefore, the increase in γ-H2AX foci observed in samples subjected to the combined treatment can be interpreted as the consequence of an indirect mechanism, mediated by cytoplasm-originated oxidative damage rather than by direct nuclear irradiation.

5. CONCLUSION

The present thesis demonstrates a nano-radiosensitization strategy based on gold nanorods functionalized with the TAT peptide (AuNR-TAT), providing a solid proof of concept for future translational development. The TAT functionalization protocol was optimized, achieving colloidal stability for up to four weeks. Moreover, AuNR-TAT ensured efficient cellular internalization, leading to the persistent localization of the nanoconstructs within the cytoplasmic compartment (primarily confined in endo-lysosomal vesicles) as confirmed by TEM, even in proliferating cell populations.

Cytotoxicity and genotoxicity assessments demonstrated that the AuNR-TAT system maintains low intrinsic toxicity at the investigated concentrations, supporting its suitability for combination with radiation-based therapeutic protocols.

The underlying radiosensitization mechanism relies on the physical interaction between ionizing radiation and gold, a high-atomic-number element characterized by an elevated probability of photoelectric absorption. This interaction induces the emission of cascades of secondary and Auger electrons, which exhibit high local LET and extremely short ranges. Although the nanorods did not translocate into the nucleus, γ-H2AX analysis revealed a significant increase in DNA damage following irradiation, indicating a measurable radiobiological enhancement.

These findings support an indirect mechanism of action: Auger electrons emitted in the cytoplasm upon irradiation of AuNR-TAT interact with the surrounding intracellular environment, promoting the generation of reactive species capable of diffusing toward the nucleus and inducing complex DNA lesions. Increasing evidence from the literature suggests that direct energy deposition within nuclear DNA is not strictly required to elicit significant biological effects, as extranuclear irradiation can also trigger comparable damage pathways.

In conclusion, despite the cytoplasmic confinement of Auger electron emission, a clearly detectable increase in DNA damage was observed. This supports the involvement of indirect damage propagation mechanisms from the cytoplasmic compartment to the nucleus. At the same time, the results indicate that further enhancement may be achievable through rational modification of the TAT sequence to promote effective nuclear targeting. Such optimization would enable future studies to systematically compare the radiobiological effects of direct

nuclear Auger emission with those arising from cytoplasmic irradiation, thereby refining the mechanistic understanding of gold-mediated nano-radiosensitization strategies.

6. APPENDIX A:

From March 1st, 2025 to June 30th, 2025, I spent a research period abroad at GSI, in the Biophysics Department directed by Professor Marco Durante. During this time, I worked in the laboratory of the Immune System and Tissue Radiobiology group (group leader: Claudia Fournier) under the supervision of Dr. Alexander Helm.

Throughout this period, I acquired new skills by collaborating closely with the research team. In particular, I improved my expertise in immunofluorescence and flow cytometry. These techniques proved extremely useful once I returned to Italy, as I was able to apply them directly to my research project focused on studying DNA damage through an indirect immunofluorescence assay detecting H2AX histone phosphorylation.

Another important skill I developed was working with mice inoculated with cells grown *in vitro*. This experience allowed me to follow each phase of the experimental workflow step by step: from the *in vitro* stage (cell culture), through the ex vivo phase (using organs or cells derived from mice), and finally to the *in vivo* stage, where I personally collected organs affected by the inoculated tumours and analysed them using the aforementioned techniques.

Closely related to this activity was the opportunity to actively participate in a carbon-ion irradiation session at the high-energy irradiation facility known as CAVE A at GSI.

7. BIBLIOGRAPHY

[1] Santamaria A.; Historical overview of nanotechnology and nanotoxicity; Methods Mol Biol. 2012; 926:1-12. Doi: 10.1007/978-1-62703-002-1_1.

[2] Baig N., Kammakakam I., & Falath W. Nanomaterials: A review of synthesis methods, properties, recent progress, and challenges. Materials advances, 2021, 2(6), 1821-1871. https://doi.org/10.1039/d0ma00807a

[3] Ukueje W.E., Abam F.I., Obi A.; A prospective review on thermal conductivity of hybrid nanofluids and their application in automobile radiator cooling; Journal of Nanotechnology, 2022, 2022,1, 2187932. DOI:10.1155/2022/2187932

[4] Benozir Asha A., Narain R. Polymer science and nanotechnology fundamentals and applications. Elsevier, 2020. Chapter 15, 343-359.

[5] Ghassan, A., Mijan, N., Taufiq-Yap Y.H. Nanomaterials: An Overview of Nanorods Synthesis and Optimization, in Nanorods and Nanocomposites; IntechOpen, 2019, chapter 2, p 11-13.

[6] Frazin L., Sheibani S., Moassesi M.E., Shamsipur M. An overview of nanoscale radionuclides and radiolabeled nanomaterials commonly used for nuclear molecular imaging and therapeutic functions. Wiley Online Library 2018, 107, 251-258 DOI: 10.1002/jbm.a.36550

[7] Freestone I., Meeks N., Sax M., Higgitt C.; The Lycurgus Cup — A Roman nanotechnology. Gold Bull. 2007 ,40, 270–277. https://doi.org/10.1007/BF03215599

[8] Apostolou P., Toloudi M., Chatziioannou M., Ioannou E., Knocke D.R., Nester J., Komiotis D., Papasotiriou I. Anvirzel™ in combination with cisplatin in breast, colon, lung,

prostate, melanoma and pancreatic cancer cell lines. BMC Pharmacol Toxicol. 2013,14,18. DOI: 10.1186/2050-6511-14-18.

[9] Weindling P., Epidemics and genocide in Eastern Europe, 1890-1945. Oxford University Press, USA, 2000.

[10] Huang X., El-Sayed M. A. Gold nanoparticles: Optical properties and implementations in cancer diagnosis and photothermal therapy, Journal of Advanced Research, 2010, 1,1, 13-28. https://doi.org/10.1016/j.jare.2010.02.002

[11] Harish K.K., Nagasamy V., Himangshu B., Anuttam K. Metallic Nanoparticle: A Review. Biomed J Sci &Tech Res 4(2)- 2018, 4,2, 3765-3775. DOI: 10.26717/ BJSTR.2018.04.001011.

[12] Li C., Shuford K.L., Park Q.H., Cai W., Li Y., Lee E.J., Cho S.O. High-yield synthesis of single-crystalline gold nano-octahedra. Angew Chem Int Ed Engl. 2007;46(18):3264-8. DOI: 10.1002/anie.200604167.

[13] Maccora D., Dini V., Battocchio C., Fratoddi I., Cartoni A., Rotili D., Castagnola M., Faccini R., Bruno I., Scotognella T., Giordano A., Venditti I. Gold Nanoparticles and Nanorods in Nuclear Medicine: A Mini Review. Applied sciences 2019; 9 (16): 3232 https://doi.org/10.3390/app9163232

[14] Kamal Eddin F.B., Fen Y.W. The Principle of Nanomaterials Based Surface Plasmon Resonance Biosensors and Its Potential for Dopamine Detection. Molecules 2020, 25, 2769. https://doi.org/10.3390/molecules25122769

[15] Sabban S., Ye H., Helm B. Development of an in vitro model system for studying the interaction of Equus caballus IgE with its high-affinity receptor FcεRI; J Vis Exp; 2014,(93): e52222. DOI: 10.3791/52222.

[16] Nikoobakht B. and El-Sayed M.A. "Surface-enhanced Raman scattering studies on aggregated gold nanorods." The Journal of Physical Chemistry A, 2003,107,18, 3372-3378. DOI:10.1021/jp026770+

[17] Zeng H., Du X., Singh S.C., Kulinich S.A., Yang S., He J., Cai W. Nanomaterials via Laser Ablation/Irradiation in Liquid: A Review. Advanced Functional Materials 2012; 22: 1333-1353 https://doi.org/10.1002/adfm.201102295

[18] Sau T.K., Rogach A.L.,Nonspherical Noble Metal Nanoparticles: Colloid-Chemical Synthesis and Morphology Control. Advanced Materials 2010, 22, 1781-1804 https://doi.org/10.1002/adma.200901271

[19] Zhao P., Na L., Astruc D. State of the art in gold nanoparticle synthesis. Coordination Chemistry Reviews, 2012, 257, 638-665 https://doi.org/10.1016/j.ccr.2012.09.002

[20] Habiba K., Makarov V.I., Weiner B.R., Morell G. Fabrication of Nanomaterials by Pulsed Laser Synthesis. Manufacturing nanostructures, 2014, 10, 263-292. DOI: 10.13140/RG.2.2.16446.28483.

[21] Cai W., Gao T., Hong H., Sun J. Applications of gold nanoparticles in cancer nanotechnology. Nanotechnology, science and applications, 2008, 19.1:17-32. DOI: 10.2147/NSA.S3788

[22] Cai W., Chen X. 2007. Nanoplatforms for targeted molecular imaging in living subjects. Small, 2007, 3,1840–54. DOI: 10.1002/smll.200700351

[23] Kesharwani P., Ma R., Sang L., Fatima M., Sheikh A., Abourehab M.A.S., Gupta N., Chen Z.S., Zhou Y. Gold nanoparticles and gold nanorods in the landscape of cancer therapy. Mol Cancer. 2023,22(1),98. DOI: 10.1186/s12943-023-01798-8.

[24] Devi L., Gupta R., Jain S.K., Singh S., Kesharwani P. Synthesis, characterization and in vitro assessment of colloidal gold nanoparticles of Gemcitabine with natural polysaccharides for treatment of breast cancer. J Drug Deliv Sci Technol. 2020, 56,101565. DOI:10.1016/j.jddst.2020.101565

[25] Kesharwani P., Choudhury H., Meher J.G., Pandey M., Gorain B. Dendrimer entrapped gold nanoparticles as promising nanocarriers for anticancer therapeutics and imaging. Prog Mater Sci. 2019, 103, 484–508. DOI:10.1016/j.pmatsci.2019.03.003

[26] Mahmoudi A., Kesharwani P., Majeed M., Teng Y., Sahebkar A. Recent advances in nanogold as a promising nanocarrier for curcumin delivery. Colloids Surfaces B Biointerfaces. 2022, 215, 112481. DOI: 10.1016/j.colsurfb.2022.112481

[27] Pornnoppadol G., Cho S., Yu J H., Kim S., Nam Y S. Cancer-targeting gold-decorated melanin nanoparticles for in vivo near-infrared photothermal therapy. Mol. Syst. Des. Eng. 2024, 9, 507-517. DOI:10.1039/D3ME00173C

[28] Kumar P.P.P., Lim D.K. Photothermal Effect of Gold Nanoparticles as a Nanomedicine for Diagnosis and Therapeutics. Pharmaceutics. 2023, 15(9),2349. DOI: 10.3390/pharmaceutics15092349.

[29] Choi W.I., Kim J.-Y., Kang C., Byeon C.C., Kim Y.H., Tae G. Tumour regression in vivo by photothermal therapy based on gold-nanorod-loaded, functional nanocarriers. ACS Nano 2011, *5*, 1995–2003. https://doi.org/10.1021/nn103047r

[30] Sriram M., Zong K., Vivekchand S.R., Gooding J.J. Single nanoparticle plasmonic sensors. Sensors 2015, 15, 25774–25792. https://doi.org/10.3390/s151025774

[31] Xie L., Ying X., Li X., Tan X., Zhang T., Zhang X., Chen X., Liu Y., Zhou Y., Zhao J. Engineering of Gold Nanorods as Multifunctional Theranostic Agent for Photothermal-

Enhanced Radiotherapy of Cancer. Materials & Design 2023, 225, 111456. https://doi.org/10.1016/j.matdes.2022.111456

[32] Mabrouk M., Das D.B., Salem Z.A., Beherei H.H. Nanomaterials for Biomedical Applications: Production, Characterisations, Recent Trends and Difficulties. Molecules. 2021, 26(4),1077. https://doi.org/10.3390/molecules26041077

[33] Chen H., Shao L., Li Q., Wang J. Gold nanorods and their plasmonic properties. Chem. Soc. Rev., 2013, 42(7), 2679–2724. https://doi.org/10.1039/C2CS35367A

[34] Feng L., Xuan Z., Ma J., Chen J., Cui D., Su C., Guo J., Zhang Y. Preparation of gold nanorods with different aspect ratio and the optical response to solution refractive index. Journal of Experimental Nanoscience, 2015, 10.4, 258–267. https://doi.org/10.1080/17458080.2013.824619

[35] Pellas V., Hu D., Mazouzi Y., Mimoun Y., Blanchard J., Guibert C., Salmain M., Boujday S. Gold Nanorods for LSPR Biosensing: Synthesis, Coating by Silica, and Bioanalytical Applications. Biosensors 2020, 10, 146. https://doi.org/10.3390/bios10100146

[36] Meng L., Zhang J., Li H., Zhao W., Zhao T. Preparation and Progress in Application of Gold Nanorods; Journal of Nanomaterials, 2019, 2019,1: 4925702. https://doi.org/10.1155/2019/4925702

[37] Jana N.R., Gearheart L., and Murphy C.J. "Wet chemical synthesis of high aspect ratio cylindrical gold nanorods." The Journal of Physical Chemistry B, 2001, 105.19: 4065-4067. https://doi.org/10.1039/B100521I

[38] Nikoobakht B., El-Sayed M.A., Preparation and Growth Mechanism of Gold Nanorods (NRs) Using Seed-Mediated Growth Method; Chem. Mater., 2003, 15,1957-1962. https://doi.org/10.1021/cm0207321

[39] Moreau L., 1, Jones M., Roth E., Wu J., Kewalramani S., O'Brien M., Chen B-R., Mirkin C.A., Bedzyk M. The role of trace Ag in the synthesis of Au nanorods; Nanoscale, 2019, 11, 11744–11754. https://doi.org/10.1039/C9NR03246K

[40] Chankhunthod N., Kidkhunthod P. Synthesis of tunable near infrared absorbance of gold nanorods (AuNRs) and their gold oxidation states during nanorod formation following by synchrotron based X-rays absorption spectroscopy (XANES). Radiation Physics and Chemistry, 2023, 207:110844. DOI: 10.1016/j.radphyschem.2023.110844

[41] Shahi S., Khorvash R., Goli M., Ranjbaran S. M., Najarian A., Mohammadi Nafchi A. Review of proposed different irradiation methods to inactivate food-processing viruses and microorganisms. Food science & nutrition, 2021, 9(10), 5883-5896. https://doi.org/10.1002/fsn3.2539

[42] Grupen C., Shwartz B. Interactions of Particles and Radiation with Matter. In Particle Detectors (pp. 1–55). Cambridge University Press, 2023.

[43] Martin C. J. Interaction of Ionizing Radiations with Matter. In Practical Radiation Protection in Healthcare (2nd ed., pp. 13–35). Oxford University Press, 2019.

[44] Kouchi N., Hatano Y. Interaction of Photons with Molecules: Photoabsorption, Photoionization, and Photodissociation Cross Sections. In A. Mozumder & Y. Hatano (Eds.), Charged Particle and Photon Interactions with Matter: Chemical, Physicochemical, and Biological Consequences with Applications (Chap. 5), 2004. Marcel Dekker. https://doi.org/10.1201/9780203913284

[45] Bichsel H., Schindler H. The Interaction of Radiation with Matter. In C. Grupen & B. Shwartz (Eds.), Particle Physics Reference Library (Vol. 1). Springer, 2020.

[46] International Atomic Energy Agency (IAEA). Radiation Biology: A Handbook for Teachers and Students. Vienna: IAEA, 2018.

[47] Attix F.H. In Introduction to Radiobiological Physics and Radiation Dosimetry; John Wiley & Sons, Inc.: New York, NY, USA, 1986; Chapter 7, pp. 124–159

[48] Amaldi U. In Fisica delle Radiazioni, Ed. Boringhieri, 1984; Chapter 9, pp. 430–448

[49] Faure, G. Principles of Isotope Geology, 2nd ed., John Wiley & Sons, 1986, pp 15-23

[50] Kassis A. I. The Amazing World of Auger Electrons. International Journal of Radiation Biology, 2004, 80(11–12), 789–803. DOI: 10.1080/09553000400017663

[51] Lee B.Q., Kibedi T., Stuchbery A. E., Robertson K. A. Atomic radiations in the decay of medical radioisotopes: a physics perspective. Computational and mathematical methods in medicine,2012,1, 651475. DOI: 10.1155/2012/651475

[52] Hall E.J., Giaccia A. J. Radiobiology for the Radiologist (8th ed.). Wolters Kluwer, 2019 (Chapter 1-6) pp. 1-186.

[53] Turner J.E. Atoms, Radiation and Radiation Protection. Weinheim, Germania: WILEY-VCH Verlag GmbH & Co. KGaA. Terza edizione, 2007 (Chapter 3), pp. 94-104

[54] Guerrini M., Fosbinder R. A., Ciccone M., Kelsey C. A., Beux A. L'immagine radiologica. Tecnologie e tecniche d'acquisizione; McGraw Hill Companies, 2003.

[55] Paganetti H. Relative biological effectiveness (RBE) values for proton beam therapy. Variations as a function of biological endpoint, dose, and linear energy transfer. Phys Med Biol. 2014 Nov 21;59(22):R419-72. DOI: 10.1088/0031-9155/59/22/R419

[56] ICRU (International Commission on Radiation Units and Measurements). Report 85: Fundamental Quantities and Units for Ionizing Radiation. Journal of the ICRU, 2011, 11,1, 1–33.

[57] Pomplun E., Booz J., Charlton D.E. Monte Carlo simulation of Auger cascades. Radiat. Res.; (United States), 1987, 111,3. https://doi.org/10.2307/3576938

[58] Nikjoo H., O'Neill P., Terrissol M., Goodhead D.T. Quantitative modelling of DNA damage using Monte Carlo track structure method. Radiat Environ Biophys. 1999, 38,1,31-8. doi: 10.1007/s004110050135.

[59] Ogawa T., Hirata Y., Matsuya Y., Kai T., Sato T., Iwamoto, Y., Hashimoto S., Furuta T., Abe S., Matsuda N., Sekikawa T., Yao., Tsai P.E., Ratliff H.N., Iwase H., Sakaki Y., Sugihara K., Shigyo N., Sihver L., Niita, K. Overview of PHITS Ver. 3.34 with particular focus on track-structure calculation. EPJ Nuclear Sciences & Technologies, 2024, 10, 13. https://doi.org/10.1051/epjn/2024012

[60] Conte V., Bianchi A., & Selva A. Track structure of light ions: the link to radiobiology. Int. J. Mol. Sci., 2023, 24.6, 5826. https://doi.org/10.3390/ijms24065826

[61] Belli M., Bettega D., Cherubini R., Ianzini F., Kraft G., Simone G., Tabocchini M.A. Phisical and radiobiological properties of hadron beam; The TERA project and the Center of Oncological Handontherapy, 1994, Amaldi U. and Silari, eds.

[62] Douglass M., Bezak E., Penfold S. Monte Carlo investigation of gold nanoparticle radiosensitization using Geant4-DNA. Physics in Medicine & Biology, 2019, 64.12, 125002. https://doi.org/10.1088/1361-6560/ab1e8f

[63] Jeremic B., Aguerri A.R., Filipovic N. Radiosensitization by gold nanoparticles. Clin Transl Oncol. 2013, 15,8,593-601. doi: 10.1007/s12094-013-1003-7.

[64] Brun E., Sanche L., Sicard-Roselli C. Parameters governing gold nanoparticle X-ray radiosensitization of DNA in solution. Colloids Surf B Biointerfaces. 2009, 72,1,128-34. doi: 10.1016/j.colsurfb.2009.03.025.

[65] Boudou C., Politi Y., Fenel D., Sicard-Roselli C. Nanometric dose enhancement around gold nanoparticles under X-ray irradiation: Experimental evidence and Monte Carlo modeling. Radiation Physics and Chemistry, 2021, 188, 109642. https://doi.org/10.1016/j.radphyschem.2021.109642

[66] Llovet X., Powell C.J., Jablonski A., Salvat F. Cross sections for inner-shell ionization and Auger-electron emission. Surface and Interface Analysis, 2014, 46(12–13), 1130–1139. https://doi.org/10.1002/sia.5523

[67] Ridolfi R. Study of the track reconstruction in the FOOT experiment for Hadrontherapy. 2018, https://amslaurea.unibo.it/id/eprint/15786

[68] Nikjoo H., Emfietzoglou D., Liamsuwan T., Taleei R., Liljequist D., Uehara S. Radiation track, DNA damage and response—A review. Reports on Progress in Physics, 2016, 79.11, 116601. DOI: 10.1088/0034-4885/79/11/116601

[69] D-Kondo N., Garcia-Garcia O.R., LaVerne J.A., Faddegon B., Schuemann J., & Ramos-Méndez J. An integrated Monte Carlo track-structure simulation framework for modeling inter and intra-track effects on homogeneous chemistry. Physics in Medicine & Biology, 2023, 68.12, 125008. https://doi.org/10.1088/1361-6560/acd6d0

[70] Pang X.L., He G., Liu Y.B., Wang Y., Zhang B. Endoplasmic reticulum stress sensitizes human esophageal cancer cell to radiation. World J Gastroenterol. 2013, 19(11):1736–48. DOI: 10.3748/wjg.v19.i11.1736

[71] Kam W.W.Y., Banati R.B. Effects of ionizing radiation on mitochondria. Free Radic Biol Med. 2013, 65, 607–19. DOI: 10.1016/j.freeradbiomed.2013.07.024

[72] Wang Js., Wang Hj., Qian Hl. Biological effects of radiation on cancer cells. Military Med Res, 2018, 5, 20. https://doi.org/10.1186/s40779-018-0167-4

[73] Goodhead D.T., Weinfeld M. Clustered DNA Damage and its Complexity: Tracking the History. Radiat Res. 2024 ;202,2,385-407. DOI: 10.1667/RADE-24-00017.1.

[74] Wilkinson B., Hill M.A., Parsons J.L. The Cellular Response to Complex DNA Damage Induced by Ionising Radiation. Int. J. Mol. Sci. 2023, 24, 4920. https://doi.org/10.3390/ijms24054920

[75] Kryston T.B., Georgiev A.B., Pissis P., Georgakilas A.G. Role of oxidative stress and DNA damage in human carcinogenesis, Mutat. Res. Mol. Mech. Mutagen. 2011, 711,193–201. DOI: 10.1016/j.mrfmmm.2010.12.016

[76] Coggle J.E. Effetti biologici delle radiazioni. Torino, Italia: Edizione Minerva Medica, 1985. Seconda edizione.

[77] Rothkamm K., Löbrich M. Evidence for a lack of DNA double-strand break repair in human cells exposed to very low x-ray doses. Proc Natl Acad Sci U S A. 2003, 29,100,9,5057-62 doi: 10.1073/pnas.0830918100.

[78] Mao Z., Bozzella M., Seluanov A., Gorbunova V. DNA repair by nonhomologous end joining and homologous recombination during cell cycle in human cells. Cell Cycle. 2008 15,7,18,2902-6. doi: 10.4161/cc.7.18.6679.

[79] Pardo B., Gómez-González B., Aguilera A. DNA repair in mammalian cells: DNA double-strand break repair: how to fix a broken relationship. Cell Mol Life Sci. 2009, 66,6,1039-56. doi: 10.1007/s00018-009-8740-3.

[80] Mobilio S., Boscherini F., Meneghini C. Synchrotron Radiation: Basics, Methods and Applications. 2015, 1–799 p.

[81] Laajalehto K., Kartio I., Suoninen E. XPS and SR-XPS techniques applied to sulphide mineral surfaces. Int J Miner Process [Internet]. 1997,51,1,163–70. https://doi.org/10.1016/S0301-7516(97)00029-X

[82] Created in https://BioRender.com, 2025

[83] Binelli L., Dini V., Amatori S., Scotognella T., Giordano A., De Berardis B., Bertelà F., Battocchio C., Iucci G., Fratoddi I., Cartoni A., Venditti I. Gold Nanorods as Radiopharmaceutical Carriers: Preparation and Preliminary Radiobiological In Vitro Tests. Nanomaterials 2023, 13, 1898. https://doi.org/10.3390/nano13131898

[84] Frankel A.D., Pabo C.O. Cellular uptake of the tat protein from human immunodeficiency virus. Cell. 1988, 23,55(6),1189-93. doi: 10.1016/0092-8674(88)90263-2.

[85] Ford, K., Souberbielle, B., Darling, D. et al. Protein transduction: an alternative to genetic intervention?. Gene Ther, 2001 8, 1–4. https://doi.org/10.1038/sj.gt.3301383

[86] Sriram M., Zong K., Vivekchand S.R.C., Gooding J.J. Single Nanoparticle Plasmonic Sensors. Sensors 2015, 15, 25774-25792. https://doi.org/10.3390/s151025774;

[87] Santos-Cuevas C.L., Ferro-Flores G., Arteaga de Murphy C., Ramírez F.de M., Luna-Gutiérrez M.A., Pedraza-López M., García-Becerra R., Ordaz-Rosado D. Design, preparation, in vitro and in vivo evaluation of (99m)Tc-N2S2-Tat(49-57)-bombesin: a target-specific hybrid radiopharmaceutical. Int J Pharm. 2009, 22;375(1-2),75-83. doi: 10.1016/j.ijpharm.2009.04.018. Epub 2009 Apr 22. PMID: 19393305.

[88] Puck T.T., Marcus P.I., Action of x-rays on mammalian cells. J Exp Med. 1956 1;103.5:653-66. doi: 10.1084/jem.103.5.653.

[89] Gohy J.F., Zhao Y. Photo-responsive block copolymer micelles: design and behavior. Chemical Society Reviews, 2013, 42,17,7117-7129. https://doi.org/10.1039/C3CS35469E

[90] Duellman S..J, Zhou W., Meisenheimer P., Vidugiris G., Cali J.J., Gautam P., Wennerberg K., Vidugiriene J. Bioluminescent, Nonlytic, Real-Time Cell Viability Assay and Use in Inhibitor Screening. Assay Drug Dev Technol. 2015 ,13,8,456-65. doi: 10.1089/adt.2015.669.

[91] RealTime-Glo™ MT Cell Viability Assay Technical Manual https://ita.promega.com/-/media/files/resources/protocols/technical-manuals/101/realtimeglo-mt-cell-viability-assay-protocol.pdf?rev=63ece8344f0647d1a028b59c1952dfe4&sc_lang=en

[92] Venditti I., Iucci G., Fratoddi I., Cipolletti M., Montalesi E., Marino M., Secchi V., Battocchio C. Directly Resveratrol immobilization on hydophilic charged gold nanoparticles: Structural investigation and cytoxic studies. Nanomaterials, 2020, 10, 1898. https://doi.org/10.3390/nano10101898

[93] Fratoddi I., Venditti I., Battocchio C., Carlini L., Amatori S., Porchia M., Tisato F., Bondino F., Magnano E., Pellei M., Santini C. Highly Hydrophilic Gold Nanoparticles as Carrier for Anticancer Copper(I) Complexes: Loading and Release Studies for Biomedical Applications. Nanomaterials (Basel). 2019 20,9.5,772. https://doi.org/10.3390/nano9050772

[94] Hackley V.A., Clogston J.D. Measuring the Hydrodynamic Size of Nanoparticles in Aqueous Media Using Batch-Mode Dynamic Light Scattering, in Characterization of Nanoparticles Intended for Drug Delivery, Scott E. McNeil Editor, Springer pp. 35-52, 2011.

[95] Amatori S., Lopez A., Meneghini C., Calcabrini A., Colone M., Stringaro A., Migani S., Khalakhan I., Iucci G., Venditti I., Battocchio C. Gold nanorods derivatized with CTAB and hydroquinone or ascorbic acid: spectroscopic investigation of anisotropic

nanoparticles of different shapes and sizes. Nanoscale Adv. 2023, 5,15, 3924– 3933, DOI: 10.1039/d3na00356f

[96] Venditti I., Cartoni A., Fontana L., Testa G., Scaramuzzo F.A., Faccini R., Mancini Terracciano C., Solfaroli Camillocci E., Morganti S., Giordano A., Scotognella T., Rotili D., Dini V., Marini F., Fratoddi I. Y3+ embedded in polymeric nanoparticles: Morphology, dimension and stability of composite colloidal system. Colloids and Surfaces A: Physicochemical and Engineering Aspects 2017, 532, 125-131. https://doi.org/10.1016/j.colsurfa.2017.05.082

[97] NIST X-ray Photoelectron Spectroscopy Database, Version 4.1 (National Institute of Standards and Technology, Gaithersburg) 2012 http://srdata.nist.gov/xps/

[98] Venditti I., Cartoni A., Cerra S., Fioravanti R., Salamone T. A., Sciubba F., Tabocchini M.A., Dini V., Battocchio C., Iucci G., Carlini L., Faccini R., Collamati F., Mancini Terracciano C., Solfaroli Camillocci E., Morganti S., Giordano A., Scotognella T., Maccora D., Rotili D., Marchese C., Anastasiadou E.,Trivedi P., Fratoddi I. Hydrophilic Gold Nanoparticles as anti-PD-L1 Antibody carriers: Synthesis and Interface Properties. Particle and Particle Systems Characterization 2022, 39,4, 2100282. DOI: 10.1002/ppsc.202100282

[99] Stumpf T., Foerstendorf H., Bok F., Richter, A. Annual Report 2018 - Institute of Resource Ecology 2019

[100] Gao M., Zhao H., Wang Z., Zhao Y., Zou X., Sun L. Controllable preparation of Ag2S quantum dots with size-dependent fluorescence and cancer photothermal therapy, Advanced Powder Technology, 2021, 32, 6, 1972-1982, ISSN 0921-8831, https://doi.org/10.1016/j.apt.2021.04.011.

[101] Sriram M., Zong K., Vivekchand S.R.C., Gooding, J.J. Single Nanoparticle Plasmonic Sensors. Sensors 2015, 15, 25774-25792. https://doi.org/10.3390/s151025774

[102] N1) Stöhr J. NEXAFS Spectroscopy; Springer Series in Surface Sciences; Springer: Berlin/Heidelberg, Germany, 1992; doi:10.1007/978-3-662-02853-7

[103] Brun P., Zamuner A., Battocchio C., Cassari L., Todesco M., Graziani V., Iucci G., Marsotto M., Tortora L., Secchi V., Dettin M. Bio-Functionalized Chitosan for Bone Tissue Engineering, International Journal of Molecular Sciences 2021, 225916 DOI: 10.3390/ijms22115916

[104] Ref N1, N2, Santos-Cuevas C.L., Ferro-Flores G., Arteaga de Murphy C., Ramírez Fde M., Luna-Gutiérrez M.A., Pedraza-López M., García-Becerra R., Ordaz-Rosado D. Design, preparation, in vitro and in vivo evaluation of (99m)Tc-N2S2-Tat(49-57)-bombesin: a target-specific hybrid radiopharmaceutical. Int J Pharm. 2009 ,375(1-2):75-83. DOI: 10.1016/j.ijpharm.2009.04.018.

[105] Silverstein R.M. and Webster F.X. Spectrometric Identification of Organic Compounds. 6th Edition, Wiley, 2003, New York.

[106] Battocchio C., Iucci G., Dettin M., Carravetta V., Monti S., Polzonetti G. Self-assembling behaviour of self-complementary oligopeptides on biocompatible substrates; Materials Science and Engineering B, 2010, 169:36-42 doi:10.1016/j.mseb.2009.12.051

[107] AIST spectral database for organic compounds; https://sdbs.db.aist.go.jp/

[108] Galezowski W., Jarczewski A., Stanczyk M., Brzezinski B., Bartl F., Zundelc G. Homoconjugated hydrogen bonds with amidine and guanidine bases. Osmometric, potentiometric and FTIR studies, J. Chem. Soc., Faraday Trans., 1997, 93,15, 2515-2518. https://doi.org/10.1039/A700668C

[109] Freudenberg R., Runge R., Maucksch U., Berger V., Kotzerke J. On the dose calculation at the cellular level and its implications for the RBE of 99mTc and 123I. Med. Phys., 2014, 41: 062503. DOI: 10.1118/1.4876296

[110] Boglaienko D., Soltis J., Kukkadapu R., Du Y., Sweet L., Holfeltz V., Hall G., Buck E., Segre C., Emerson H., Katsenovich Y., Levitskaia T. Spontaneous redox continuum reveals sequestered technetium clusters and retarded mineral transformation of iron. Communications Chemistry 2020, 3, 87. DOI: 10.1038/s42004-020-0334-x

[111] Chew M.T., Bradley D.A., Suzuki M., Matsufuji N., Murakami T., Jones B., Nisbet A. The radiobiological effects of He, C and Ne ions as a function of LET on various glioblastoma cell lines. Journal of Radiation Research 2019, 60, 178–188. DOI: 10.1093/jrr/rry099

[112] Burdak-Rothkamm S., Smith A., Lobachevsky P., Martin R., Prise K.M. Radioprotection of targeted and bystander cells by methylproamine. Strahlenther Onkol 2015, 191, 248–255. DOI: 10.1007/s00066-014-0751-9

[113] Short S., Mayes C., Woodcock M., Johns H., Joiner M.C. Low dose hypersensitivity in the T98G human glioblastoma cell line. International Journal of Radiation Biology 1999, 75, 847-855. DOI: 10.1080/095530099139908

[114] Kobayashi A., Tengku Ahmad T.A.F., Autsavapromporn N., Oikawa M., Homma-Takeda S., Furusawa Y., Wang J., Konishi T. Enhanced DNA double-strand break repair of microbeam targeted A549 lung carcinoma cells by adjacent WI38 normal lung fibroblast cells via bi-directional signaling. Mutat Res. 2017 803-805:1-8. DOI: 10.1016/j.mrfmmm.2017.06.006.

[115] Konishi T., Kobayashi A., Tengku Ahmad T.A., Wang J. Enhanced DNA double strand break repair triggered by microbeam irradiation induced cytoplasmic damage. J Radiat Cancer Res 2018, 9:183-9. DOI: 10.4103/jrcr.jrcr_21_18

[116] Zhang Z., Li K., Hong M. Radiation-Induced Bystander Effect and Cytoplasmic Irradiation Studies with Microbeams. Biology 2022, 11, 945. https://doi.org/10.3390/biology11070945

[117] Tomita M., Torigata M., Ohchi T., Ito A. Observation of Histone H2AX Phosphorylation by Radiation-Induced Bystander Response Using Titanium Characteristic X-ray Microbeam. Biology (Basel). 2023, 12,5:734. doi: 10.3390/biology12050734.

LIST OF PEER-REVIEW PUBLICATIONS

1) **Binelli, L**., Dini, V., Amatori, S., Scotognella, T., Giordano, A., De Berardis, B., Bertelà, F., Battocchio, C., Iucci, G., Fratoddi, I., Cartoni, A., & Venditti, I. *Gold Nanorods as Radiopharmaceutical Carriers: Preparation and Preliminary Radiobiological In Vitro Tests.* Nanomaterials 2023, 13, 1898. https://doi.org/10.3390/nano13131898

2) Ranaldi M., Ferrarini A., Palma A., **Binelli L**., Dini V., Rosi A., Ammendolia M.G., De Berardis B., Battocchio C., Iucci G., Attili A., Bianchi L., Calcagni M.L., Fabbri A., Scotognella T., Venditti I., Grande S. *MRS Studies of the Effects Induced by Gold Nanorods and Ionizing Radiation Treatments in Glioblastoma Cultured Cells;* Eur. Phys. J. Plus. Under rev.

3) **Binelli L.,** Bertelà F., Amatori S., Lipani D., Battocchio C., Iucci G., Tortorà L., Dini V., Grande S., Palma., Ranaldi M., De Berardis B., Ammendolia M.G., Mancini Terraciano C., Fabbri A., Attili A., Scotognella T., Giordano A., Calcagni M.L., Dettin M., Zamuner A., Maraloiu V.A., Venditti I. *Peptide-functionalized gold nanorods as model to reach cell nucleus: synthesis and structural characterizations in view of theragnostic applications*; Journal of Physical Chemestry B, in press april 2026.

4) Ferrarini A., Ranaldi M., Grande S., Ammendolia M.G, Dini V., **Binelli L.**, Battocchio C., Dettin M., Zamuner A., Bianchi L., Attili A., Fabbri A., Scotognella T., Calcagni M.L., Venditti I., Palma A.; *Study of the combined effect of CTAB functionalized gold nanorods and radiation on tumor cell metabolism via MRS technique*; JAPL Conferences Series NanoInnovation 2025 submitted 2026

5) **Binelli L.,** Attili A., Venditti I., Battocchio C., Dini V., Calcagni M.L., Ranaldi M., Iucci G., Trortora L., Grande S., Palma A., Rosi A., De Berardi B., Ammendolia M.G., Scotognella T., Campanaro F., Dettini M., Bianchi L., Fabbri A.; *Gold nanorods–*

radiopharmaceutical conjugates for nuclear medicine theranostics: a methodological and multiscale perspective, Theranostic, In preparation

6) Scotognella T., **Binelli L.,** Attili A., Battocchio C., Dini V., Calcagni M.L., Ranaldi M., Iucci G., Trortora L., Grande S., Palma A., Rosi A., De Berardi B., Ammendolia M.G., Campanaro F., Zamuner A., Dettin M., Bianchi L., Fabbri A., Calcagni M.L., Venditti I. *The ^{99}Tc functionalized gold nanorods as new teranotstic tool*, International Journal of Molecula Science, in preparation

Conference Proceedings

1) M. Ranaldi, **L. Binelli**, A. Palma, V. Dini, B. De Berardis, M. Ammendolia, C. Battocchio, G. Iucci, A. Ruocco, A. Attili, A. Fabbri, L. Tortora, T. Scotognella, A. Giordano, I. Venditti, S. Grande. Effects of ionizing radiation treatment and gold nanorods on glioblastoma cells: a Magnetic Resonance Spectroscopy study for optimization in Nuclear Medicine. Atti del Convegno Nazionale AIRP di Radioprotezione "*La radioprotezione della popolazione: esposizioni pianificate ed esistenti in un'ottica di sostenibilità*": ISBN 9788888648545

2) **L. Binelli**, I. Venditti, M. Ranaldi, S. Grande, A. Palma, A. Rosi, B. De Berardis, M.G. Ammendolia, L. Tortora, S. Amatori, G. Iucci, C. Battocchio, C. Mancini Terraciano, A. Fabbri, A. Attili, T. Scotognella, A. Giordano, M. Dettin and V. Dini. *Implementation theranositc for nuclear medicine application: preliminary biological data*; European Radiation Protection Week (ERPW), 11-15 November 2024, Rome, Italy; Istituto Superiore di Sanità ISSN 0393-5620 ISTISAN, Congressi 24/C4.

3) M. Ranaldi, **L. Binelli**, C. Battocchio, G. Iucci, A. Palma, A. Rosi, B. De Berardis, M.G. Ammendolia, V. Dini, A. Ruocco, A. Fabbri, A. Attili, L. Tortora, L. Scotognella, A. Giordano, I. Venditti, S. Grande. *Effects of ionizing radiation and gold nanorods combined treatrment on glioblastoma cells studied by magnetic resonance*

spectroscopy: a possible nuclear medicine theragnorstic tool. European Radiation Protection Week (ERPW), 11-15 November 2024, Rome, Italy; Istituto Superiore di Sanità ISSN 0393-5620 ISTISAN, Congressi 24/C4.

4)

Oral at Congress

1) **L. Binelli**, I. Venditti, M. Ranaldi, S. Grande, A. Palma, A. Rosi, B. De Berardis, M. G. Ammendolia, L. Tortora, S. Amatori, G. Iucci, C. Battocchio, C. Mancini Terraciano, A. Fabbri, A. Attili, T. Scotognella, A. Giordano, V. Dini. *Implementation of a theragnostic system for applications in nuclear medicine: preliminary biological data*; XXI NATIONAL CONFERENCE of the Italian Society for Radiation Research (SIRR); October 14-16, 2024, Pavia, Italy

2) **L. Binelli**, I. Venditti, M. Ranaldi, S. Grande, A. Palma, A. Rosi, B. De Berardis, M.G. Ammendolia, L. Tortora, S. Amatori, G. Iucci, C. Battocchio, C. Mancini Terraciano, A. Fabbri, A. Attili, T. Scotognella, A. Giordano, M. Dettin and V. Dini. *Implementation theranositc for nuclear medicine application: preliminary biological data; European Radiation Protection Week* (ERPW), 11-15 November 2024, Rome, Italy.

3) **L. Binelli**, V. Dini, M. Ranaldi, S. Grande, A. Palma, A. Rosi, B. De Berardis, M.G. Ammendolia, L. Tortora, G. Iucci, C. Battocchio, D. Lipani, C. Mancini Terracciano, A. Fabbri, A. Attili, T. Scotognella, M.L. Calcagni, M. Dettin, I. Venditti; *Development of AuNR-Based Theranostic Systems for Targeted Nuclear Medicine*; European Radiation Research Society (ERRS) Meeting 2025, 2-4 September 2025, Brussels, Belgium.

4) **L. Binelli**, V. Dini, M. Ranaldi, S. Grande, A. Palma, A. Rosi, B. De Berardis, M.G. Ammendolia, L. Tortora, G. Iucci, C. Battocchio, D. Lipani, C. Mancini Terraciano, A. Fabbri, A. Attili, T. Scotognella, M.L. Calcagni, M. Dettin, I. Venditti. Surface

Functionalization of Gold Nanorods with Peptides for Targeted Nuclear Delivery in Glioblastoma; Nanoinnovation. 15-19 September 2025, Rome, Italy.

5) M. Ranaldi, **L. Binelli**, I. Venditti, C. Battocchio, G. Iucci, A. Attili, V. Dini, A. Rosi, A. Palma, S. Grande. *Preliminary NMR characterization of gold nanorods developed for drug delivery systems in Glioblastoma cells;* NanoInnovation 2024, 9-13 Settembre, 2024, Rome, Italy

6) M. Ranaldi, **L. Binelli**, A. Palma, V. Dini, B. De Berardis, M. Ammendolia, C. Battocchio, G. Iucci, A. Ruocco, A. Attili, A. Fabbri, L. Tortora, T. Scotognella, A. Giordano, I. Venditti, S. Grande. *Effects of ionizing radiation treatment and gold nanorods on glioblastoma cells: a Magnetic Resonance Spectroscopy study for optimization in Nuclear Medicine*; AIRP National Conference on Radioprotection, September 25-27, 2024, Lucca, Italy

7) M. Ranaldi, **L. Binelli**, A. Palma, V. Dini, B. De Berardis, M.G. Ammendolia, A. Rosi, C. Battocchio, G. Iucci, A. Attili, A. Fabbri, L. Tortora, T. Scotognella, A. Giordano, I. Venditti, S. Grande. *Possible synergistic effects of ionizing radiation treatment and gold nanorods on human glioblastoma cells: a magnetic resonance spectroscopy study*; XXI National Conference SIRR, 14-16 October 2024, Pavia, Italy

8) M. Ranaldi, L. Torrieri Di Tullio, **L. Binelli**, A. Palma, V. Dini, B. De Berardis, M.G. Ammendolia, A. Rosi, C. Battocchio, G. Iucci, A. Attili, A. Fabbri, L. Tortora, T. Scotognella, A. Giordano, P. Fattibene, I. Venditti, S. Grande. *Effects of ionizing radiation and gold nanorods treatment on human glioblastoma cells: a combined MR and EPR spectroscopy study*. 1st GIDRM-GIRSE joint day, 6 Dicember 2024, Roma.

9) S. Grande, M. Ranaldi, A. Ferrarini, **L. Binelli**, D. Lipani, A. Palma, A. Rosi, V. Dini, B. De Berardis, M.G. Ammendolia, T. Scotognella, L. Bianchi, C. Battocchio, A. Attili, M.L. Calcagni, I. Venditti, A. Fabbri. *Sistemi teragnostici innovativi basati su*

nanobacchette d'oro ai fini dell'ottimizzazione in Medicina Nucleare: il progetto INFN "SEGNAR"; XXXIX Congresso Nazionale Airp. 29-31 October 2025, Padova, Italy

Poster at Congress

1) **L. Binelli**, T. Scotognella, A. Giordano, F. Bertelà, C. Battocchio, G. Iucci, A Fabbri, V. Dini and I. Venditti. *Conjugation of gold nanorods and 99Tc based radiopharmaceutical to create a theragnostic system*.; 12th International Colloids Conference; 11-14 June 2023, Palma de Mallorca, Spain.

2) **L. Binelli**, V. Dini, S. Grande, A. Palma, B. De Berardis, M.G. Ammendolia, F. Bertelà, L. Tortora, G. Iucci, C. Battocchio, C. Mancini Terraciano, A. Fabbri, A. Attili, T. Scotognella, A. Giordano, M. Dettin and I. Venditti. *Gold nanorods -functionalized to reach cell nucleus: new tools for theranostic applications*; Nanoinnovation; 18-22 September 2023, Rome, Italy.

3) **L. Binelli**, V. Dini, M. Ranaldi, S. Grande, A. Palma, B. De Berardis, M. G. Ammendolia, L. Tortora, S. Amatori, G. Iucci, C. Battocchio, C. Mancini Terraciano, A. Fabbri, A. Attili, T. Scotognella, A. Giordano , M. Dettin, I. Venditti. *Preliminary studies of gold nanorods for the development of theranostic systems and their applications in Nuclear Medicine*; European Radiation Research Society Meeting (ERRS), 10-13 September 2024, Aveiro, Portugal.

4) **L. Binelli**, V. Dini, M. Ranaldi, S. Grande, A. Palma, A. Rosi, B. De Berardis, M. G. Ammendolia, L. Tortora, G. Iucci, C. Battocchio, D. Lipani, C. Mancini Terraciano, A. Fabbri, A. Attili, T. Scotognella, M. L. Calcagni, M. Dettin, I. Venditti; *Peptide-Mediated Surface Functionalization of Gold Nanorods for Nuclear Targeting in Glioblastoma Cells*; 50th Conference of the Divisione di Chimica Inorganica, 9-12 September 2025, Naples, Italy.

5) S. Amatori, **L. Binelli**, V. Dini, G. Esposito, C. Battocchio, G. Iucci, L. Tortora, E. Marconi, C. Meneghini, I. Fratoddi, A. Cartoni, D. Rotili, F. Collamati, R. Faccini, A. Giordano, T. Scotognella and I. Venditti. *Gold nanorods: synthesis, structural characterizations and in vitro biological tests for future applications in nuclear medicine*; First Symposium for YouNg Chemists: Innovation and Sustainability (SYNC2022), June, 20 – 22 Rome 2022

6) V. Dini, A. Giordano, G. Esposito, **L. Binelli**, C. Battocchio, T. Scotognella, I. Venditti. Gold nanorods and radioisotopes: future diagnostic and therapeutic applications in nuclear medicine. *Preliminary in vitro radiobiological tests*; 47th Annual Meeting of the European Radiation Research Society (ERRS 2022), 21-24 september 2022, Catania, Italy

7) I. Venditti, **L. Binelli**, F. Bertelà, S. Amatori, I. Fratoddi, M. Ranaldi, G. Iucci, V. Dini, B. De Berardis, S. Grande, A. Palma, T. Scotognella, A. Giordano, C. Battocchio. *Fluorescent gold nanoparticles as carrier for radiopharmaceuticals*; 49° Congresso Nazionale di Chimica Inorganica – 12-15 settembre 2023 – Perugia, Italy.

8) S. Amatori, **L. Binelli**, A. Lopez, F. Bertelà ,I. Venditti, G. Iucci, C. Meneghini, V. Dini, C. Santini, M. Pellei and C. Battocchio. *Gold Nanorods: Synthesis, Functionalization and Characterization for Drug Delivery Applications*; The first Joint European MRS Chapter Workshop; 19-22 March 2024, Paris, France.

9) M. Ranaldi, **L. Binelli**, D. Lipani, V.Dini, C. Battocchio, G. Iucci, A. Ruocco, B. De Berardis, M. Ammendolia, A. Attili, A. Fabbri, L. Tortora, T. Scotognella, A. Giordano, A. Palma, S. Grande, I. Venditti. *NMR Characterization of metabolic response in glioblastoma cells interacting with gold nanorods*; XXVIII National Congress of Società Chimica Italiana. SCI 2024, 26-30 August 2024, Milano, Italy.

10) M. Ranaldi, **L. Binelli**, C. Battocchio, G. Iucci, A. Palma, A. Rosi, B. De Berardis, M.G. Ammendolia, V. Dini, A. Ruocco, A. Fabbri, A. Attili, L. Tortora, L. Scotognella, A. Giordano, I. Venditti, S. Grande. *Effects of ionizing radiation and gold nanorods combined treatrment on glioblastoma cells studied by magnetic resonance spectroscopy: a possible nuclear medicine theragnorstic tool*. European Radiation Protection Week (ERPW), 11-15 November 2024, Rome, Italy.

11) M. Ranaldi, D. Lipani, G. Iucci, C. Battocchio, A. Palma, A. Rosi, B. De Berardis, M.G. Ammendolia, **L. Binelli**, V. Dini, A. Fabbri, L. Bianchi, A. Attili, T. Scotognella, M.L. Calcagni, I. Venditti, S. Grande. *Optimization of Gold Nanorods for theragnostic application: a possible nuclear medicine tool for cancer treatment*; 13°Congresso Nazionale AIFM 2025, 16-19 October 2025, Verona, Italy.